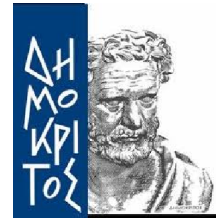




ΕΘΝΙΚΟ ΜΕΤΣΟΒΙΟ
ΠΟΛΥΤΕΧΝΕΙΟ
ΣΧΟΛΗ ΕΦΑΡΜΟΣΜΕΝΩΝ
ΜΑΘΗΜΑΤΙΚΩΝ &
ΦΥΣΙΚΩΝ ΕΠΙΣΤΗΜΩΝ

ΕΚΕΦΕ ΔΗΜΟΚΡΙΤΟΣ
ΙΝΣΤΙΤΟΥΤΟ
ΠΥΡΗΝΙΚΗΣ
ΦΥΣΙΚΗΣ &
ΣΤΟΙΧΕΙΩΔΩΝ
ΣΩΜΑΤΙΔΙΩΝ



Μέθοδος Υπολογισμού της Ενέργειας Μιονίων και Νετρίνων στο Τηλεσκόπιο KM3NeT

ΔΙΔΑΚΤΟΡΙΚΗ ΔΙΑΤΡΙΒΗ

της

Ευαγγελίας Κ. Δρακοπούλου

Επιβλέπων: Τσιπολίτης Γιώργος
Καθηγητής στο Εθνικό Μετσόβιο Πολυτεχνείο



ΕΘΝΙΚΟ ΜΕΤΣΟΒΙΟ ΠΟΛΥΤΕΧΝΕΙΟ

ΣΧΟΛΗ ΕΦΑΡΜΟΣΜΕΝΩΝ ΜΑΘΗΜΑΤΙΚΩΝ & ΦΥΣΙΚΩΝ ΕΠΙΣΤΗΜΩΝ

ΤΟΜΕΑΣ ΦΥΣΙΚΗΣ

ΕΡΓΑΣΤΗΡΙΟ ΠΕΙΡΑΜΑΤΙΚΗΣ ΦΥΣΙΚΗΣ ΥΨΗΛΩΝ ΕΝΕΡΓΕΙΩΝ

Μέθοδος Υπολογισμού της Ενέργειας Μιονίων και Νετρίνων στο Τηλεσκόπιο KM3NeT

ΔΙΔΑΚΤΟΡΙΚΗ ΔΙΑΤΡΙΒΗ

της

Ευαγγελίας Κ. Δρακοπούλου

ΤΡΙΜΕΛΗΣ ΣΥΜΒΟΥΛΕΥΤΙΚΗ
ΕΠΙΤΡΟΠΗ:

1. Γ. Τσιπολίτης, Καθ. ΕΜΠ
2. Χ. Μάρκου, Διευθ. Ερευν.
ΕΚΕΦΕ Δημόκριτος
3. Α. Τζαμαριουδάκη Κύρ.Ερευν.
ΕΚΕΦΕ Δημόκριτος

ΕΠΤΑΜΕΛΗΣ ΕΞΕΤΑΣΤΙΚΗ
ΕΠΙΤΡΟΠΗ:

1. Γ. Τσιπολίτης, Καθ. ΕΜΠ
2. Χ. Μάρκου, Διευθ. Ερευν.
ΕΚΕΦΕ Δημόκριτος
3. Α. Τζαμαριουδάκη, Κύρ. Ερευν.
ΕΚΕΦΕ Δημόκριτος
4. Θ. Αλεξόπουλος, Καθ. ΕΜΠ
5. Ε. Γαζής, Καθ. ΕΜΠ
6. Γ. Φανουράκης, Διευθ. Ερευν.
ΕΚΕΦΕ Δημόκριτος
7. Κ. Κουσουρή, Επ. Καθ. ΕΜΠ



NATIONAL TECHNICAL
UNIVERSITY OF ATHENS
SCHOOL OF APPLIED
MATHEMATICAL &
PHYSICAL SCIENCES

NCSR DEMOKRITOS
INSTITUTE OF
NUCLEAR &
PARTICLE
PHYSICS



Muon and Neutrino Energy Reconstruction for KM3NeT

DOCTORAL OF PHILOSOPHY
PHYSICS

by

Evangelia K. Drakopoulou

SUPERVISOR: Tsipolitis Yorgos
Professor at National Technical University of Athens

©NATIONAL TECHNICAL UNIVERSITY OF ATHENS
ALL RIGHTS RESERVED

Athens, March 2016

Acknowledgements

Writing a PhD thesis is the end of many years of exciting research and hard work. During these years lots of people encouraged and supported me in different ways. Here, I would like to thank all these people for their help.

First, I would like to express my gratefulness and deepest gratitude to the supervisors of this thesis. I would not have gone all this way without their guidance and generous support during these years. In particular, I would like to thank Katerina Tzamariudaki, Senior Researcher at N.C.S.R. Demokritos, for her continuous guidance and her constant encouragement which were sometimes vital in making this dissertation a reality. I owe her many thanks for her patience to answer my questions, her sincere willingness to help when needed and her invaluable assistance to all the code-compatibility problems. I also owe many thanks to Christos Markou, Director of Research at N.C.S.R. Demokritos, for the trust he has shown to my person, his academic guidance during my PhD studentship and for his efforts to supply me with the best conditions to work including funds that gave me the opportunity to successfully complete my thesis and attend schools and conferences. I am indeed indebted to my supervisors for their assistance in reading and correcting all the papers, all the presentations and of course this thesis. I would also like to acknowledge Yorgos Tsipolitis, Professor at National Technical University of Athens, for being an excellent academic teacher who first inspired me to get involved with the field of particle physics and introduced me to this research group of highly-experienced scientists at N.C.S.R. Demokritos. He and Professor Theodore Alexopoulos gave me the chance to be a summer student at DESY Research Centre where I first decided to draw my path in astroparticle physics and I owe them many thanks.

Many thanks also belong to people in N.C.S.R. Demokritos who were always there for me. Thanks to Georgia Karellh for her warm smile, her endless kindness and her willingness to provide her assistance to overcome any kind of problem. I would also like to thank Christos Filippidis for solving several problems with PC and computer cluster and to the Director of Research Petros Rapidis for motivating me (with his unique way) to improve my skills and enrich my knowledge.

My officemates were always supporting and encouraging me all these years. Many thanks to Dr. Eleni Ntomari for her invaluable advice and all the nice chats at the office. Thanks to Iasonas Topsis-Giotis and Dr. Ariadni Antonaki for the fascinating breaks and the fruitful discussions. I also owe many thanks to Konstantinos Pikounis for providing his help when needed, for sharing all the problems with software and for being a very good fellow and friend in all the meetings and conferences. I should also say thank you to all my colleagues for the memorable lunch breaks and the great memories; thanks to George Androulakis for his great sense of humor, to Konstantia Balasi for her unique comments, to Panagiotis Damianos for sharing his experiences with us and to Anna, Lisa, Fanis and Giannis for transferring their enthusiasm to our team. Last but not least, I would like to thank my friends from school and university for being in my life, for their support and the nice memories we shared all these years.

My utmost respect, love and gratitude belongs to my parents, Kostas and Olympia, who taught me to set goals and work hard to fulfill them. They encouraged me to dream and never give up upon difficulties. I owe them who I am. I would also like to thank my husband, George, for standing by me all these years, for his support and his endless patience when hearing "unknown words"; such as neutrinos. Many thanks to my brother, George, for his advice and for his different way of thinking that usually helped me think out of the box. Many thanks to my sisters, Katerina and Sofia, who were

always there for me and helped me to overcome all the difficulties.

Thank you.

To my family who encouraged me all these
years

Περίληψη

Οι άνθρωποι πάντα ήθελαν να εξερευνήσουν τα μυστήρια του σύμπαντος. Άρχισαν λοιπόν να παρατηρούν τον ουρανό με τηλεσκόπια ανιχνεύοντας φωτόνια σε διαφορετικά μήκη κύματος του ηλεκτρομαγνητικού φάσματος. Τα φωτόνια χρησιμοποιούνται ευρέως στην αστρονομία καθώς κινούνται σε ευθείες γραμμές και έρχονται στη Γη απευθείας από το σημείο του ουρανού από όπου ξεκινούν. Εντούτοις, τα φωτόνια μπορούν να απορροφηθούν από τη διαγαλαξιακή ύλη κι έτσι δε φτάνουν στη Γη όταν ταξιδεύουν διαγαλαξιακές αποστάσεις. Επιπλέον, τα φορτισμένα σωματίδια που μπορούν κι αυτά να αποτελέσουν "κοσμικούς αγγελιοφόρους", εκτρέπονται από μαγνητικά πεδία και φτάνουν στη Γη με διαφορετικές κατευθύνσεις από τις αρχικές τους. Με αυτό τον τρόπο, τα φορτισμένα σωματίδια δεν μπορούν να παρέχουν πληροφορίες για το σημείο παραγωγής τους στον ουρανό.

Αντίθετα με τα φωτόνια και τα φορτισμένα σωματίδια, τα νεutrίνο μπορούν να αναδύονται μέσα από τις πηγές παραγωγής τους και να ταξιδεύουν ανεπηρέαστα στο Σύμπαν. Τα ουδέτερα νεutrίνο δεν αντιδρούν με τα μαγνητικά πεδία και δεν απορροφώνται από τη διαγαλαξιακή ύλη δείχνοντας έτσι την κατεύθυνση των πηγών παραγωγής τους. Αυτές οι ιδιότητες καθιστούν τα νεutrίνο ιδανικούς κοσμικούς αγγελιοφόρους. Εντούτοις, τα νεutrίνο αντιδρούν ασθενώς με την ύλη και απαιτούνται μεγάλοι ανιχνευτικοί όγκοι για την ανίχνευσή τους σε ικανή στατιστική ώστε να εντοπισθούν οι πηγές τους. Τα τηλεσκόπια νεutrίνων τοποθετούνται στη θάλασσα, σε λίμνες ή στον πάγο και προσπαθούν να ανιχνεύσουν νεutrίνο τα οποία έχουν διασχίσει τη Γη και αντιδρούν κοντά στον ανιχνευτή. Τα νεutrίνο ανιχνεύονται έμμεσα, από το φως που συγκεντώνεται από τους φωτοπολλαπλασιαστές κατά τις αντιδράσεις των σωματιδίων που προέρχονται από τα νεutrίνο με το ανιχνευτικό μέσο (το θαλασσινό νερό, το νερό των λιμνών ή τον πάγο). Το φως στους φωτοπολλαπλασιαστές χρησιμοποιείται για την ανακατασκευή της κατεύθυνσης του νεutrίνο και την εκτίμηση της ενέργειάς του.

Το τηλεσκόπιο νεutrίνων KM3NeT είναι μια υποδομή τηλεσκοπίων νεutrίνων που θα τοποθετηθούν στα βάθη των θαλασσών και συγκεκριμένα στη Μεσόγειο Θάλασσα. Το KM3NeT στοχεύει στην ανίχνευση νεutrίνων από γαλαξιακές και εξωγαλαξιακές πηγές παραγωγής νεutrίνο. Αυτή η διατριβή περιγράφει μία μέθοδο για την ανακατασκευή της ενέργειας μιονίων και νεutrίνων στο τηλεσκόπιο KM3NeT.

Στο πρώτο κεφάλαιο περιγράφονται οι πηγές και οι μηχανισμοί παραγωγής των κοσμικών ακτίνων και των νεutrίνων. Οι κοσμικές ακτίνες αφορούν σε πρωτόνια ή βαρύτερους πυρήνες υψηλών ενεργειών που εισέρχονται στην ατμόσφαιρα της Γης με ισοτροπική ροή. Η σύνθεση και η ροή αυτής της ισοτροπικής ακτινοβολίας καθώς και ο σχηματισμός εκτεταμένων καταιονισμών εξαιτίας της αλληλεπίδρασης των υψηλοενεργειακών φορτισμένων σωματιδίων στην ατμόσφαιρα της Γης έχει μελετηθεί από διάφορα πειράματα. Ωστόσο, αν και το φάσμα των κοσμικών ακτίνων έχει μετρηθεί από διαφορετικά πειράματα, η προέλευσή τους παραμένει άγνωστη. Η έλλειψη γνώσης

της προέλευσης των κοσμικών ακτίνων καθώς και η περιορισμένη γνώση του υψηλο-ενεργειακού μέρους του φάσματός τους δίνει ώθηση στις αναζητήσεις για την εύρεση νετρίνων υψηλών ενεργειών.

Το φάσμα των κοσμικών ακτίνων εκτείνεται σε πολύ υψηλές ενέργειες υποδηλώνοντας έτσι την ύπαρξη αστροφυσικών πηγών ικανών να επιταχύνουν σωματίδια σε αυτές τις ενέργειες. Οι κοσμικές ακτίνες, όμως, δεν μπορούν να οδηγήσουν στον εντοπισμό των αστροφυσικών πηγών από τις οποίες προήλθαν καθώς εκτρέπονται από γαλαξιακά και διαγαλαξιακά μαγνητικά πεδία αλλάζοντας την αρχική τους διεύθυνση. Εντούτοις, οι πηγές παραγωγής των κοσμικών ακτίνων αναμένεται να παράγουν νετρίνο υψηλών ενεργειών μέσω των αλληλεπιδράσεων των κοσμικών ακτίνων με την ύλη μέσα ή γύρω από την πηγή. Σύμφωνα με θεωρητικά μοντέλα, τα νετρίνο παράγονται όταν πρωτόνια ή πυρήνες αλληλεπιδρούν με το πλάσμα ή το πεδίο ακτινοβολίας μέσα ή γύρω από την πηγή: η αλληλεπίδραση αυτή οδηγεί στην παραγωγή πιονίων, τα οποία παράγουν ένα νετρίνο ηλεκτρονίου και δύο νετρίνο μιονίου ($\pi^+ \rightarrow \mu^+ + \nu_\mu$, $\pi^- \rightarrow \mu^- + \bar{\nu}_\mu$ και $\mu^+ \rightarrow e^+ + \bar{\nu}_\mu + \nu_e$, $\mu^- \rightarrow e^- + \nu_\mu + \bar{\nu}_e$). Όσον αφορά στην παραγωγή νετρίνο, οι τρεις γεύσεις παράγονται σε ποσοστό $\nu_e : \nu_\mu : \nu_\tau = 1 : 2 : 0$ κατά τη διάρκεια διάσπασης των πιονίων. Ωστόσο, οι ταλαντώσεις νετρίνο μετατρέπουν αυτό το ποσοστό σε: $\nu_e : \nu_\mu : \nu_\tau = 1 : 1 : 1$ μέχρι να φτάσουν στη Γη. Τα υψηλοενεργειακά, φευγαλέα και ασθενώς αλληλεπιδρώντα νετρίνο ταξιδεύουν ανεπηρέαστα από την πηγή παραγωγής τους στη Γη και η ανίχνευσή τους μπορεί να παρέχει πληροφορίες για την προέλευση των κοσμικών ακτίνων, τους μηχανισμούς παραγωγής που λαμβάνουν χώρα στην πηγή και την κατανομή των πηγών νετρίνων στο Σύμπαν.

Διάφορες κατηγορίες αστροφυσικών αντικειμένων έχουν προταθεί ως υποψήφιος για την επιτάχυνση σωματιδίων. Οι πιθανές πηγές παραγωγής νετρίνων μπορούν να ταξινομηθούν σε πηγές γαλαξιακής και εξωγαλαξιακής προέλευσης. Στις πηγές παραγωγής νετρίνων μέσα στο Γαλαξία συμπεριλαμβάνονται μεταξύ άλλων τα υπολείμματα εκρήξεων σουπερνόβα, αέρια νεφελώματα από πάλσαρ και δυαδικά συστήματα αστέρων που εκπέμπουν ακτινοβολία στα μήκη κύματος των ακτίνων X. Οι πιθανές πηγές παραγωγής νετρίνων εξωγαλαξιακής προέλευσης αφορούν σε ενεργούς γαλαξιακούς πυρήνες, εκλάμψεις ακτίνων γ , γαλαξίες με μεγάλο πληθυσμό αστέρων με μεγάλη μάζα καθώς και νετρίνο που προέρχονται από την αλληλεπίδραση κοσμικών ακτίνων πολύ υψηλών ενεργειών με φωτόνια της ακτινοβολίας υποβάθρου.

Εκτός από τα νετρίνο που προέρχονται από αστροφυσικές πηγές, υπάρχουν και τα ατμοσφαιρικά νετρίνο που παράγονται κατά τη διάρκεια της αλληλεπίδρασης κοσμικών ακτίνων στην ατμόσφαιρα της Γης. Ανάμεσα στα άλλα σωματίδια που παράγονται στους καταιονισμούς, μόνο τα νετρίνο και τα μόνια που παράγονται κατά τις αντιδράσεις φορτισμένου ρεύματος των νετρίνο, μπορούν να φτάσουν τα υποθαλάσσια τηλεσκόπια νετρίνων. Τα ατμοσφαιρικά μόνια απορροφούνται από τη Γη και έτσι μπορούν να φτάσουν στον ανιχνευτή μόνο από κατευθύνσεις πάνω από τον ορίζοντα. Εντούτοις, αποτελούν ένα από τα πιο σημαντικά υπόβαθρα για τον ανιχνευτή. Για να μειώσουν το υπόβαθρο των ατμοσφαιρικών μιονίων, τα τηλεσκόπια νετρίνων τοποθετούνται σε μεγάλα βάρη (αρχικών χιλιομέτρων) καθώς η ροή ατμοσφαιρικών μιονίων μειώνεται σημαντικά με την

αύξηση του βάθους. Σε αντίθεση με τα ατμοσφαιρικά μίονια, τα ατμοσφαιρικά νετρίνο φτάνουν στον ανιχνευτή από όλες τις κατευθύνσεις αλλά ανιχνεύονται λιγότερο συχνά εξαιτίας της μικρής πιθανότητας αλληλεπίδρασής τους. Αν και τα ατμοσφαιρικά νετρίνο αποτελούν ένα υπόβαθρο για τα τηλεσκόπια νετρίνων που είναι δύσκολο να μειωθεί, αποτελούν μία πηγή βαθμονόμησης του ανιχνευτή και μια απόδειξη της αρχής λειτουργίας του τηλεσκοπίου νετρίνων.

Η ανίχνευση των νετρίνων στα υποθαλάσσια τηλεσκόπια νετρίνων βασίζεται στην ανίχνευση του φωτός που εκπέμπεται κατά τη διέλευση των σωματιδίων που προέρχονται από το νετρίνο μέσα στο θαλασσινό νερό. Η αρχή ανίχνευσης στα τηλεσκόπια νετρίνων, οι αντιδράσεις των νετρίνων με τη Γη ή το θαλασσινό νερό και η τοπολογία των γεγονότων που ανιχνεύονται στα τηλεσκόπια νετρίνων περιγράφεται στο δεύτερο κεφάλαιο αυτής της διατριβής. Επιπλέον, αναφέρονται οι κυριότερες πηγές υποβάθρου στα υποθαλάσσια τηλεσκόπια νετρίνων και γίνεται μια σύντομη επισκόπηση των τηλεσκοπίων IceCube και ANTARES.

Η αλληλεπίδραση φορτισμένου ρεύματος του νετρίνο του μιονίου που οδηγεί στην παραγωγή μιονίου αποτελεί το σημαντικότερο κανάλι διάσπασης για την αστρονομία νετρίνων. Η ανίχνευση των μιονίων που διαπερνούν τη Γη εγγυάται την προέλευσή τους από νετρίνο καθώς κανένα άλλο γνωστό σωματίδιο δεν μπορεί να διασχίσει τη Γη. Όταν ένα φορτισμένο σωματίδιο ταξιδεύει σε ένα διηλεκτρικό μέσο ταχύτερα από την ταχύτητα (φάσης) του φωτός στο μέσο αυτό, το φως που εκπέμπεται από τα διεγερμένα μόρια κατά μήκος της τροχιάς του σωματιδίου δημιουργεί ένα χαρακτηριστικό κώνο φωτός, τον κώνο Cherenkov. Στην περίπτωση των μιονίων, τα οποία ταξιδεύουν μεγάλες αποστάσεις στο θαλασσινό νερό πριν χάσουν την ενέργειά τους, αυτή η χαρακτηριστική γωνία εκπομπής φωτονίων (43°) χρησιμοποιείται για την ανακατασκευή της τροχιάς τους. Σε μεγάλες ενέργειες, η τροχιά του νετρίνο είναι σχεδόν συγραμμική με την τροχιά του μιονίου οπότε η ανακατασκευή της τροχιάς του μιονίου οδηγεί στον προσδιορισμό της τροχιάς του νετρίνο από το οποίο προήλθε. Η ανακατασκευή της τροχιάς του μιονίου βασίζεται στην ακριβή ανακατασκευή του κώνου Cherenkov. Για αυτό το λόγο, τα ανιχνευτικά στοιχεία ενός τηλεσκοπίου νετρίνων πρέπει να παρέχουν πολύ καλή χρονική ακρίβεια (σε επίπεδο ns) και παράλληλα να μπορούν να ανιχνεύσουν μεμεσωνωμένα φωτόνια. Οι φωτοπολλαπλασιαστές έχουν αυτές τις ιδιότητες και χρησιμοποιούνται ως τα πιο κατάλληλα ανιχνευτικά στοιχεία στα τηλεσκόπια νετρίνων.

Τα υπόβαθρα στα υποθαλάσσια τηλεσκόπια νετρίνων αποτελούνται από το φυσικό υπόβαθρο των ατμοσφαιρικών νετρίνων και μιονίων (όπως περιγράφηκε ανωτέρω) και από υπόβαθρα που οφείλονται σε περιβαλλοντικούς παράγοντες. Στα τελευταία περιλαμβάνονται το ραδιενεργό ^{40}K και η βιοφωταύγεια. Ειδικότερα, το ^{40}K είναι το πιο άφθονο ραδιενεργό στοιχείο στο θαλασσινό νερό. Οι διασπάσεις του δημιουργούν φορτισμένα σωματίδια τα οποία κατά τη διέλευσή τους μέσα στο θαλασσινό νερό παράγουν φωτόνια. Σε αντίθεση με τα Cherenkov φωτόνια που προέρχονται από το μίονιο, τα φωτόνια που προέρχονται από τις διασπάσεις του ^{40}K δεν εμφανίζουν χρονική συσχέτιση μεταξύ τους και έτσι μπορούν να διαχωριστούν ζητώντας χρονικές συμπτώσεις σε γειτονικούς φωτοπολλαπλασιαστές. Η βιοφωταύγεια αφορά στο φως που εκπέμπεται

από ζωντανούς οργανισμούς που ζουν στη βαθιά θάλασσα. Η ένταση του φωτός που προέρχεται από τη βιοφωταύγεια και η διάρκεια του φαινομένου ποικίλλει. Για παράδειγμα, τα βακτήρια τείνουν να εκπέμπουν φως σταθερά για μεγάλα χρονικά διαστήματα που διαρκούν από μερικές ώρες έως μερικές μέρες ενώ οργανισμοί μεγαλύτερου μεγέθους εκπέμπουν φως σε εκρήξεις με διάρκεια μερικών δευτερολέπτων.

Τα πιο πρόσφατα τηλεσκόπια νετρίνων είναι το ANTARES και το IceCube. Το τηλεσκόπιο ANTARES είναι το πρώτο τηλεσκόπιο νετρίνων στη Μεσόγειο Θάλασσα. Η πόντιση του τηλεσκοπίου ολοκληρώθηκε το 2008 και αποτελείται από 885 οπτικά στοιχεία. Το τηλεσκόπιο ANTARES καλύπτει έναν ανιχνευτικό όγκο περίπου 0.025 km^3 και αποτελεί τον πρόδρομο του τηλεσκοπίου KM3NeT που θα τοποθετηθεί στη Μεσόγειο Θάλασσα και θα καλύπτει όγκο μερικών κυβικών χιλιομέτρων. Το τηλεσκόπιο νετρίνων IceCube έχει όγκο 1 km^3 και είναι τοποθετημένο στον πάγο της Ανταρκτικής. Αποτελεί το μεγαλύτερο τηλεσκόπιο νετρίνων με 5160 οπτικά στοιχεία σε βάθος από 1450 έως 2450 m. Το τηλεσκόπιο νετρίνων IceCube παρατήρησε για πρώτη φορά ροή νετρίνων πολύ υψηλών ενεργειών. Ειδικότερα ανίχνευσε 37 νετρίνο με ενέργεια (που εναποτέθηκε μέσα στον ενεργό όγκο ανίχνευσης) περισσότερη από 30 TeV έως 2 PeV. Πρόσφατα, ανιχνεύτηκε ένα μιονίο πολύ υψηλής ενέργειας περίπου ίσης με 2.6 PeV ($\pm 0.3 \text{ PeV}$) το οποίο διέσχισε τον όγκο του ανιχνευτή. Αυτή η τιμή της ενέργειας του μιονίου που εναποτέθηκε μέσα στον όγκο του ανιχνευτή, αναμένεται από μιονίο με ενέργεια από 4 έως 5 PeV αποτελώντας το μιονίο με τη μεγαλύτερη ενέργεια που έχει ποτέ παρατηρηθεί.

Όπως έχει αναφερθεί παραπάνω, το KM3NeT είναι ένα δίκτυο υποθαλάσσιων τηλεσκοπίων νετρίνων που θα τοποθετηθεί στη Μεσόγειο Θάλασσα. Το KM3NeT αποτελείται από δύο διαφορετικούς σχηματισμούς ανιχνευτών, τον ανιχνευτή ARCA και τον ανιχνευτή ORCA. Ο ανιχνευτής ARCA είναι ένα τηλεσκόπιο νετρίνων αρκετών κυβικών χιλιομέτρων που στοχεύει στην ανίχνευση νετρίνων υψηλών ενεργειών (στην περιοχή των TeV) από γαλαξιακές και εξωγαλαξιακές πηγές. Ο ανιχνευτής ORCA καλύπτει έναν όγκο αρκετών κυβικών μέτρων και στοχεύει στη μέτρηση της ιεραρχίας μαζών των νετρίνων χρησιμοποιώντας τις ταλαντώσεις των ατμοσφαιρικών νετρίνων (στην περιοχή των GeV) που διασχίζουν τη Γη. Το δίκτυο ανιχνευτών KM3NeT και ειδικότερα ο ανιχνευτής ARCA περιγράφεται στο τρίτο κεφάλαιο. Σε αυτό το κεφάλαιο, παρουσιάζεται ο σχεδιασμός του ανιχνευτή και περιγράφονται τα στοιχεία ανίχνευσης, η ανάκτηση δεδομένων και οι τεχνικές διαχωρισμού του σήματος από το υποβάθρο. Στο ίδιο κεφάλαιο δίνεται μια σύντομη περιγραφή των πακέτων λογισμικού που χρησιμοποιούνται για τις προσομοιώσεις νετρίνων και μιονίων με τη μέθοδο Monte Carlo.

Η πρώτη φάση του ανιχνευτή ARCA αποτελείται από δύο δομικές μονάδες που θα τοποθετηθούν σε βάθος 3500 m στην περιοχή του Capo Passero, ανατολικά της ακτής της Σικελίας, και θα καλύπτουν έναν ενεργό όγκο περίπου ενός κυβικού χιλιομέτρου. Κάθε δομική μονάδα είναι μία σχεδόν κυλινδρική ανιχνευτική διάταξη που αποτελείται από 115 ανιχνευτικές μονάδες, που αναφέρονται ως σειρές. Στην τελική φάση, ο ανιχνευτής ARCA θα αποτελείται από έξι δομικές μονάδες συνιστώντας έναν όγκο ανίχνευσης αρκετών κυβικών χιλιομέτρων (που εξαρτάται από την απόσταση ανάμεσα στις

σειρές ανίχνευσης). Υπάρχουν άλλες δύο προτεινόμενες περιοχές εγκατάστασης των υπολοίπων τεσσάρων δομικών μονάδων του ανιχνευτή: η περιοχή της Toulon με βάθος 2475 m και η περιοχή της Πύλου στο ανατολικό Ιόνιο με τρία πιθανά βάθη στα 5200 m, 4500 m και 3750 m. Οι φυσικές, γεοφυσικές και ωκεανογραφικές ιδιότητες αυτών των περιοχών έχουν μελετηθεί διεξοδικά και ικανοποιούν τις απαιτήσεις για την τοποθέτηση ενός τηλεσκοπίου νετρίνων. Συγκεκριμένα, το νερό σε αυτές τις περιοχές έχει πολύ καλές οπτικές ιδιότητες, χαμηλά ποσοστά βιοφωταύγειας και βακτηριακής εναπόθεσης στα οπτικά στοιχεία του ανιχνευτή, χαμηλές ταχύτητες των θαλασσιών ρευμάτων και μικρή πιθανότητα να συμβούν ισχυρές σεισμικές δονήσεις. Επίσης, οι περιοχές αυτές είναι αρκετά κοντά στην ακτή διευκολύνοντας την τοποθέτηση του ανιχνευτή και μειώνοντας το κόστος καλωδίου για παροχή ρεύματος και μεταφορά δεδομένων από τον ανιχνευτή στην ακτή.

Κάθε σειρά ανίχνευσης του τηλεσκοπίου ARCA έχει 18 οπτικά στοιχεία που είναι τοποθετημένα κατακόρυφα σε απόσταση 36 m μεταξύ τους. Κάθε σειρά ανίχνευσης έχει ύψος περίπου 600 m ενώ το πρώτο οπτικό στοιχείο απέχει περίπου 100 m από τον πυθμένα. Οι σειρές ανίχνευσης στερεώνονται με τη βοήθεια άγκυρας στον πυθμένα και διατηρούνται σε κατακόρυφη θέση με τη βοήθεια πλευστήρα στην κορυφή. Κατά μήκος των σειρών ανίχνευσης υπάρχουν οπτικοηλεκτρικά καλώδια για παροχή ρεύματος στα οπτικά στοιχεία και καλώδια οπτικών ινών για επικοινωνία με την ακτή. Κάθε οπτικό στοιχείο είναι μία γυάλινη σφαίρα (ανθεκτική στις υψηλές πιέσεις) με διάμετρο 17 ιντσών (432 mm) στην οποία είναι τοποθετημένοι 31 φωτοπολλαπλασιαστές με εμβαδό φωτοκαθόδου περίπου 3 ιντσών (72 mm) μαζί με τα ηλεκτρονικά τους. Κάθε φωτοπολλαπλασιαστής περιβάλλεται από κάτοπτρο κωνικού σχήματος που αυξάνει τη διάμετρο της φωτοκαθόδου σε 95 mm. Αυτό το κωνικό κάτοπτρο βοηθάει να συλλέγονται φωτόνια τα οποία δε θα ανιχνεύονταν διαφορετικά. Μέσα σε κάθε οπτικό στοιχείο υπάρχουν, επίσης, μια πυξίδα, ένα κλισιόμετρο και ακουστικοί πιεζοηλεκτρικοί αισθητήρες οι οποίοι επιτρέπουν τη βαθμονόμηση της θέσης των φωτοπολλαπλασιαστών με ακρίβεια 10 cm. Η ακρίβεια στη θέση και τη διεύθυνση των φωτοπολλαπλασιαστών σε συνδυασμό με τον ακριβή χρονικό προσδιορισμό των παλμών, που επιτυγχάνεται με ακρίβεια 2 ns, είναι απαραίτητη για την ακριβή ανακατασκευή της τροχιάς του μιονίου. Η βαθμονόμηση του χρόνου των φωτοπολλαπλασιαστών πραγματοποιείται στην ακτή πριν την πόντιση και στη συνέχεια παρακολουθείται με τη βοήθεια λέιζερ (laser) που είναι τοποθετημένα στο βυθό και LED τα οποία είναι τοποθετημένα μέσα στα οπτικά στοιχεία. Τα δεδομένα που συλλέγονται στους φωτοπολλαπλασιαστές μεταφέρονται στα κουτιά σύνδεσης που είναι τοποθετημένα στον πυθμένα και από εκεί στην ακτή μέσω ενός δικτύου οπτικοηλεκτρικών καλωδίων.

Οι φωτοπολλαπλασιαστές καταγράφουν το χρόνο άφιξης και το πλάτος του φωτός Cherenkov που εκπέμπεται από τα μόνια και άλλα φορτισμένα σωματίδια κατά τη διέλευσή τους από το θαλασσινό νερό. Το φως που καταγράφεται χρησιμοποιείται για την ανακατασκευή της τροχιάς και της ενέργειας των μιονίων και κατά συνέπεια των νετρίνων. Η κατεύθυνση του νετρίνου είναι σχεδόν συγγραμμική με αυτή του μιονίου για νετρίνο υψηλών ενεργειών. Έτσι, η ανακατασκευή της τροχιάς του μιονίου οδηγεί

στον προσδιορισμό της κατεύθυνσης του νετρίνο. Ο αλγόριθμος που χρησιμοποιείται για την ανακατασκευή της τροχιάς των μιονίων περιγράφεται στο τέταρτο κεφάλαιο αυτής της διδακτορικής διατριβής. Αυτός ο αλγόριθμος ανακατασκευής ονομάζεται Chameleon reconstruction και αποτελείται από δύο μέρη. Το ένα μέρος είναι η αναγνώριση προτύπων που περιλαμβάνει αλγορίθμους για την επιλογή και την ταξινόμηση των παλμών στους φωτοπολλαπλασιαστές και το δεύτερο μέρος αφορά στην ανακατασκευή της τροχιάς του μιονίου που πραγματοποιείται με έναν αλγόριθμο ελαχιστοποίησης του χ^2 . Στο πείραμα KM3NeT υπάρχει και μία άλλη μέθοδος ανακατασκευής της τροχιάς του μιονίου, η οποία χρησιμοποιεί μία συνάρτηση πυκνότητας πιθανότητας για τον προσδιορισμό της κατεύθυνσης του μιονίου. Αυτός ο αλγόριθμος ονομάζεται recoLNS και η σύγκρισή του με το Chameleon, μετά από τις βελτιώσεις που πραγματοποιήθηκαν, περιγράφεται στο τέταρτο κεφάλαιο.

Η ανακατασκευή της ενέργειας του μιονίου και του νετρίνο είναι ζωτικής σημασίας για τα τηλεσκόπια νετρίνων. Το φάσμα των νετρίνων αστροφυσικής προέλευσης που συνιστούν το σήμα του ανιχνευτή εκτείνεται σε υψηλότερες ενέργειες σε σχέση με το υπόβαθρο των ατμοσφαιρικών νετρίνων που φτάνουν στον ανιχνευτικό όγκο και προσομοιάζουν το σήμα. Η εκτίμηση της ενέργειας είναι, λοιπόν, απαραίτητη για το διαχωρισμό των νετρίνων και των μιονίων, που προέρχονται από αντιδράσεις φορτισμένου ρεύματος των αστροφυσικών νετρίνων με το νερό ή το βράχο γύρω (κάτω) από τον ανιχνευτή, από τα ατμοσφαιρικά νετρίνο και μόνια. Επιπλέον, η εκτίμηση της ενέργειας είναι καίριας σημασίας για διάφορες μελέτες που αφορούν στον προσδιορισμό των πηγών νετρίνων, όπως έρευνες για σημειακές πηγές παραγωγής νετρίνων.

Η μέθοδος υπολογισμού της ενέργειας μιονίων και νετρίνων που αναπτύχθηκε, περιγράφεται στο πέμπτο κεφάλαιο αυτής της διατριβής. Για την ανακατασκευή της ενέργειας του μιονίου και του νετρίνο εκπαιδεύτηκε ένα Νευρωνικό Δίκτυο στο οποίο εισήχθησαν κατάλληλες μεταβλητές που εμφανίζουν άμεση εξάρτηση με την ενέργεια του μιονίου. Οι μεταβλητές αυτές αφορούσαν στον αριθμό των οπτικών στοιχείων και στον αριθμό των φωτοπολλαπλασιαστών που έχουν ανιχνεύσει παλμούς, στον αριθμό των φωτοπολλαπλασιαστών που δεν έχουν ανιχνεύσει παλμούς παρόλο που βρίσκονται στο μέτωπο του κύματος Cherenkov και στον ολικό χρόνο των παλμών πάνω από το κατώφλι. Αυτή η μέθοδος υπολογισμού της ενέργειας εφαρμόστηκε σε γεγονότα που είχαν ανακατασκευασθεί με τους δύο διαφορετικούς αλγορίθμους, το Chameleon και το recoLNS. Τα αποτελέσματα και στις δύο περιπτώσεις ήταν πολύ καλά ενώ η ενεργειακή διακριτική ικανότητα που επιτεύχθηκε αντιστοιχεί σε περίπου 0.25 για μόνια με ενέργειες στην περιοχή των TeV. Η ανακατασκευή της ενέργειας του νετρίνο πραγματοποιήθηκε για γεγονότα τα οποία αλληλεπιδρούν μέσα στον όγκο του ανιχνευτή ώστε να μπορούν να ανιχνευθούν τα φωτόνια από τον αδρονικό καταιονισμό και τα φωτόνια που προέρχονται από τη διέλευση του μιονίου στο θαλασσινό νερό. Για τα γεγονότα που δεν αλληλεπιδρούν μέσα στον ενεργό όγκο ανίχνευσης μπορεί να υπολογιστεί μόνο ένα κατώτερο όριο της ενέργειας των νετρίνων που αντιστοιχεί στην ενέργεια του μιονίου, καθώς τα φωτόνια από τον αδρονικό καταιονισμό δεν μπορούν να ανιχνευθούν από τους φωτοπολλαπλασιαστές.

Στο έκτο κεφάλαιο αυτής της διατριβής υπολογίζεται η τιμή της ευαισθησίας (sensitivity) του ανιχνευτή και της δυνατότητας ανακάλυψης (discovery potential) νετρίνων με το τηλεσκόπιο KM3NeT – ARCA λαμβάνοντας υπόψη την αστροφυσική ροή νετρίνων όπως μετρήθηκε από το πείραμα IceCube. Η ευαισθησία του ανιχνευτή είναι το καλύτερο όριο που μπορεί να τεθεί στη ροή νετρίνων από μία αστροφυσική πηγή σε ένα διάστημα εμπιστοσύνης (90%) αν δεν έχει ανιχνευθεί σήμα. Η δυνατότητα ανακάλυψης αντιστοιχεί στη ροή που πρέπει να έχει η πηγή παραγωγής νετρίνων ώστε αν υπάρχει σήμα από νεutrino να ανιχνεύεται με βεβαιότητα 5σ σε ένα ποσοστό (50%) των πειραμάτων. Για τους παραπάνω υπολογισμούς χρησιμοποιείται η ανακατασκευασμένη ενέργεια του μιονίου. Με αυτό τον τρόπο η περιορισμένη ακρίβεια στον προσδιορισμό της ενέργειας, που αντιστοιχεί στην ενεργειακή διακριτική ικανότητα της μεθόδου, εισάγει μια αβεβαιότητα στους παραπάνω υπολογισμούς. Η αβεβαιότητα αυτή υπολογίστηκε και ορίστηκε ένα διάστημα αβεβαιότητας στο οποίο αναμένεται να κυμαίνονται οι τιμές για την ευαισθησία και τη δυνατότητα ανακάλυψης νετρίνων με το τηλεσκόπιο KM3NeT – ARCA.

Abstract

Humans were always curious about the sky and the unveiled mysteries of our Universe. They started observing the sky with telescopes detecting photons at different wavelengths of the electromagnetic spectrum. Photons are widely used in astronomy as they travel in straight lines and come directly from the spot of the sky whence they originated. However, photons can be absorbed by interstellar matter thus not reaching the Earth when traveling intergalactic distances. On the other hand, charged particles, that can also be used as cosmic messengers, are deviated by magnetic fields, reaching the Earth with different directions than their initial ones. In this way, charged particles cannot provide information about their point of origin in the sky.

Unlike photons or charged particles, neutrinos can emerge from deep inside their sources of origin and travel undeflected across the universe. Neutrinos, being neutral, do not interact with magnetic fields and are not absorbed by interstellar matter thus pointing back to their sources. These properties make neutrinos ideal for cosmic messengers. However, neutrinos interact weakly with matter and large instrumented volumes are necessary in order to detect neutrinos in sufficient statistics to trace their origin. Neutrino telescopes are deployed in the sea, lakes or ice and aim to detect neutrinos that have crossed the Earth and interact in or in the vicinity of the telescope. Neutrinos are detected indirectly, by the light collected in photomultipliers during the interaction of neutrino-induced particles with the medium (sea/ lake water or ice). The light in photomultipliers is used for the reconstruction of the neutrino direction and the estimation of the neutrino energy.

KM3NeT is an infrastructure of deep-sea water neutrino telescopes in the Mediterranean Sea. This neutrino telescope aims to detect neutrinos from galactic and extragalactic neutrino sources. This thesis describes a method for the muon and neutrino energy reconstruction for the KM3NeT neutrino telescope. In the first chapter, the sources and the production mechanisms of Cosmic Rays and neutrinos are described. The detection principle of neutrino telescopes and the signal and background sources are outlined in the second chapter. In addition, the main existing neutrino telescopes are presented in this chapter. In the third chapter of this thesis, the KM3NeT project is discussed providing information about the detector design, its detection units, the data acquisition and event triggering processes as well as the software packages used for the Monte Carlo simulation of neutrinos. The algorithm used to reconstruct the direction of the neutrino-induced muon tracks, and consequently the neutrino direction reconstruction, is described in the fourth chapter. The performance of this reconstruction is presented before and after the improvements that were made and the results are also compared with another track reconstruction package. The muon and neutrino energy reconstruction is described in chapter 5. The method that was developed for the muon and neutrino energy estimation is analysed. This method employs a Neural Network with appropriate input variables to determine the muon and neutrino energy. The energy resolution achieved with this method is approximately 0.25 in $\log_{10} E_\mu$ for muons at the TeV energy range. Finally, the sensitivity and discovery potential of the KM3NeT neutrino telescope for the detection of high energy neutrinos from astrophysical sources is discussed in chapter 6. The astrophysical neutrino flux that was recently measured by the IceCube Collaboration is used and the uncertainty introduced by the energy estimator is investigated.

Contents

1	Cosmic Rays and Neutrino Production	1
1.1	Cosmic Rays	1
1.1.1	The Cosmic Ray Spectrum	2
1.1.2	Shock Acceleration	4
1.2	Astrophysical Neutrinos	6
1.2.1	Candidate Sources for Astrophysical Neutrinos	7
1.2.1.1	Extragalactic sources	8
1.2.1.2	Galactic sources	10
1.2.2	Neutrino Production from Hadronic processes	11
1.3	Atmospheric Neutrinos and Muons	12
2	Neutrino Telescopes	15
2.1	Detection Principles	15
2.1.1	Neutrino Interactions	17
2.1.2	Cherenkov light	21
2.1.3	Light propagation and detection	23
2.1.4	Event Signatures	24
2.1.5	Detector Backgrounds for Underwater Neutrino Telescopes	26
2.2	The Main Existing Neutrino Telescopes	29
2.2.1	ANTARES	30
2.2.2	IceCube	31
3	The KM3NeT Project - ARCA Detector	35
3.1	Detector Design	35
3.1.1	Detection Units	40
3.1.2	Optical Modules	41

CONTENTS

3.1.3	Deep Sea Tests of Prototype Optical Module and Detection Unit of the KM3NeT detector	45
3.1.4	Data Acquisition and Event Trigger	47
3.2	Generation and Simulation Packages	48
3.2.1	The detector geometry	49
3.2.2	Neutrino event generation	51
3.2.3	MUPAGE: An atmospheric muon generator	53
3.2.4	The KM3 simulation package	54
3.2.5	JTriggerEfficiency: Generation of pulses and optical background in PMTs and event triggering	55
3.2.5.1	Generation of pulses and optical background in PMTs	55
3.2.5.2	Event triggering	56
4	Track Reconstruction	57
4.1	The Chameleon Track Reconstruction	57
4.1.1	Hits Pattern Recognition	58
4.1.2	Fitting Algorithm	59
4.2	Performance of the Track Reconstruction	59
4.3	Reconstruction Improvements	63
4.4	Performance of the Track Reconstruction for an Alternative Detector Configuration	71
4.5	Comparison between the Chameleon and the recoLNS Reconstruction Package	74
5	Energy Reconstruction with Neural Networks (EReNN)	79
5.1	Scientific Motivation	79
5.2	Data Selection	81
5.3	Artificial Neural Networks	84
5.3.1	Multi-Layer Perceptron Neural Network	85
5.4	Input Parameters of the Neural Network	86
5.5	Training the Neural Network	90
5.6	Performance of the Energy Reconstruction	92
5.7	Efficiency of the Energy Reconstruction	95
5.8	Estimating the Energy for Reconstructed Events with the recoLNS Track Reconstruction Algorithm	96

5.8.1	Performance of the Energy Reconstruction	99
5.8.2	Contribution of Background in the Energy Estimation . .	102
5.8.3	Efficiency of the Energy Reconstruction	104
5.8.4	Systematic Uncertainties	106
5.8.5	Neutrino Energy Reconstruction	107
5.9	Estimating the Energy for an Alternative Detector Configuration	110
6	Sensitivity and Discovery Potential	115
6.1	Sensitivity	116
6.2	Discovery Potential	117
6.3	Calculations of the Sensitivity and the Discovery Potential for the KM3NeT detector	119
6.4	Improvements on the Energy Reconstruction	124
6.4.1	Training the Neural Network	127
6.4.2	Performance of the Improved Energy Reconstruction . . .	128
6.5	Calculations for KM3NeT detector using the Improved Energy Reconstruction	130
6.6	Uncertainty introduced by the energy estimator	134
7	Conclusion	139
	Bibliography	141

CONTENTS

1

Cosmic Rays and Neutrino Production

1.1 Cosmic Rays

Cosmic Rays (CRs) are high energy protons or heavy nuclei that enter the atmosphere of the Earth with an isotropic flux. Their initial detection lies back in 1912, when Victor Hess discovered, during his balloon experiments, that the ionizing radiation, already detected on Earth, increased with increasing altitude. In the following decades, several experiments studied the composition and the flux of this isotropic radiation and the form of extensive air showers due to the interaction of high energy charged primaries with the atmosphere. Although, the Cosmic Ray spectrum was measured by different experiments, the origin of CRs remains a mystery. This lack of knowledge for the origin of CRs along with the limited knowledge of the high energy part of their spectrum motivates the searches for high energy neutrinos.

The spectrum of CRs extends to very high energies thus suggesting the existence of astrophysical sources able to accelerate particles at such energies. CRs though, cannot point back to the astrophysical sources as they are deflected by galactic and intergalactic magnetic fields. However, the sources of CRs are expected to produce high energy neutrinos via the interactions of CRs with the medium in or around the source. The detection of high energy, elusive and weakly interacting neutrinos can then provide information about the origin of CRs, the production mechanisms taking place at the source and the distribution of neutrino sources in the Universe, as neutrinos can travel undeflected from the

1. COSMIC RAYS AND NEUTRINO PRODUCTION

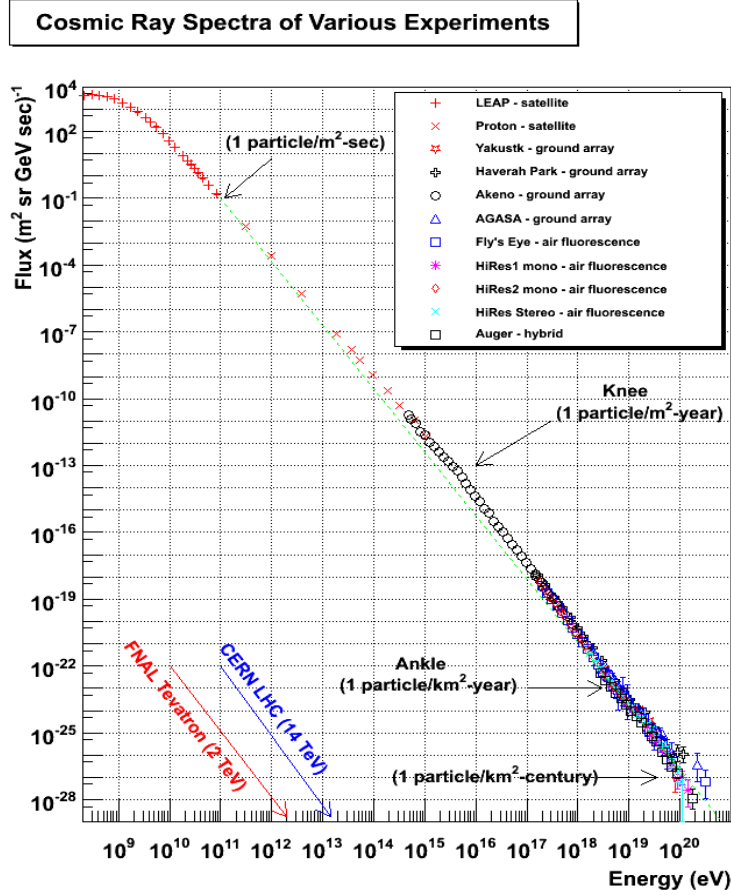


Figure 1.1: The Cosmic Ray spectrum as it was measured by different experiments [1].

source to the Earth.

The spectrum of CRs, the possible mechanisms by which they are accelerated and the theoretical models that predict the production of neutrinos at astrophysical sources are discussed in the following sections.

1.1.1 The Cosmic Ray Spectrum

The Cosmic Ray (CR) spectrum as it has been measured by different experiments is shown in Figure 1.1. This spectrum can be described by a power law:

$$dN/dE \propto E^{-\gamma} \quad (1.1)$$

where γ is the spectral index and corresponds to $\gamma \simeq 2.7$ for energies up

to approximately $3 \cdot 10^{15}$ eV. Above this energy, the spectrum becomes steeper with $\gamma \simeq 3$ and this change of slope is referred as the *knee*, while above energies around $4 \cdot 10^{18}$ eV, the spectrum becomes harder again, entering an energy region which is known as the *ankle* [2].

For a relativistic particle with electric charge q and energy E in a magnetic field B , the radius of gyration is given by the Larmor radius $R_L = E/q \cdot B$. In the Galactic magnetic field protons with energies up to 10^{18} eV have a Larmor radius which is smaller than the size of the Galaxy and so can remain confined to the Galaxy. For energies up to the *knee* CRs are therefore thought to have a Galactic origin. According to many theoretical models, the *knee* signs the energy region in which the composition of CRs gradually changes from lighter to heavier nuclei. These heavier nuclei have larger electric charges and therefore need to be accelerated to larger energies in order to get similar R_L as protons.

For energies above 10^{18} eV the extragalactic component begins to dominate leading to a harder spectrum of CRs. The statistics is very small for energies above $\simeq 10^{19}$ eV and several experimental efforts have not managed to reach definite conclusions about the dominance of light or heavier nuclei in the composition of CRs. The mass composition of CRs with energies above $\simeq 10^{18}$ eV, that are usually referred as Ultra High Energy Cosmic Rays (UHECRs), is critical for astronomy with protons as ultra high energy protons can reach the Earth with minimal deflection by magnetic fields thus pointing back to the astrophysical sources of production [3]. Theoretical models suggest the interaction of these ultra high energy protons with photons from the Cosmic Microwave Background (CMB) with temperature at approximately 2.7°K via the Δ resonance, as indicated below:



The aforementioned interaction of protons with photons from the CMB radiation limits their range to approximately 50 Mpc as calculated by the formula of the absorption length of ultra high energy protons ($\simeq 10^{19}$ eV) in the Universe $L_{p,\gamma\text{CMB}} \simeq (n_\gamma \cdot \sigma_{p\gamma})^{-1}$, where n_γ is the average CMB radiation density and $\sigma_{p\gamma}$ the cross section of $p\gamma$ interaction for the Δ resonance ¹. This limitation of

¹Ultra high energy protons also interact with CMB photons via pair production. The absorption length of protons is then ~ 500 Mpc. Pair production is thus not responsible for the rapid decrease of the CR spectrum as it is described in [4]

the range of UHECRs is known as the Greisen-Zatsepin-Kuz'min cutoff (GZK-cutoff) and imposes a theoretical upper limit of few $\simeq 10^{19}$ eV on the energy of cosmic rays from distant cosmological sources that can reach the Earth.

1.1.2 Shock Acceleration

The origin of CRs and in particular of the UHECRs remains unknown. However, the observed CR spectrum that follows a power law: $\frac{dN}{dE} \sim E^{-2.7}$ can be theoretically interpreted by a diffusive shock acceleration mechanism, known as the first order Fermi acceleration, considered as a plausible mechanism for the acceleration of particles to the high energies observed in CRs [5], [6].

According to the Fermi acceleration mechanism, the CR particles are accelerated during multiple elastic scatterings with the magnetic irregularities contained in the plasma of the source. The charged CR particles that are magnetically confined to the source, manage to escape together with the shocked material only after several scatterings, resulting to an increase of their energy. In particular, the Fermi acceleration can occur when two plasmas collide, forming a shock at the boundary as it is shown in Figure 1.2. In the generic case, these two plasmas have different velocities. Assuming that the velocity of the upstream plasma flow, V_1 , (Figure 1.2(a)) is much larger than the downstream velocity, V_2 , an energetic particle that is injected at the shock to upstream flow will gain energy. This energy gain comes from the collision of the particle with the fast waves of the upstream flow. Then the particle is reflected to the downstream plasma flow. When this particle moves downstream, it is reflected in a collision with the downstream waves back upstream. During this collision with the slow waves of the downstream flow, the particle loses energy. However, this energy loss is small compared to the energy gain obtained during the multiple scatterings with the upstream flow. Thus, the energy of the particle does not increase significantly during one single reflection and multiple elastic scatterings between the upstream and downstream flow are required for a significant energy gain. The particle acceleration depends on the scattering process, which is a stochastic process, and on the presence of magnetic irregularities that act as scattering centers. Finally, the particle escapes from the shock if it can no longer be confined to the source or if the shock decays and ends up in free space as a Cosmic Ray particle of very high energy.

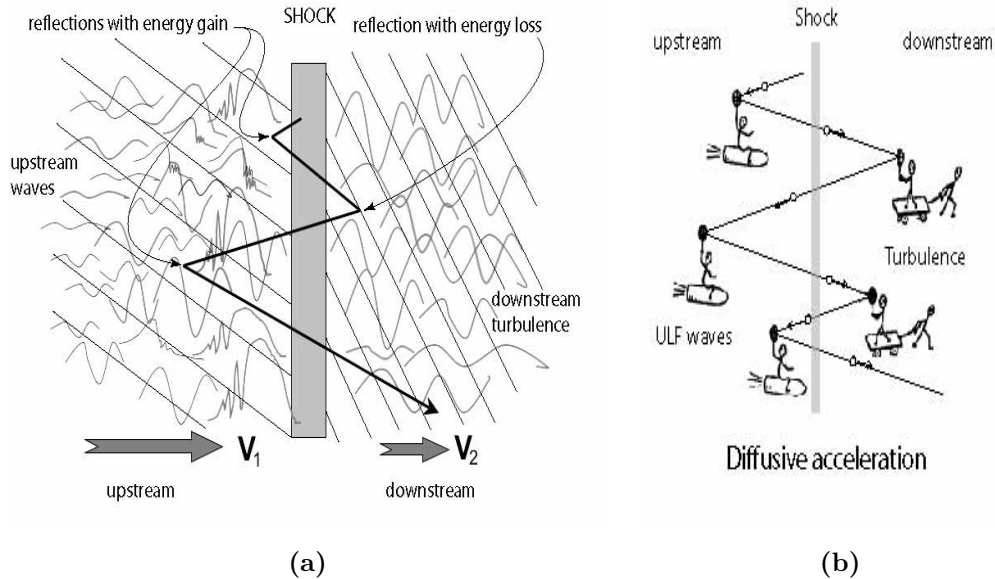


Figure 1.2: A schematic representation (a) and a cartoon (b) of the acceleration mechanism of a charged particle in reflection at a shock. During this process the particle is scattered around the shock being much faster than the shock. The requirement is the presence of upstream waves and downstream turbulence or waves [7].

The spectrum predicted by the shock acceleration mechanism can then be estimated. The average fractional energy gain of the CR particle every time it goes back and forth the shock front is:

$$\left\langle \frac{\Delta E}{E} \right\rangle \sim \frac{(V_1 - V_2)}{c} \quad (1.4)$$

where E is the initial energy of the relativistic particle entering the shock [7]. Apart from this constant increase of energy, each particle has a probability, P_{esc} , to escape the shock. This probability can be derived from the ratio R_{loss}/R_{cross} , where R_{loss} is the rate at which the CR particle enters the downstream flow and is advected away from the shocked region together with the shocked material with velocity $\frac{(V_1 - V_2)}{4}$ and R_{cross} is the rate at which the CR particle crosses from the upstream to downstream flow, assuming an isotropic CR flux entering the upstream region. Then the probability for a CR particle to escape the shock is:

$$P_{esc} = \frac{R_{loss}}{R_{cross}} = \frac{\rho(V_1 - V_2)/4}{c\rho/4} = \frac{(V_1 - V_2)}{c} \quad (1.5)$$

where ρ is the density of CRs [8]. The combination of these effects gives rise to a power law spectrum:

$$\frac{dN}{dE} \sim E^{-1 + \frac{\ln(1-P_{esc})}{\ln(1+\Delta E/E)}} \quad (1.6)$$

where $P_{esc} \ll 1$ and $\Delta E/E \ll 1$ thus leading to a spectrum of protons proportional to E^{-2} [9]. However, the observed CR spectrum is steeper with a larger spectral index than the one predicted above. Many theories try to explain this steepness of the spectrum with different models for the galactic and extragalactic component of CRs. The high energy CRs with a galactic origin, are thus theoretically expected to have a higher probability to escape the galactic magnetic field leading to a steeper spectrum. For extragalactic CRs, the redshift and the GZK effect most probably influence the steepness of the observed spectrum. The shape of the spectrum at very high energies is thus related to the distribution of CRs sources in the Universe [10].

1.2 Astrophysical Neutrinos

Astrophysical neutrinos (and anti-neutrinos)¹ are created in interactions of the high-energy cosmic rays with other massive particles or photons. In a first approximation, the energy spectrum of astrophysical neutrinos follows that of cosmic rays at their acceleration sites while second order corrections on this approximation can arise from muon energy losses [11] and muon acceleration [12].

An overview of the neutrino spectrum is shown in Figure 1.3. The lowest part of the neutrino spectrum consists of ν from the Cosmic Neutrino Background ($C\nu B$). $C\nu B$ is an isotropic neutrino flux coming from neutrinos that decoupled in the Early Universe. The temperature of the black body spectrum has dropped to $\sim 1.9^\circ\text{K}$ due to the expansion of the Universe, and the flux peaks at meV energies. Compared to the CMB, the $C\nu B$ radiation has lower temperature as the e^-e^+ annihilation that ensued at later stages of the evolution of the Universe resulted in an increase of the CMB temperature. Although, the $C\nu B$ is theoretically predicted, it cannot be directly measured with the current experimental techniques. At higher energies (approximately at the MeV energy range) neutrinos produced by fusion processes in the Sun and neutrinos from the Supernova

¹When neutrinos are mentioned, anti-neutrinos will always be implied throughout this thesis.

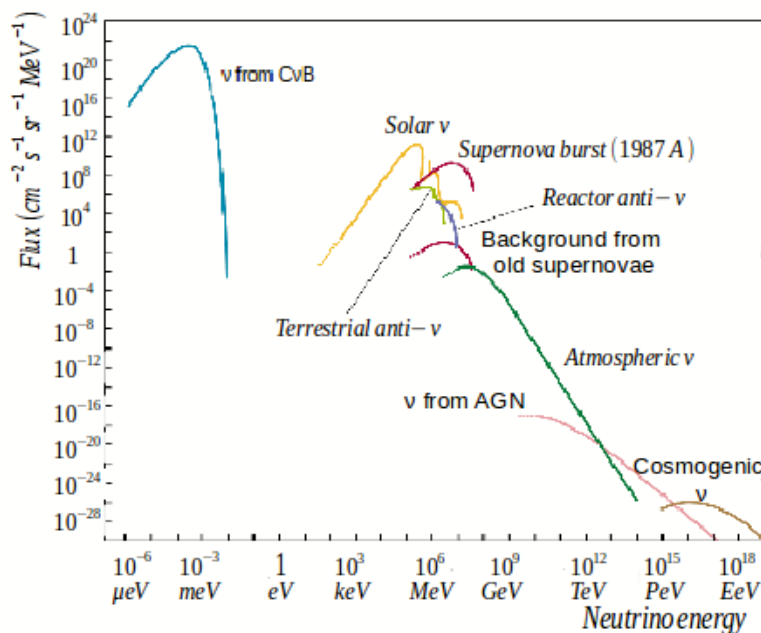


Figure 1.3: The astrophysical neutrino spectrum with measured and expected fluxes of natural and reactor neutrinos [13].

burst 1987A are shown. Neutrinos from these sources have been detected, as have neutrinos from the interior of the Earth. The experimentally measured atmospheric neutrino spectrum, that refers to neutrinos produced by CR interactions in the Earth’s atmosphere, is also shown at energies $E_\nu > 0.1\text{GeV}$. At the highest energies theoretically predicted neutrinos from astrophysical sources, such as Active Galactic Nuclei and cosmogenic neutrinos produced by interactions of ultra high energy protons with the cosmic microwave background, are depicted. Neutrino telescopes with instrumented volumes of several cubic kilometers aim to detect these high energy neutrinos [4], [13].

1.2.1 Candidate Sources for Astrophysical Neutrinos

Several astrophysical object classes have been proposed as potential particle accelerators. The existence of observational data in the whole electromagnetic wavelength range however, has not shed light on whether the non-thermal processes in these objects are of electronic or hadronic nature. The possible observation of neutrinos from these sources is expected to provide more information about the processes that take place inside such astrophysical objects. Neutri-

1. COSMIC RAYS AND NEUTRINO PRODUCTION

neutrinos emerge when protons or nuclei interact with plasma or with a radiation field within or surrounding the source: the interaction produces pions, whose decay produces one electron neutrino and two muon neutrinos ($\pi^+ \rightarrow \mu^+ + \nu_\mu$, $\pi^- \rightarrow \mu^- + \bar{\nu}_\mu$ and $\mu^+ \rightarrow e^+ \bar{\nu}_\mu \nu_e$, $\mu^- \rightarrow e^- \nu_\mu \bar{\nu}_e$). Each neutrino carries 5% of the energy, per nucleon of the parent cosmic-ray particle. But unlike charged cosmic rays, neutrinos, being neutral, are not deflected by magnetic fields on their trajectory to Earth. This provides the advantage that neutrino measurements can be compared to light from the same potential source. And unlike photons, neutrinos can escape from deep within a source, carrying useful information about its physics.

The candidate neutrino sources can be classified in sources of galactic and extragalactic origin and are briefly described in the following sections.

1.2.1.1 Extragalactic sources

The diffuse neutrino flux is expected to be derived from the cosmological distribution of extragalactic sources that are responsible for both the CR spectrum above the ankle and the neutrino spectrum [14]. The most plausible extragalactic candidates for the emission of high energy neutrinos are:

Active Galactic Nuclei: Active Galactic Nuclei (AGN) are associated with galaxies with a super-massive black hole of $10^6 - 10^9$ solar masses in their center. The energy that is released by these objects is provided by the transformation of huge amounts of gravitational energy into radiation during the accretion of matter into the black hole. AGNs are very luminous objects releasing energy typically of the order of 10^{47} erg/s [13]. In some cases, AGNs are observed to emit relativistic jets. Such AGNs with the jet aligned closely to the line of sight are called blazars and have proved to be strong gamma ray emitters. According to some models, neutrinos are expected to be produced both in the accretion disk, where thermal photons provide the target for photo-meson production, and in the jets, where the target can also consist of synchrotron photons. Blazars are thus good candidate point sources for neutrino observation with a neutrino flux that is expected to be rather significant due to the flux enhancement in the jet via Doppler broadening [4], [15].

Gamma Ray Bursts: Gamma Ray Bursts (GRBs) are very luminous eruptions that release huge amounts of energy ($\geq 10^{51} \text{ erg/s}$) in gamma rays within milliseconds to minutes. The main burst is usually followed by a late afterglow

emission in X-ray, optical and radio wavelengths. GRBs are classified according to the duration of the gamma ray emission and to the hardness of the spectrum to "long" GRBs, with duration ≥ 2 s, and "short" GRBs, with duration < 2 s. These two GRB classes are associated with different progenitors, considering the core collapse of a massive star scenario for the explanation of "long" GRBs and the compact merge of two neutron stars or the merge of a black hole with a neutron star as the possible progenitor for "short" GRBs.

The most favored model for the explanation of the emissions of gamma rays in "long" GRBs is the so-called *fireball* model [16],[17], while analogous models have been constructed to explain the gamma ray emission at "short" GRBs. According to this model, a massive star collapses into a black hole forming an inner compact source that ejects large amounts of mass within a short time interval. Successive plasma shells with typical Lorentz factors of $\Gamma = 100 - 1000$ are thus formed and relativistic internal shocks are created. When the outer shells slow down they are hit by faster inner shells and internal shock fronts are piling up. During this procedure, electrons and protons are accelerated. Electrons lose an amount of energy through synchrotron radiation while protons can be accelerated up to energies of approximately 10^{21} eV favoring the neutrino production. During the fireball expansion, the shells are driven into the interstellar medium and the external shocks are built up, leading to an afterglow emission which is visible in X-ray, optical and radio wavelengths. The neutrino emission has been predicted for three phases of the GRB evolution including the precursor phase when the jet is still forming and no electromagnetic radiation is escaping, the prompt phase coinciding with the burst in gamma rays and the afterglow phase [18].

Starburst galaxies: These galaxies have large populations of massive stars in formation and a higher density of supernovae. During the large-scale star formation, where the central regions eject a galactic-scale wind driven by the collective effect of supernova explosions and winds from massive stars the neutrino production is predicted via hadronic mechanisms. The gamma ray flux at several hundred GeV suggests cosmic ray densities of two to three orders of magnitude above that in our own Galaxy, making it a potential source of neutrinos [19], [20].

Cosmogenic neutrinos: The UHECRs combined with the diffuse photon background filling the Universe consist possible sources of ultra high energy neu-

1. COSMIC RAYS AND NEUTRINO PRODUCTION

trinos. The production of the so-called cosmogenic or GZK neutrinos is expected to be due to hadronic processes and specifically the Δ^+ resonance, which takes place when ultra high energy protons impinge the CMB background, as described in section 1.2.2. The magnitude and features of the cosmogenic neutrino flux depend on the assumptions made about the sources that produce neutrinos and in particular the composition of UHECRs at the source, the evolution of the source population with redshift and the injection spectrum. The composition of UHECRs significantly affects the neutrino flux, as heavier nuclei lose energy via photon disintegration disfavoring the neutrino production, thus reducing the expected neutrino flux [14], [21].

1.2.1.2 Galactic sources

Apart from the extragalactic neutrino sources, many objects inside the Galaxy exhibit non-thermal photon spectra, which hints at particle acceleration. If hadrons are accelerated in these objects, they could act as sources of high energy neutrinos. A number of Galactic neutrino sources is discussed below.

Supernovae Remnants and Pulsar Wind Nebulae: Supernovae can be the final stage of the evolution of stars in which the whole star explodes. The matter ejected with supersonic velocity in the supernova explosions collides with the inter-stellar matter, forming a shock wave at which particle acceleration may occur. These supernovae remnants (SNRs) are thought to be responsible for the production of CRs with energies up to about 10^{15} eV. CRs interacting with ambient matter can produce neutrinos and gamma rays via decays of charged and neutral pions. Some of the most intense SNRs have a pulsar (rapidly spinning neutron star) and are of interest because of their strong variable magnetic field which could further accelerate charged particles. Some examples of this type of SNRs observed so far, are the RXJ 1713.7-3946 and RXJ0852.0-4622, which is also known as Vela Junior [22].

Pulsar Wind Nebulae (PWNe) refer to pulsar winds consisting of relativistic electrons and positrons that emit strong synchrotron radiation and fill the SNRs. In particular, a rapidly spinning neutron star (pulsar), which is the residue of the progenitor star is formed in a sub-class of SNRs. The rotational energy is converted into the kinetic energy of the pulsar wind which terminates in a shock when it encounters the ambient medium. Acceleration of protons and nuclei could take place at shocks in the pulsar wind giving rise to the production

of the observed gamma rays and possibly neutrinos via the π^0 and π^\pm decays respectively [23].

X-ray binaries and Microquasars: X-ray binaries refer to galactic X-ray binary systems, which show morphological similarities with AGNs and are believed to follow the same mechanism, including the accretion of matter from a companion star onto a massive black hole or a neutron star. During this mechanism energy is emitted in the form of X-rays while high energy neutrinos are expected to be produced via similar mechanisms as in AGNs [24].

Microquasars are a subcategory of X-ray binaries which exhibit relativistic jets, observed in the radio band. Apart from electrons, hadrons could be accelerated in the jet. The interactions of hadrons, and specifically protons, with the synchrotron photons produced by accelerated electrons could then lead to neutrino production. A theoretical model in which protons, accelerated at energies higher than 100 TeV by internal shocks within jets, could produce TeV neutrino fluxes through the interaction of photons with mesons on ambient X-ray radiation has been proposed by Levinson and Waxman [25].

Cosmic ray neutrinos from the Galactic disc: Diffuse CRs propagating through the Galaxy will interact with the interstellar medium. These interactions are expected to produce gamma rays and neutrinos via neutral and charged pion decays. The predicted neutrino flux is thus related to the density of matter in the Galaxy [26].

1.2.2 Neutrino Production from Hadronic processes

The generation of high energy photons and neutrinos in hadronic interactions is theoretically explained by the so-called "beam dump" model which borrows its name from accelerator physics. According to this model the charged cosmic rays, the "beam", interact with the massive target, the "dump", that consists of diffuse gas or plasma. The range of the mesons produced is long enough and allows them to decay before being absorbed by the matter surrounding the source, yielding neutrinos or photons as the decay products. Neutrinos are thus generated by protons from cosmic accelerators, via charged pion production in collisions with the ambient matter or radiation fields, in interactions such as:

$$p + nucleus \rightarrow \pi^{\pm,0} + X \tag{1.7}$$

$$p + \gamma \rightarrow \Delta^+ \rightarrow \begin{cases} \pi^0 + p \\ \pi^+ + n \end{cases}$$

[27] followed by the subsequent interactions of pions:

$$\begin{aligned} \pi^0 &\rightarrow \gamma\gamma \\ \pi^+ &\rightarrow \mu^+ + \nu_\mu, \quad \pi^- \rightarrow \mu^- + \bar{\nu}_\mu \end{aligned}$$

and:

$$\mu^+ \rightarrow e^+ \bar{\nu}_\mu \nu_e, \quad \mu^- \rightarrow e^- \nu_\mu \bar{\nu}_e$$

Regarding the neutrino production chain, the three flavors of neutrinos are produced with a ratio $\nu_e : \nu_\mu : \nu_\tau = 1 : 2 : 0$ during the π meson decay. However, neutrino oscillations turn this ratio into $\nu_e : \nu_\mu : \nu_\tau = 1 : 1 : 1$ upon arrival at Earth [13].

1.3 Atmospheric Neutrinos and Muons

Atmospheric neutrinos are created in cosmic ray induced air showers in the atmosphere of the Earth. Amongst all the particles that are created in air showers, only neutrinos and muons produced during Charged Current (CC) interactions of neutrinos, can reach the underwater neutrino telescopes. The so-called atmospheric muons are absorbed by the Earth so they can only reach the detector from above the horizon. Even so, they still constitute one of the most abundant backgrounds of the detector as it is shown in Figure 1.4. In order to reduce the atmospheric muon background, the underwater neutrino telescopes are deployed in depths of several kilometers as the atmospheric muon flux is decreased significantly when the mass water equivalent increases (see Figure 1.4). In contrast to atmospheric muons, atmospheric neutrinos reach the detector from all directions but are detected less frequently due to their small interaction probabilities. Atmospheric neutrinos constitute an almost irreducible background since it is hard to distinguish them from astrophysical neutrinos.

The atmospheric neutrino flux consists of two components, the conventional flux, which dominates the lower energy part of the spectrum and the prompt flux that contributes to the flux at higher energies (see Figure 1.5 from the IceCube Collaboration). The conventional atmospheric neutrino flux refers to the decays

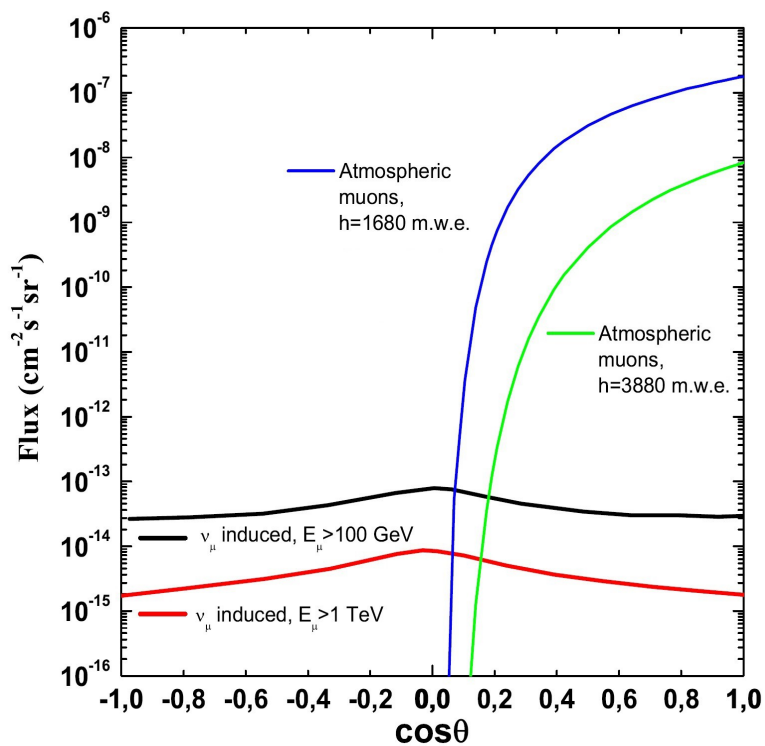


Figure 1.4: The atmospheric neutrino flux for different ranges of E_μ [28] and the atmospheric muon flux [29] for two different water depths, both as a function of the zenith angle [30].

1. COSMIC RAYS AND NEUTRINO PRODUCTION

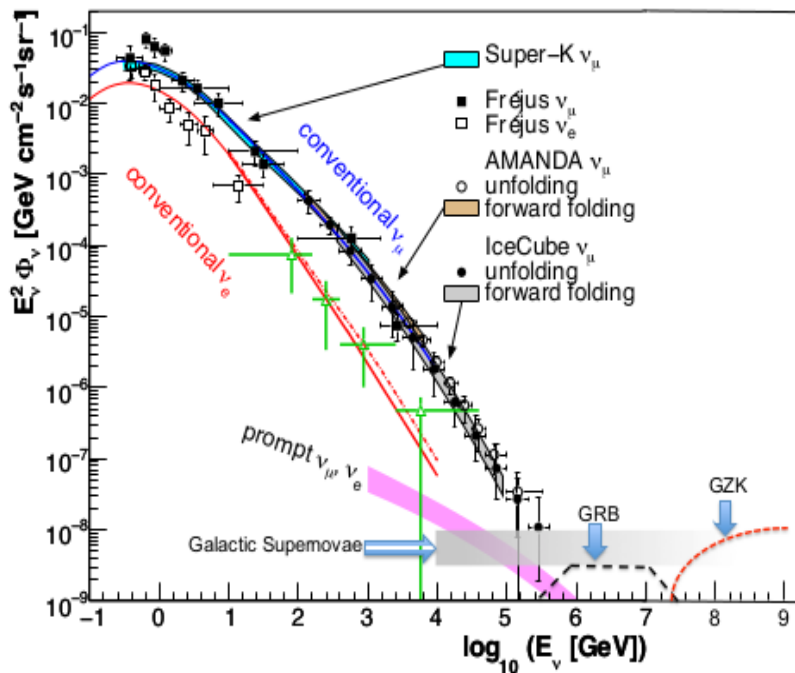


Figure 1.5: The conventional and the prompt component of the atmospheric ν_μ and ν_e flux are shown. A sample calculation of the GZK neutrino flux and the theoretically expected astrophysical neutrino fluxes produced by SNRs and GRBs are also shown [33].

of kaons and charged pions during their interactions with air molecules. The resulting neutrino flux differs from the original cosmic ray flux as the energy spectrum is steeper (reaching approximately $E^{-3.7}$) while the flux is enhanced towards the horizon [31]. The prompt atmospheric neutrino flux is due to the decays of heavy, short-lived hadrons that contain a charm or bottom quark. These hadrons decay before having the chance to interact, thus giving rise to a flux of prompt atmospheric neutrinos. This flux is expected to follow the spectrum of cosmic rays more closely, with an energy spectrum of approximately $E^{-2.7}$ and an isotropic zenith angle distribution [32].

2

Neutrino Telescopes

Neutrino detection in underwater neutrino telescopes is based on the detection of light emitted during the passage of neutrino induced particles through water. The detection principle of neutrino telescopes, the neutrino interactions with the Earth or sea water and the signature of events that are detected in neutrino telescopes are described in the following sections. The main backgrounds of underwater neutrino telescopes are discussed and a brief overview of the existing water and ice neutrino telescopes is provided.

2.1 Detection Principles

The original idea for the construction of neutrino telescopes belongs to Markov and Zheleznykh, who in 1961 [34], suggested the use of deep lakes or the sea for the detection of secondary particles (and specifically muons) created in charged current interactions of high energy (muon) neutrinos with the Earth. These secondary particles traveling with relativistic velocities through water emit photons in a characteristic angle forming a light cone, the Cherenkov cone. The photo-sensors of the neutrino telescope detect these photons in order to reconstruct the secondary particle direction and energy and thus to extract a measure of the parent neutrino direction and energy. The cross section of neutrinos with matter is very small which explains the necessity of large instrumented volumes in order to get sufficient statistics. Apart from water, ice can also be used as a target-material for neutrino detection.

The "golden channel" for neutrino astronomy with Cherenkov telescopes is the muon-neutrino charged current interaction. The detection of upward-going

2. NEUTRINO TELESCOPES

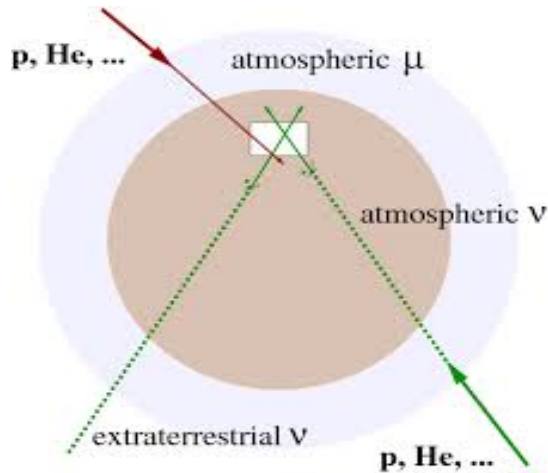


Figure 2.1: Sources of muons in deep underwater/ice detectors. Cosmic nuclei protons (p), particles (He), etc. interact in the Earth’s atmosphere. Atmospheric muons created by these interactions can reach the detector (white box) from above. Upward-going muons must have been produced in interactions of extraterrestrial neutrinos [13].

muons guarantees the neutrino origin of the muon since no other known particle can traverse the Earth. As it is shown in Figure 2.1 and is described in detail in section 1.3, there are other sources of muons that can reach the neutrino telescope and can be misidentified as muons from neutrinos of extraterrestrial origin. These sources, consist the detector background and refer to neutrinos and muons that are generated in the Earth’s atmosphere (atmospheric neutrinos and muons). Neutrino telescopes need to be situated at depth of several kilometers in order to suppress downward-going (atmospheric) muons which may be misreconstructed as upward-going, while the background from atmospheric neutrinos cannot be reduced by going deeper. Atmospheric neutrinos provide, however, a standard calibration source and a reliable proof of principle.

Underwater neutrino telescopes consist of photomultiplier tubes (PMTs) housed in transparent pressure spheres (optical modules) which are spread over a large volume in oceans, lakes or glacial ice. PMTs record the arrival time and amplitude of Cherenkov light emitted by muons or particle cascades. The light recorded by PMTs is then used for event triggering and the reconstruction of direction and energy of neutrinos.

2.1.1 Neutrino Interactions

Neutrinos are neutral subatomic particles with very low mass, that interact only through weak interactions. These elusive particles can only be detected by the light produced by the secondary particles that are created during the neutrino interactions with matter. A sketch of the Neutral Current (NC) and Charged Current (CC) neutrino interactions of different flavors is shown in Figure 2.2. The secondary particles that are created in each case and the induced electromagnetic and/or hadronic showers are shown. The differential cross sections for CC, $\nu_l N \rightarrow l X$ and NC interactions, $\nu_l N \rightarrow \nu_l X$ with $l = \mu, e, \tau$ are:

$$\frac{d^2\sigma_{\nu N}}{dxdy} = \frac{2G_F^2 m_N E_\nu}{\pi} \frac{M_W^4 x}{(Q^2 + M_W^2)^2} \times [q(x, Q^2) + (1-y)^2 \bar{q}(x, Q^2)] \quad (2.1)$$

for CC interactions and:

$$\begin{aligned} \frac{d^2\sigma_{\nu N}}{dxdy} = & \frac{G_F^2 m_N E_\nu}{2\pi} \frac{M_Z^4 x}{(Q^2 + M_Z^2)^2} \times [g_L^2 (q(x, Q^2) + (1-y)^2 \bar{q}(x, Q^2)) \\ & + g_R^2 (\bar{q}(x, Q^2) + (1-y)^2 q(x, Q^2))] \end{aligned} \quad (2.2)$$

for NC interactions. $x = Q^2/2m_N(E_\nu - E_l)$ and $y = (E_\nu - E_l)/E_\nu$ are the Bjorken variables, $Q^2 \simeq 2xyE_\nu M_N$ is the square of the four-momentum transferred between the neutrino and the lepton (in case of CC interactions) or between the neutrino and the scattered neutrino (in case of NC interactions), m_N is the nucleon mass, M_W and M_Z are the masses of the W and Z boson and G_F is the Fermi coupling constant [35]. Functions $q(x, Q^2)$ and $\bar{q}(x, Q^2)$ are the parton distribution functions for quarks and antiquarks respectively, describing the distributions of the valence and sea quark flavors of the target and $g_L^2 \simeq 0.3$ and $g_R^2 \simeq 0.03$ are the weak NC chiral couplings. They are experimentally determined (at fixed target experiments and at the HERA experiment [36]) coefficients which reflect the non-purely V-A structure of the weak NC interaction. The corresponding cross sections for $\bar{\nu}$ can be deduced by exchanging q and \bar{q} .

Integrating equations (2.1) and (2.2) over x and y yields the total cross section (σ). The cross sections for CC and NC reactions of neutrinos and antineutrinos, for neutrino energies relevant to neutrino telescopes observations ($E_\nu \geq 10$ TeV), are shown in Figure 2.3. For lower neutrino energies, $E_\nu \leq 10$ TeV, $\langle Q^2 \rangle \ll M_W^2$; in this regime the cross section is linear to E_ν in a good approximation, with a value of $\sigma \simeq 10^{-35}$ cm² at $E_\nu = 1$ TeV. For higher energies, the invariant

2. NEUTRINO TELESCOPES

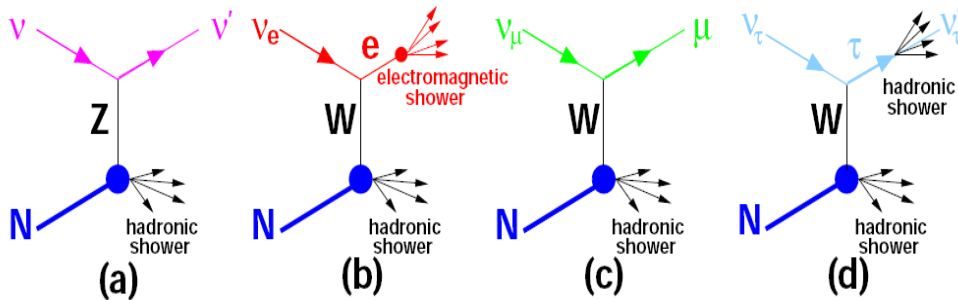


Figure 2.2: Signatures of the event topologies occurring for different types of neutrino interactions. (a) Neutral current (NC) interaction producing only a hadronic shower. (b) Charged current (CC) interaction of a ν_e , initiating an electro-magnetic and a hadronic shower. (c) CC interaction of a ν_μ producing a long range muon. (d) CC interaction of a ν_τ , producing a τ that decays after some distance.

mass $Q^2 = 2m_N E_\nu xy$ can be larger than the W-boson rest mass, resulting in a slower rise of the total cross section with energy, roughly proportional to $E_\nu^{0.4}$. As it can be observed in Figure 2.3, the cross section is different for neutrinos and antineutrinos. The cross section for antineutrinos, $\sigma_{\bar{\nu}}$, is one third of the neutrino cross section σ_ν . This can be explained by considering the contribution of valence and sea quarks to the cross section. Valence quarks dominate the cross section for neutrinos with energies less than approximately 10^6 GeV. According to detailed calculations that can be found in [37] and [38] the parton distribution function \bar{q} consisting of sea quarks can be neglected.

In this case and using the integrated equation (2.1) over x , we get the following relation for quarks and antiquarks:

$$\frac{d\sigma_{\bar{\nu}}}{dy} = (1 - y)^2 \frac{d\sigma_\nu}{dy} \quad (2.3)$$

which when integrating equation (2.3) over y results in $\sigma_{\bar{\nu}}/\sigma_\nu = 1/3$. Above neutrino energies of about 10^6 GeV, sea quarks start to dominate leading to equal cross sections for neutrinos and antineutrinos. At very high energies, no data are available to constrain the parton distributions at very small x ($x \leq 10^{-5}$) leading to uncertainties in the determination of the cross section as it is shown in Figure 2.4 [41]. The cross section at the PeV energy range can be approximated by $\sigma_\nu = \sigma_1 E/GeV$ for $E < 1$ PeV and $\sigma_\nu = \sigma_2 (E/GeV)^{0.4}$ for $E > 1$ PeV where $\sigma_1 \simeq 10^{-38}$ cm² and $\sigma_2 \simeq 4 \cdot 10^{-36}$ cm². Important uncertainties on the cross section estimate arise for neutrinos at the EeV energy range, where new physics

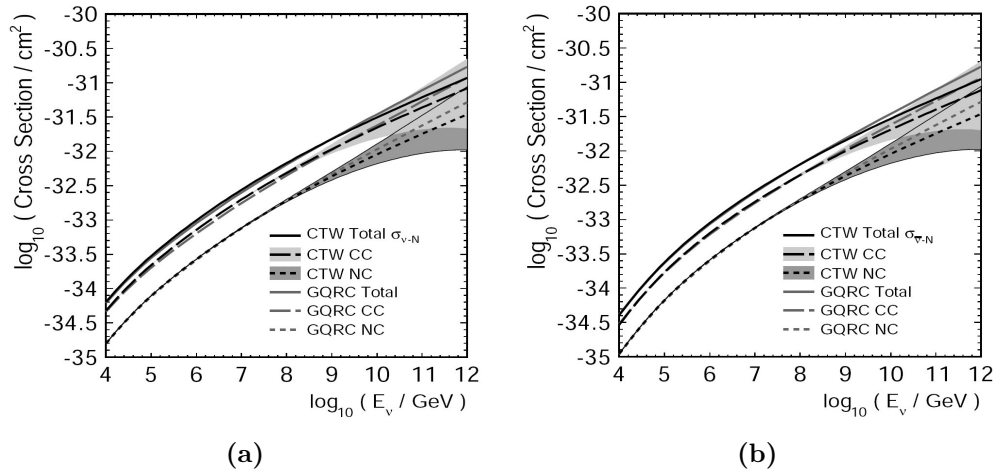


Figure 2.3: Total cross sections for neutrino (left) and antineutrino (right) scattering on isoscalar nucleons. The results of two different analyses, both for charged current (CC) and neutral current (NC) scattering with respect to the neutrino energy are shown. Results from (CTW) [39] and (GQRC) [40] are included.

phenomena can modify very significantly the interaction of neutrinos to quarks and differences in cross sections can exceed one order of magnitude [42], [43].

Based on the considerations above, the size of a detector for the search of the high energy neutrinos can be deduced. The differential neutrino flux is of the form of $dN/dEdTdS = K \cdot E^{-2}$, while integrating over time dT and the detection area dS the number of interactions expected by unit volume above a certain neutrino energy threshold E_{thr} is:

$$n_i = \int_{E_{thr}}^{\infty} K \cdot E^{-2} \cdot \sigma_{tot}(E) \cdot \rho \cdot N_A dE \quad (2.4)$$

where $\sigma_{tot}(E)$ is the total interaction cross section of neutrinos, ρ the density of the medium and N_A the Avogadro number. The characteristic size of a neutrino telescope in order to detect at least one event per year is then:

$$L = \frac{1}{(n_i \cdot 1yr)^{1/3}} \quad (2.5)$$

Considering $K \simeq 10^{-6} GeV cm^{-2} s^{-1}$ from the Waxman-Bahcall bound integrated over the whole sky, $\rho N_A = 6.023 \cdot 10^{23}$, for $E > 1$ TeV we get $L = \mathcal{O}(100)$ m. This demonstrates the necessity for very large instrumented volumes of target material for the detection of high energy neutrinos [30].

Neutrino telescopes of large instrumented volumes will not be able to distinguish between neutrinos and antineutrinos as electromagnetic or hadronic

2. NEUTRINO TELESCOPES

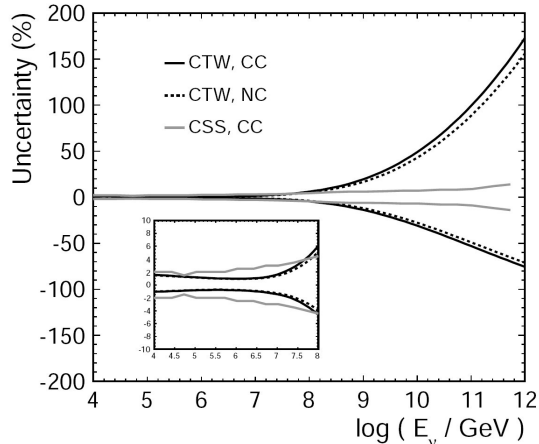


Figure 2.4: The relative uncertainties both for charged current (CC) and neutral current (NC) analyses with respect to the neutrino energy are indicated. Results from (CTW) [39] and (CSS) [44] are shown.

showers originating from both particles are identical. In addition, the final state lepton carries on average the major fraction of the neutrino energy while the hadronic cascade has lower energy. This is shown in Figure 2.5 where the average y is plotted as a function of neutrino energy for neutrino and antineutrino interactions, and $(1-y)$ corresponds to the fraction of the neutrino energy carried by the final-state lepton. For lower energies, $\langle Q^2 \rangle \ll M_W^2$ the integration of equation 2.1 over y yields $1/4 < \langle y \rangle < 1/2$, depending on the relative contribution of quarks and antiquarks. As it is shown, for larger neutrino energies, the dependence of the propagator term on $Q^2 \simeq 2xyM_N E_\nu$ reduces the mean y in the aforementioned figure [45].

Another important parameter that should be taken into account for high energy neutrino detection is the absorption of neutrinos in the Earth. For a neutrino flux of $\Phi_\nu(E_\nu, \theta) = [d^4 N_\nu / (dE_\nu dt dS d\Omega)] \cdot \Delta\Omega$ arriving within a solid angle $\Delta\Omega$ at zenith θ , the number of events recorded by a detector with area S within a time T is given by

$$\frac{N_\mu(E_\mu^{min}, \theta)}{ST} = \int_{E_\mu^{min}}^{E_\nu} dE_\nu \Phi_\nu(E_\nu, \theta) \cdot P_{\nu \rightarrow \mu}(E_\nu, E_\mu^{min}) \cdot \exp\left[-\frac{\sigma_{\nu N \rightarrow \mu X}(E_\nu) \cdot Z_\theta}{M_N}\right] \quad (2.6)$$

where Z_θ (g/cm^2) is the matter column density in the Earth crossed by the neutrino, $P_{\nu \rightarrow \mu}(E_\nu, E_\mu^{min})$ the probability to produce a muon which reaches the detector with an energy exceeding the minimum detectable energy, E_μ^{min} and M_N the nucleon mass. As it is shown in Figure 2.6, the absorption of neutrinos

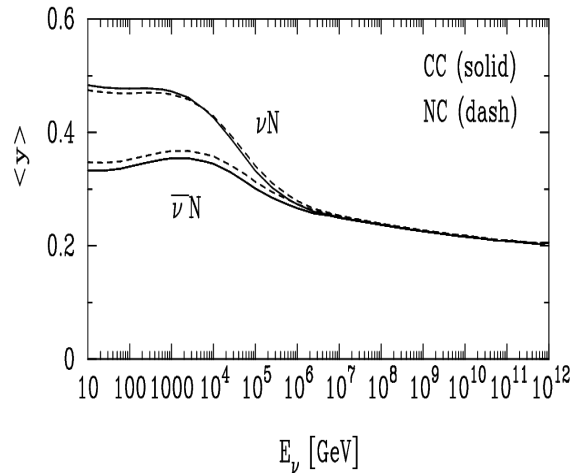


Figure 2.5: Average y as a function of neutrino energy, for CC (solid lines) and NC (dashed) reactions [45].

in the Earth is negligible for sub-TeV energies while for neutrinos at higher energies the Earth absorption becomes relevant [38].

2.1.2 Cherenkov light

When a charged particle travels in a dielectric medium faster than the phase velocity of light in that medium, the light emitted by the excited molecules along the particle track creates a characteristic cone, the Cherenkov cone (see Figure 2.7). The Cherenkov light is emitted in a characteristic angle:

$$\cos\theta_c = \frac{1}{\beta \cdot n} \quad \text{for particles with } \frac{c}{n} < v < c \quad (2.7)$$

where v is the particle velocity, c is the speed of light in vacuum, θ_c is the Cherenkov angle, $\beta = v/c$ and n is the index of refraction in the medium; n depends on the frequency of the emitted photons. The spectral distribution of Cherenkov photons per path length for a particle with charge $\pm ze$ can be calculated by:

$$\frac{dN}{dx d\lambda} = \frac{2\pi \cdot z^2 a}{\lambda^2} \cdot \left(1 - \frac{1}{\beta^2 \cdot n^2}\right) \quad (2.8)$$

where $a = 1/137$ is the fine structure constant and λ the wavelength. If the medium is water, the index of refraction is $n \simeq 1.33$ for water temperature at 20°C. The Cherenkov radiation is continuous and its density is inversely related to the wavelength squared. Therefore, the number of photons increases as the wavelength decreases, which explains why most of the Cherenkov radiation is

2. NEUTRINO TELESCOPES

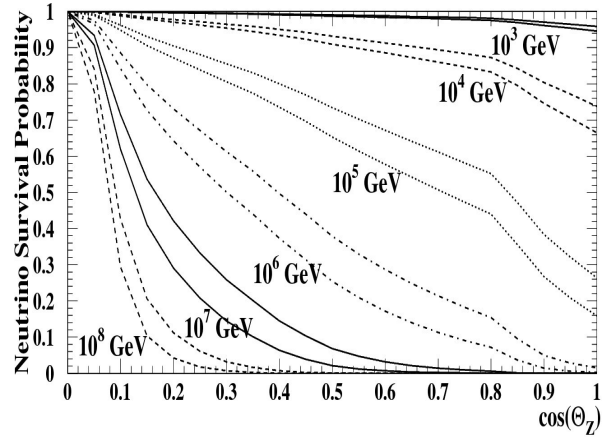


Figure 2.6: Survival probability through the Earth for neutrinos of different energies, as a function of the zenith angle. The horizon is at 0, and a path through the center of the Earth is at 1. For each energy, the upper line is for CC interactions and the lower one for CC and NC interactions [46].

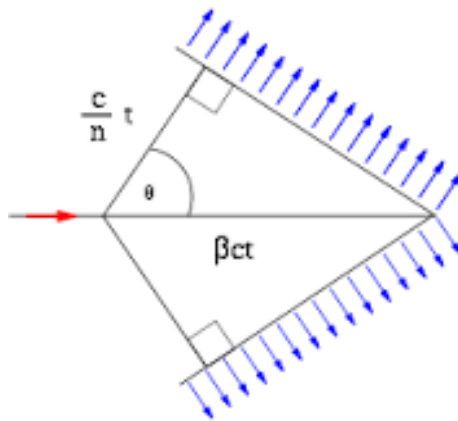


Figure 2.7: Scheme of the Cherenkov radiation, in the form of a characteristic cone, that is created when a charged particle travels in a dielectric and transparent medium faster than the phase velocity of light in that medium.

blue and mostly in UV range. Multiplying equation (2.7) with the photon energy ($E_\gamma = hf$) and integrating over the photon frequency, f , we get the total amount of energy released per particle path length:

$$-\left(\frac{dE}{dx}\right) = \frac{2\pi \cdot z^2 ah}{c} \int_{\beta \cdot n \geq 1} f \left(1 - \frac{1}{\beta^2 \cdot n^2}\right) df \quad (2.9)$$

For $\lambda = 550\text{nm}$ (blue light), equation (2.8) yields approximately 400 eV/cm, or 200 Cherenkov photons/cm. The average Cherenkov angle of these photons is $\theta_c \simeq 43^\circ$ [13], [47].

The secondary leptons that are produced during CC interactions of ν , travel through sea water emitting photons in the characteristic Cherenkov angle. In the case of muons that are able to travel long distances in sea water before losing their energy, this feature can be used to reconstruct the muon track. At high energies, the neutrino direction is almost co-linear with the muon track as it is shown by the following formula [48]:

$$\theta_{\mu\nu} \simeq \frac{0.6^\circ}{(E_\nu[\text{TeV}])^{0.5}} \quad (2.10)$$

where $\theta_{\mu\nu}$ is the mean angle between the direction of arrival of the neutrino and the muon track. Since the reconstruction of the muon direction relies on the accurate reconstruction of the Cherenkov cone, the detection units of a neutrino telescope should have a very good time resolution ($\sim ns$) and in parallel being able to detect individual photons. PMTs having these properties are used as the most appropriate detection units in neutrino telescopes.

2.1.3 Light propagation and detection

The light propagated in water experiences attenuation, which sets limits to the maximum distance between the optical sensors of the neutrino telescope. The attenuation of light is due to the absorption and scattering of light which both depend on the wavelength λ . Absorption and scattering are described by parameters usually referred to as the absorption length and scattering length, respectively. The absorption length, $L_a(\lambda)$, represents the distance after which light is absorbed. The corresponding distance for scattering is called the scattering length, $L_s(\lambda)$. Scattering delays the photons at their path from the point of emission to the optical sensors. The attenuation length $L_{att}(\lambda)$ is related to the absorption and scattering length via:

$$\frac{1}{L_{att}(\lambda)} = \frac{1}{L_a(\lambda)} + \frac{1}{L_s(\lambda)} \quad (2.11)$$

where $a(\lambda) = \frac{1}{L_a(\lambda)}$ and $b(\lambda) = \frac{1}{L_s(\lambda)}$ are the absorption and scattering coefficients respectively. These coefficients are used to describe the path, x , after which a beam of initial intensity I_0 is reduced in intensity by a factor $1/e$ according to: $I_a = I_0 \cdot e^{-\frac{x}{L_a(\lambda)}}$ or in analogy $I_s = I_0 \cdot e^{-\frac{x}{L_s(\lambda)}}$.

The values of scattering and absorption coefficients are essential for the accurate reconstruction of events in neutrino telescopes. High levels of absorption will lead to reduced collection of light while high scattering will worsen the time information. Measurements of these parameters are performed with use of lasers with wavelengths similar to Cherenkov light. The absorption length significantly changes with the wavelength compared to the scattering length which mostly varies with particulate matter. Both coefficients remain almost constant with the changes of depth corresponding to the height (of the order of 0.5 km) of a neutrino telescope. However, their values can vary with time due to seasonal changes in water parameters or due to the existence of dust or biological organisms. Hence, these coefficients need to be permanently monitored. The absorption length and the scattering length for sea water have values between 40-70 m and 200-400 m respectively for Cherenkov photons, varying with time. In contrast, these parameters are constant in time for neutrino telescopes in glacial ice (i.e. IceCube at the South Pole) but they vary significantly with depth [49].

2.1.4 Event Signatures

The topology of events in neutrino telescopes varies depending on the type of interaction and on the lepton flavor (μ, e, τ). As it has already been shown in previous section, Figure 2.2 sketches the event topologies for NC and CC neutrino interactions of different flavors. In the case of NC interactions, neutrinos interact with a nucleon producing a hadronic shower while the scattered neutrino has lower energy. The event signature in NC interactions does not depend on the neutrino flavor. However, the event topology for CC neutrino interactions differs for each flavor. CC ν_μ interactions produce a long range muon track and a hadronic and/or electromagnetic cascade whereas CC ν_e interactions produce an electron and thereby an electromagnetic cascade that overlaps with the hadronic

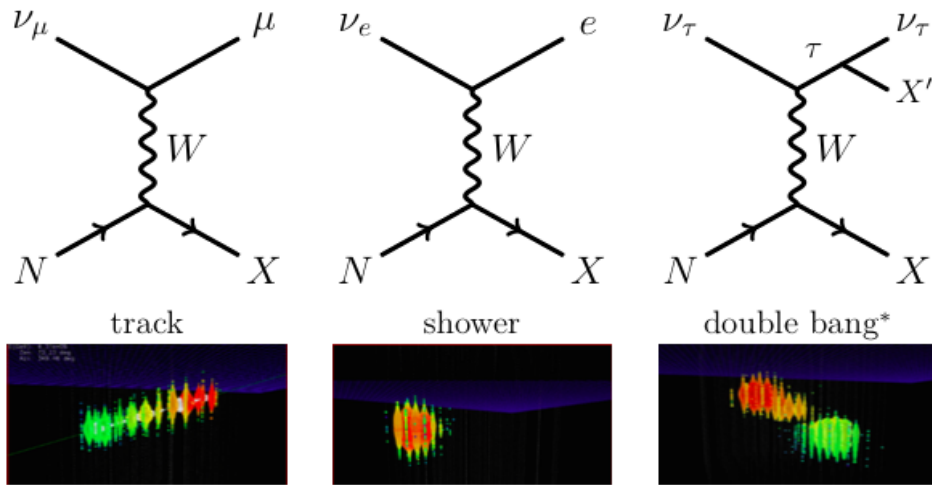


Figure 2.8: Feynman diagrams and the visualization of the event topologies at the IceCube detector for CC interaction of a ν_μ producing a long range muon, a ν_e , initiating an electro-magnetic and a hadronic shower and a ν_τ , producing a τ that decays after some distance creating the so-called double bang signature. The colour scale refers to the time evolution of light deposit (red indicates the earliest arrival time of photon and blue the latest)[51].

cascade. CC ν_τ interactions create a τ lepton followed by a hadronic shower. Depending on the τ decay mode ν_τ can either have track or cascade signatures. In most cases, tau leptons have sufficient energy to travel adequate distances in the detector such that when they decay, they produce a second visible shower. This event signature of tau neutrinos is called the "double bang" [50]. The event topologies for CC neutrino interactions in the IceCube detector are shown in Figure 2.8.

Muon Tracks: Muons travel long distances in matter, and in particular in water, before being absorbed (see Figure 2.9). This allows the detection of muons which have been created kilometers away the instrumented volume leading to a vast increase of the detector effective volume. The reconstruction of the direction and the energy of muon track is based on the reconstruction of the Cherenkov cone. As it can be deduced by equation 2.9, the reconstruction of the muon direction provides a very precise determination of the neutrino direction, which explains the great importance of the CC ν_μ channel for all investigations of astrophysical neutrino sources. However, the energy estimation of the neutrino energy for this channel, is not straightforward since a sufficient fraction of the muon track is often outside the instrumented volume, so both photons from the

hadronic shower and Cherenkov photons are lost [13], [30].

Cascades: CC interactions of ν_e , often of ν_τ and all NC interactions do not lead to high energy muons but to electromagnetic or hadronic cascades. Compared to muons, electromagnetic and hadronic showers have much shorter path lengths as it can be seen in Figure 2.9. In order to ensure the detection of photons from the hadronic/electromagnetic shower and Cherenkov photons produced by the secondary particles, which are needed to reconstruct the neutrino direction, events must be contained in the detector. This limits the effective volume to the instrumented volume of the detector. The detector is then used as a calorimeter for cascade events as most of the light produced can be detected by photomultipliers. The energy reconstruction for showers is then more accurate than that of muons (of the order of 0.05 instead of 0.3 in $\log_{10} E_\nu [GeV]$ for muon tracks). However, in the case of NC interactions, a sufficient part of the energy is taken away by the escaping neutrino and is not measured. Although, the energy for cascades can be determined with very good precision, the pointing accuracy for cascades is less accurate (of the order of 10° instead of less than 0.5° for muon tracks). This is due to the fact that showers have small path length (not exceeding 10 m) and a diameter of 10 - 20 cm, thus can be considered as quasi point-like compared to the spacing of the PMTs. In the case of ν_τ a better pointing accuracy can be achieved since the production of τ and its decay is usually accompanied by two cascades and a track. However, it is difficult to separate this type of events from simple cascades for energies below few PeV, as it can be interfered from Figure 2.9. The cascade channel is particularly interesting for searches for a diffuse, high-energy excess of extraterrestrial over atmospheric neutrinos since the background from atmospheric ν_e is significantly smaller than that of atmospheric ν_μ for the muon channel [13], [30].

2.1.5 Detector Backgrounds for Underwater Neutrino Telescopes

The backgrounds in underwater neutrino telescopes consist of the physical background of atmospheric neutrinos and muons and of environmental backgrounds. For neutrino telescopes in deep sea water, the environmental backgrounds which are of interest for this thesis, come from radioactivity and bioluminescence.

Atmospheric Neutrinos and Muons: As it has been described in detail in section 1.3, atmospheric neutrinos and muons are produced during the cosmic ray (CR) interactions with the Earth's atmosphere. During these interactions,

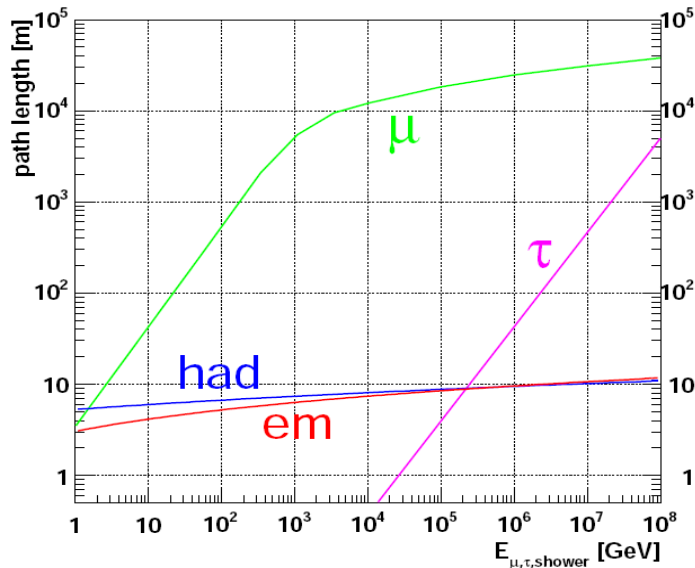
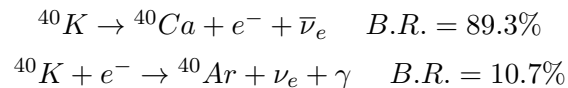


Figure 2.9: Path lengths of muons, taus, electromagnetic and hadronic showers in water as a function of their respective energy [30].

tremendous amounts of high energy muons are created in extensive air showers. The deployment of neutrino telescopes at large depths (2 km to 5 km) in water (or glacial ice) provides a primary shielding against atmospheric muons (as it is discussed in section 1.3 and shown in Figure 1.4). Since this shielding is not sufficient, neutrino telescopes mainly search for upward-going muons. Upward-going muons can only originate from neutrinos since neutrinos are the only known particles that can transverse the Earth without being absorbed. This implies that a neutrino telescope located at the Southern hemisphere will look for astrophysical neutrinos from the Northern sky and vice versa. However, the Earth becomes almost opaque to neutrinos with energies above the PeV so one has to enlarge the zenith acceptance in order to study high energy neutrinos [40]. The higher energies of muons from PeV-EeV extraterrestrial neutrinos can be used to distinguish them from downward-going atmospheric muons. Atmospheric neutrinos cannot be rejected using angular cuts and can only be distinguished from neutrinos of astrophysical origin by the reconstruction of the muon and consequently the neutrino energy, since the spectrum of astrophysical neutrinos extends to higher energies compared to atmospheric neutrinos. Although they constitute one of the main backgrounds of neutrino telescopes, atmospheric muons and neutrinos can be used to calibrate the detector as their fluxes are well known.

2. NEUTRINO TELESCOPES

Radioactivity: The decays of radioactive elements in sea water create charged particles. The propagation of these particles in sea water can produce Cherenkov light that mimics the light produced by neutrino induced particles. The most abundant radioactive element in sea water is ^{40}K which decays with two main channels yielding either electrons (β -decay) or γ rays with energies of approximately 1 MeV:



The electrons, either directly produced or from Compton scattering, often fulfill the condition for the production of Cherenkov light (as described in equation (2.6)) while can also undergo multiple Coulomb scattering in the surrounding water. The light pulses in optical sensors produced by ^{40}K decays are mostly uncorrelated, so by requiring coincidences in neighboring PMTs a significant reduction of the background can be achieved.

Bioluminescence: Bioluminescence refers to the luminescence induced by biological organisms living in deep sea. The intensity of light produced by bioluminescence and the duration of the phenomenon varies. For example, bacteria tend to emit light steadily on time scales of hours to days while larger size organisms emit light in bursts with durations of the order of seconds. The steady component of bioluminescent light gives pulses to PMTs of similar intensity as those from ^{40}K decays and is emitted typically homogeneously over the full detector. Compared to the steady component, light from bursts can give rates in PMTs larger by orders of magnitude while it is localized in a group of optical sensors.

The rates of ^{40}K and bioluminescence depend on the installation site of the neutrino telescope and in particular on the properties of sea water in this site. The most direct assessment of the environmental background is deduced by measuring the intensities of deep sea background light over long term periods. The total rate of light from the environmental background has been measured for a prototype of the KM3NeT digital optical module, housing 31 PMTs, which was integrated in the ANTARES detector at a depth of around 2375 m for in-situ testing and validation. The data taking and rate measurements over the first six months are reported in [52]. The environmental background counting

rates were characterized stable at around 8 kHz per photomultiplier (PMT) with rates averaged over 10 minutes. A maximum rate was observed as high as 1.2 MHz for the whole optical module due to bioluminescence present during the period of measurements. These rates have been observed to decrease when the bioluminescent activity decreases over the months. The genuine ^{40}K coincidence rates have also been measured and correspond to 340 Hz, 30 Hz and 2.7 Hz for two, three, four hits in coincidence within 20 ns in different PMTs of the same optical module [52]. The environmental background rates were also measured for the Capo Passero site at a depth of 3500 m. Three optical modules were deployed and data corresponding to 600 hours were analysed [53]. Similar results have been reported for the environmental background with the single rate per PMT at around 6 kHz while the bioluminescence sporadic activity was found to be homogeneous in the vicinity of the optical module [53].

2.2 The Main Existing Neutrino Telescopes

The first designs and the resolution of the technical challenges related to the deployment and commissioning of neutrino telescopes required many decades. The first neutrino telescopes were deployed at sea, lake and glacial ice. In particular, the DUMAND (Deep Underwater Muon and Neutrino Detector) project [54] was deployed off the shore of Big Island in Hawaii, the NT200 project in lake Baikal [55] and AMANDA (Antarctic Muon And Neutrino Detection Array) used the 3 km thick ice layer at the South Pole [56] as the target and detection volume. After the first deployment of the DUMAND project, European groups started to look forward to the deployment of neutrino telescopes in the Mediterranean Sea. In this context, the NESTOR [57] and NEMO [58] groups deployed prototype detector installations off the coast of Pylos in Greece and off the coast of Capo Passero in Italy respectively. Specifically, the NESTOR Collaboration reconstructed for the first time, the direction of atmospheric muons with mean zenith angle accuracy less than 10° , thus providing the proof of feasibility for such techniques in neutrino telescopes [59], [60]. In parallel, the NESTOR team performed several measurements of the light transmission in deep sea water estimating the impacts of the water depth, the different sites in the Ionian Sea and the temporal effects on these measurements [61]. ANTARES (Astronomy with a Neutrino Telescope and Abyss environmental RE-Search) [62] is the first

2. NEUTRINO TELESCOPES

underwater neutrino telescope in the Mediterranean, installed and operated off the coast of Toulon in France. The main existing neutrino telescopes described in this section, are the ANTARES and the IceCube detector [63], successor of AMANDA, which is deployed in the glacial ice of the South Pole.

2.2.1 ANTARES

The ANTARES neutrino telescope consists of 12 strings (lines), each carrying 25 storeys at a distance of 14.5 m equipped with three optical modules looking at 45° downward, an electronics container and calibration devices where necessary. A sketch of the ANTARES detector is shown in Figure 2.10. The deployment of the full detector was completed in 2008 with a total of 885 optical modules. The optical module consists of a 10-inch photomultiplier with its electronics, housed in a pressure resistant glass sphere. A special gel for optical coupling and a μ -metal cage for magnetic shielding are contained in each sphere as well. Each string has a length of 450 m and is anchored to the sea floor with a dead weight while it is kept upright by a buoy located at its top. The lower 100 m of the string are not instrumented. The distance between strings ranges from 60 to 75 m, reaching an instrumented volume of approximately 0.025 km^3 . Strings are connected to a central junction box, which is connected to shore via an electro-optical cable. The detector is deployed at a depth of 2475 m. Apart from optical modules, the ANTARES detector is equipped with an acoustic detection system, named AMADEUS [64], for feasibility studies towards acoustic neutrino detection.

Downgoing muons collected by the ANTARES telescope were used to calibrate the detector and to measure the vertical muon intensity as a function of the water depth [65]. The atmospheric neutrino spectrum has been reproduced for the conventional flux and data are in good agreement with measurements reported by IceCube [66]. Studies for neutrinos from point-sources have been performed leading to the set of 90% confidence level upper limits on the muon neutrino flux normalization between 3.5 and $5.1 \cdot 10^{-8} \text{ GeV cm}^{-2} \text{ s}^{-1}$ depending on the location of the source [67]. Combined searches for neutrinos from point-sources with ANTARES and IceCube have also been performed and results are reported in [68].

The ANTARES detector is the progenitor of the KM3NeT neutrino telescope with an instrumented volume of few km^3 that will be deployed in the

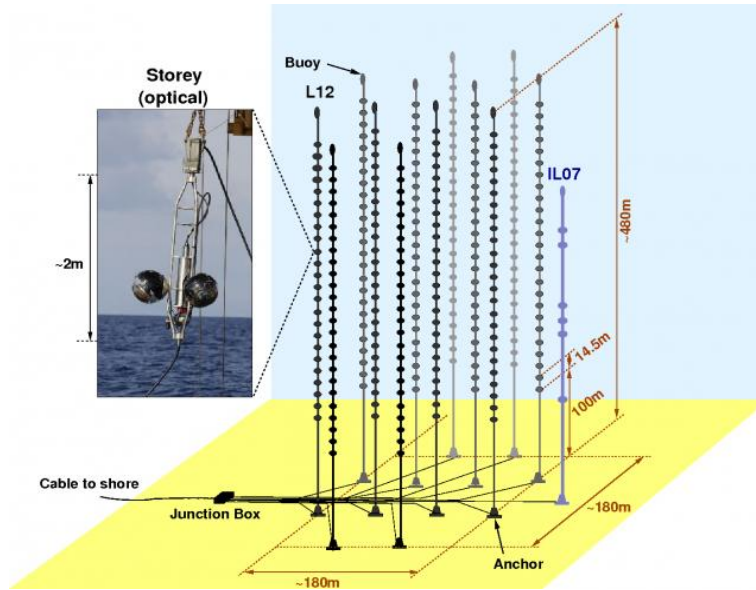


Figure 2.10: Schematic of the ANTARES detector. Indicated are the 12 strings and the instrumentation line (IL07). Shown as an inset is the photograph of a storey carrying 3 photomultipliers.

Mediterranean Sea. The KM3NeT project is described in detail in the following chapter.

2.2.2 IceCube

IceCube [32] is a neutrino telescope of about 1 km^3 located at the glacial ice of South Pole searching for high energy neutrinos of extraterrestrial origin. The detector consists of 5160 optical modules at depths between 1450 and 2450 m in the Antarctic ice (see Figure 2.11). Each optical module is a glass sphere that contains a 10-inch photomultiplier with its digital electronics. The detector consists of 86 strings with optical modules at a vertical spacing of about 17 m, while the horizontal spacing between two strings is approximately 125 m. Eight of these strings are more densely located consisting a five times more dense instrumented volume than the standard IceCube array, in the center of the detector, named the Deep Core. The Deep Core is situated primarily at 2100 m below the surface of the ice thus taking advantage of the exceptionally clear ice at those depths. It is used as the low energy extension of the IceCube detector as it can detect neutrinos with energies as low as about 10 GeV. Furthermore, it can use the surrounding IceCube detector as a highly efficient active veto

2. NEUTRINO TELESCOPES

against the background of downward-going muons increasing its sensitivity to low energy neutrino detection [69]. Apart from Deep Core, the IceCube detector also includes a cosmic ray detector called IceTop. IceTop consists of 81 stations installed on the surface, above the IceCube detector, forming an air shower array. Each station consists of a pair of cylindrical plastic tanks filled with clear ice, that contain the optical modules. This detector focuses on the detection of electrons and muons from cosmic ray induced air showers while its scientific goal is to reconstruct the energy, type, and direction of the cosmic ray primary particle [70], [71]. The IceTop detector can also be used as a veto for the cosmic ray induced background in IceCube in order to measure astrophysical neutrinos from the Southern sky [72].

The IceCube detector has provided evidence for extraterrestrial flux of high energy neutrinos in multiple searches [73], [74]. Figure 2.12 shows the arrival angles and the energy deposited in the instrumented volume for 37 neutrino candidate events. The deposited energies of these events range from 30 TeV to 2 PeV and were observed in 988 days of data [74]. The single-flavor energy spectrum for the IceCube astrophysical neutrino flux with cutoff at 3 PeV has been parametrized as: $\Phi(E_\nu) = 1.2 \cdot 10^{-8} \cdot \frac{E_\nu^{-2}}{1 \text{ GeV}} \cdot e^{-E_\nu/3 \text{ PeV}}$ [$\text{GeV}^{-1} \text{ sr}^{-1} \text{ s}^{-1} \text{ cm}^{-2}$] where E_ν is the neutrino energy. This is the best limit ever established on the flux of astrophysical neutrinos while further observations with the upgraded IceCube detector [33] or the planned KM3NeT telescope are essential to answer questions about the sources of this astrophysical flux. Recently, a high energy muon event with deposited energy of about 2.6 PeV (± 0.3 PeV) was detected to cross the instrumented volume. This deposited energy is expected from a muon with energy between 4 and 5 PeV, consisting the highest energy event observed so far [75].

Apart from neutrino astronomy, the IceTop detector has been used to measure the cosmic ray anisotropy for the first time in the Southern Hemisphere [76]. In addition, a measurement of the atmospheric oscillation parameters has been achieved with the Deep Core detector, with a precision comparable to that of dedicated oscillation experiments, such as MINOS, T2K, or Super-Kamiokande [77].

Studies for the extension of the IceCube detector have been performed. The next generation of IceCube, the IceCube-Gen2 [33] detector with an 10 km^3

2.2 The Main Existing Neutrino Telescopes

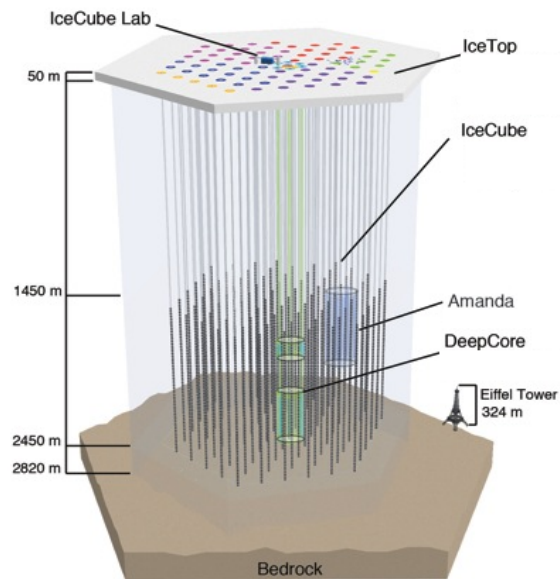


Figure 2.11: Schematic view of the IceCube neutrino telescope. At the surface, the air shower array IceTop and the IceCube counting house are indicated. The location of the AMANDA detector, a progenitor of IceCube and the Deep Core are shown as well. The Eiffel tower is shown to scale for a size comparison.

instrumented volume of clear glacial ice at the South Pole will be able to collect high statistics of very high energy neutrinos (at the PeV range). Besides the extension to the high energy range, the IceCube Collaboration is looking forward to the construction of the PINGU sub-array [78] that targets precision measurements of the atmospheric oscillation parameters and the determination of the neutrino mass hierarchy.

2. NEUTRINO TELESCOPES

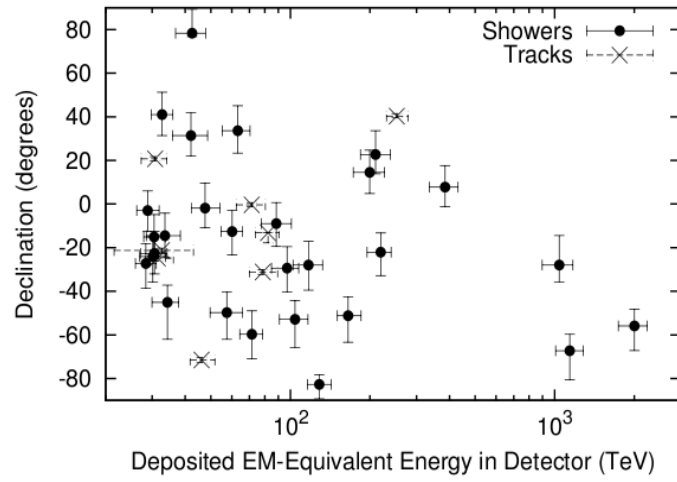


Figure 2.12: Arrival angles and deposited energies of the detected events in three years of IceCube data [74].

3

The KM3NeT Project - ARCA Detector

KM3NeT is a network of underwater neutrino telescopes that will be deployed at the Mediterranean Sea. The KM3NeT project consists of two different detector configurations, the ARCA and the ORCA detector. The ARCA detector is a neutrino telescope of several cubic kilometers that aims to search for high energy neutrinos (at the TeV region) of extraterrestrial origin. The ORCA detector covers a volume of few cubic meters and intends to measure the neutrino mass hierarchy using oscillations of atmospheric neutrinos (in the GeV range) through the Earth. The KM3NeT project and in particular the ARCA detector is described in this chapter. In the first sections of the chapter the detector configuration, the installation sites, the detection units and their components are discussed. In section 3.2, the generation and simulation packages employed for the production and simulation of the events used to study the expected performance of the detector to neutrinos are described.

3.1 Detector Design

The first phase of the ARCA detector consists of two building blocks covering a total volume of approximately 1 km^3 (Figure 3.1) that are going to be installed at the Capo Passero site, located at the east of the Sicilian coast, and at a depth of approximately 3500 m. Each building block is a roughly cylindrical detector configuration consisting of 115 detection units (DUs), usually referred to as strings [79]. In the final stage, the ARCA detector will consist of six

3. THE KM3NET PROJECT - ARCA DETECTOR

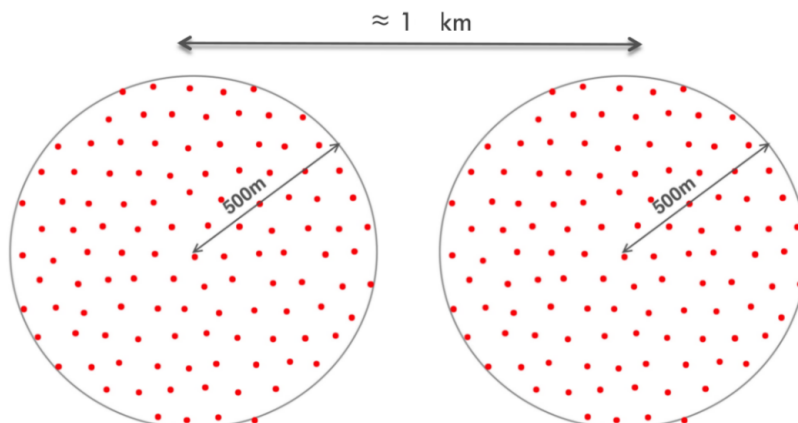


Figure 3.1: The ARCA detector layout.

building blocks resulting to an instrumented volume of several cubic kilometers (depending on the distance between the detection units). There are two more sites proposed for the installation of the rest four building blocks: the Toulon site located in the Ligurian Sea at a depth of 2475 m and the Pylos site in the East Ionian Sea at three possible depths of 5200 m, 4500 m and 3750 m resulting to a multi-site infrastructure [79], [80]. This multi-site infrastructure is shown in Figure 3.2. Apart from the network of neutrino telescopes, the KM3NeT consists of administrative head quarters located in the Netherlands and data repository and data processing centres in France and Italy, as it is shown in Figure 3.3.

The physical, geophysical and oceanographic properties of these sites have been investigated in detail and satisfy the requirements to host the KM3NeT infrastructure. In particular, these sites have good optical water properties ¹, low level of bioluminescence and bacterial deposition on optical surfaces, low sea current velocities, low rate of sedimentation and low risk of significant seismic events [80]. The sites are also sufficiently close to shore facilitating the deployment and reducing the expense for power and signal cable connections to shore. In parallel, these sites provide sufficient depths to reduce background from atmospheric muons (as it is shown in Figure 1.4). Long term characterisation studies for these sites have been performed, including measurements on the deep-sea water optical properties (absorption and scattering), water environmental prop-

¹The absorption and scattering lengths for these sites are close to the ones of optically pure sea water for light in the wavelength range of about 350 nm to 550 nm, which is the wavelength for Cherenkov photons.

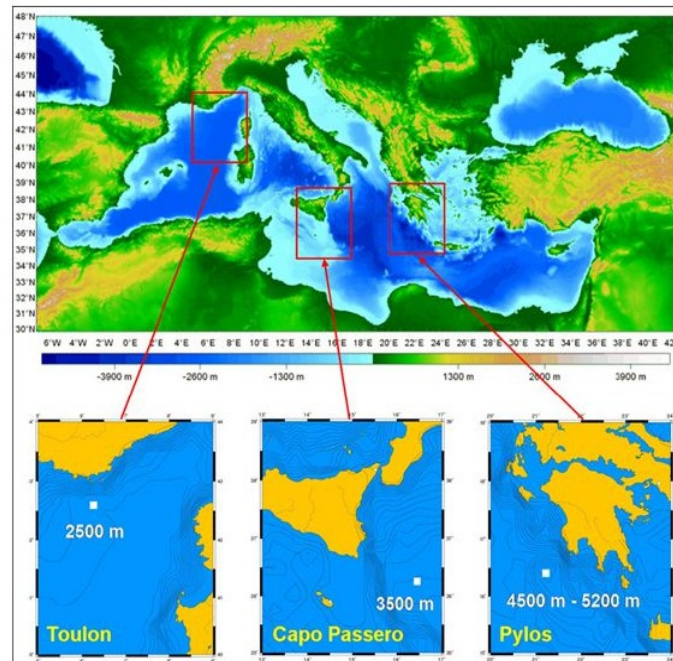


Figure 3.2: The installation sites for the KM3NeT project in the Mediterranean Sea with the corresponding depth for each site.



Figure 3.3: The KM3NeT research infrastructure consisting of three installation sites. The data center and administrative head quarters are also shown.

3. THE KM3NET PROJECT - ARCA DETECTOR

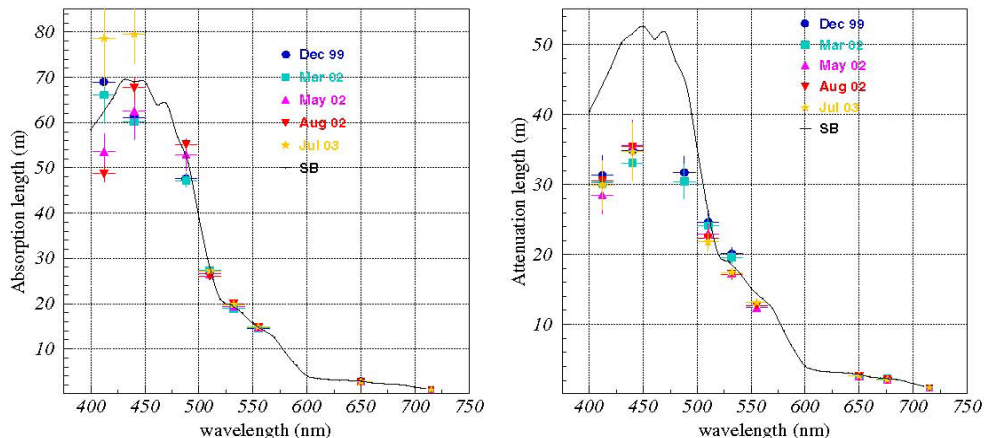


Figure 3.4: The absorption length (left panel) and attenuation length (right panel) measured at the Capo Passero site at four seasons. Also indicated are the values for optically clean salt water (black lines) [81].

erties (temperature, salinity) and biological activity. These measurements are described in detail in [80].

Specifically for the Pylos site, the transmission length of light was measured with a device, developed by the NESTOR group (Long-Arm Marine Spectrophotometer, LAMS). This is a rigid structure that allows for measuring the intensity of light from an isotropic, constant source at several distances [82]. The transmission length, L_β , of light in water characterises the variation of light intensity as a function of the distance between the source and the detector ¹. The light transmission length in Pylos site is 55 ± 10 m at a wavelength of 460 nm corresponding to 10% longer length than the one measured in the Capo Passero. The measurements on the absorption and attenuation length measured in Capo Passero are also presented in Figure 3.4. As it can be observed, at all wavelengths, deep waters have an absorption length compatible with that of pure sea water. In addition, there is not significant seasonal dependence of the optical parameters for all three sites.

Depending on the installation site, the building blocks of the KM3NeT will be situated at a latitude λ between 36° and 43° North, allowing the detection of upgoing neutrinos from the Southern hemisphere. Compared to the IceCube

¹In analogy to the absorption coefficient, the transmission coefficient, $\frac{1}{L_\beta}$, describes the path x after which a beam of initial intensity I_0 is reduced by a factor of $1/e$.

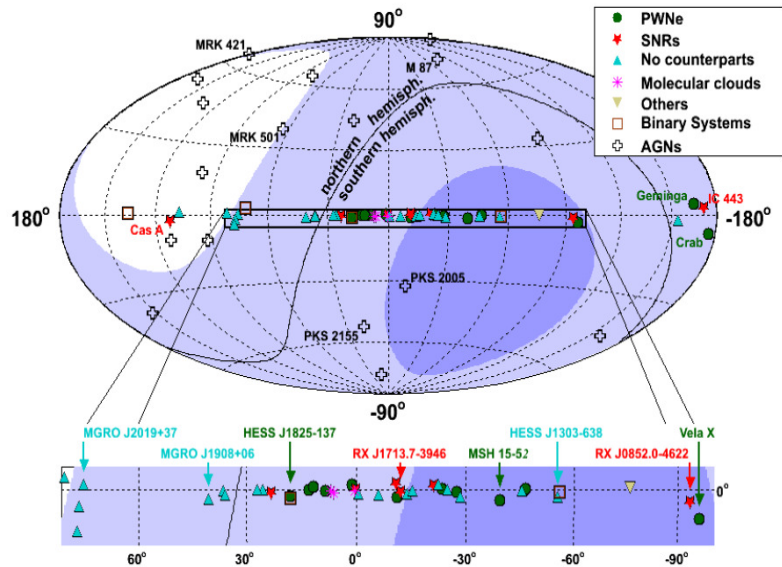


Figure 3.5: Sky coverage in Galactic coordinates for a detector located in the Mediterranean Sea and at the South Pole. The shading indicates the visibility for a detector in the Mediterranean with 2π downward coverage; dark (light) areas are visible at least 75% (25%) of the time. The locations of recently observed sources of high energy gamma-rays are also indicated.

detector, the KM3NeT project located in the Mediterranean Sea, will have a larger sky coverage. As it is shown in Figure 3.5, the KM3NeT will be able to observe up-going neutrinos from a large fraction of the sky including the Galactic Centre and most of the Galactic Plane. This is a major advantage of this neutrino telescope since many sources of interest for neutrino astronomy are located in the Galactic plane. In this way, the KM3NeT neutrino telescope will complement the field of view of IceCube. KM3NeT and IceCube neutrino telescopes will thus cover the whole sky.

In addition to its geographical location the KM3NeT neutrino telescope has significant advantages over ice experiments due to the very good optical properties of sea water ¹, as it was mentioned above. The advantages of seawater neutrino telescopes lead to significantly better angular resolution, down to 0.1° (RMS) for muon tracks, compared to approximately 1° for IceCube and a better and more uniform discovery potential flux due to the homogeneity of the

¹The scattering length in ice is much shorter than the scattering length in sea water, with values between 20-40 m varying with depth.

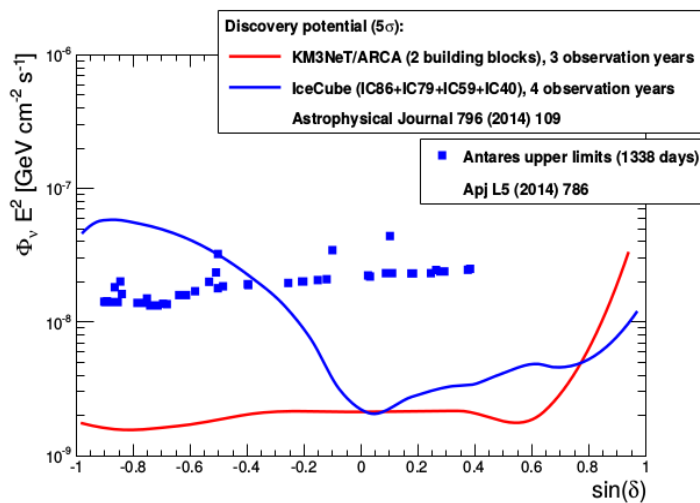


Figure 3.6: KM3NeT/ARCA 5σ discovery potential (red line) per flavor for (point-like) neutrino sources with a spectrum $\propto E^{-2}$ for 3 years of data-taking (in order to have a comparable exposure with respect to the current IceCube result) as a function of the source declination. For comparison, shown also is the corresponding discovery potential for the IceCube detector (blue line), and upper limits on particular sources for the ANTARES detector (blue squares) [83].

medium. An example of this uniformity can be seen in Figure 3.6 in which the discovery potential¹ of the KM3NeT (red line) for neutrino sources is mentioned and compared with the corresponding discovery potential for the IceCube detector (blue line). For comparison, the upper limits on particular sources for the ANTARES detector are presented. A disadvantage of sea-water neutrino telescopes is the higher optical background due to radioactive decay of ^{40}K and bioluminescence. However, these backgrounds can be reduced by requiring hits in time coincidence in neighboring PMTs of the same OM, as discussed in the following section.

3.1.1 Detection Units

The KM3NeT detection unit hosts 18 digital optical modules (OMs) vertically aligned on a string with 36 m distance between each other, leading to a string height of almost 600 m, while the distance of the first OM from the seafloor is 100

¹The discovery potential is determined by the number of observed events in a given observation time that have a probability less than 5σ to purely originate from background. The discovery potential is discussed in detail in section 6.2.

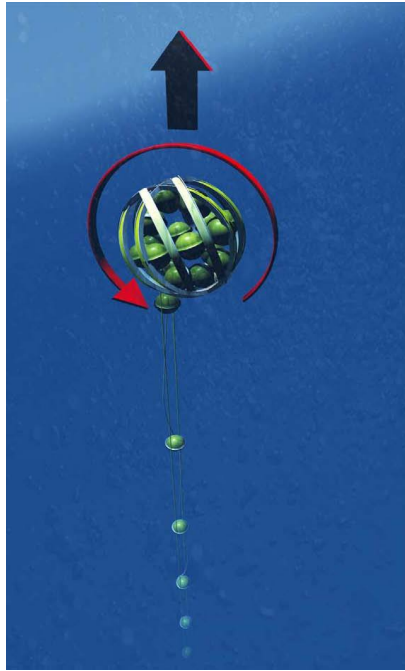


Figure 3.7: A sketch of the KM3NeT string unfurling in the sea.

m. These strings are anchored to the sea floor and kept close to vertical with the aid of submerged buoys at the top of the string. Two dyneema ropes keep the OMs together at the string, an electro-optical backbone provides connections for each OM on two conductors for power and two optical fibers are used for communication with shore. In order to deploy these strings to sea depth, a launcher vehicle is used. The strings are wrapped in the launcher vehicle, which is then lowered to the seabed from a surface vessel. Once the launcher vehicle reaches the seabed the buoy is released (via an acoustic release) and the string rises to its full height as it is shown in Figure 3.7. Finally, a Remotely Operated Vehicle (ROV) is used to connect the string with the under-sea infrastructure and the launcher vehicle is recovered for subsequent deployments.

3.1.2 Optical Modules

Each OM is a pressure-resistant glass sphere with a diameter of 17 inches (432 mm) that is equipped with 31 photomultipliers (PMTs) with 3-inch (72 mm) photocathode area and their readout electronics (Figure 3.8) [52], [53]. Each PMT is surrounded by a cone-shaped reflector that increases the photocathode diameter to 95 mm, collecting photons that would not be otherwise detected [84].

3. THE KM3NET PROJECT - ARCA DETECTOR



Figure 3.8: Left: The KM3NeT digital optical module. Right: The assembly of the prototype.

The PMTs are arranged in 5 rings with zenith angles of 56° , 72° , 107° , 123° and 148° respectively (Figure 3.9). The 6 PMTs in each ring are spaced at 60° in azimuth and the successive rings are staggered by 30° . The last PMT points vertically downward at a zenith angle of 180° [52]. This OM designed for the KM3NeT project, has several advantages compared to the traditional design of a single PMT with large photocathode area that is housed to an optical module [85], [86], [87]. In particular, each KM3NeT optical module houses three times the effective area of the single PMT in a single glass sphere while it provides an almost uniform angular coverage. The segmentation of the detection area at this multi-PMT OM makes it possible to distinguish single-photon from multi-photon hits, leading to a rejection of the environmental optical background. It also increases the reliability of the OM, as the failure of one PMT will not affect significantly the performance of the total OM. The quantum efficiency of these small PMTs ranges from 20% (at 470 nm) to 28% (at 404 nm). In addition, these PMTs provide small transit time spread ¹. The Earth's magnetic field influences electron trajectories between the photocathode and the first dynode. However, this effect is negligible for these PMTs due to their small size, and thus a mu-metal shielding from the Earth's magnetic field is not required. An additional advantage of these small PMTs is the low anode current that results to slower ageing of these photomultipliers [84]. Specifically, each PMT electronic

¹The transit time is the time interval between the arrival of a light pulse at the photocathode and the appearance of the output pulse. When a photocathode is fully illuminated with single photons, the transit time of each photoelectron pulse has a fluctuation. This fluctuation is called transit time spread (TTS).

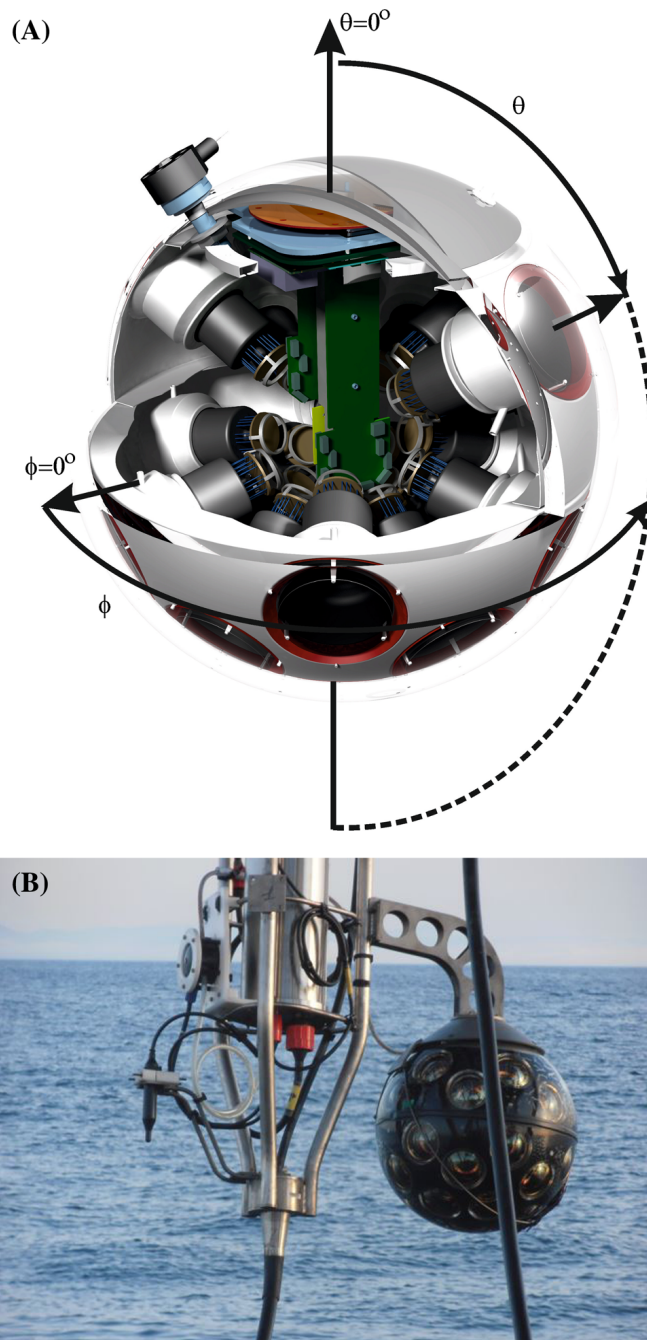


Figure 3.9: (A) The 3D cutout illustration of the OM. The zenith angle θ and the azimuth angle ϕ are indicated. $\phi = 0^\circ$ points to the support cable while $\theta = 0^\circ$ points vertically upward. (B) A picture of the prototype OM connected to the ANTARES line during deployment. The structure to which the DOM is connected is a standard ANTARES support frame including a cylindrical electronics container [52].

3. THE KM3NET PROJECT - ARCA DETECTOR

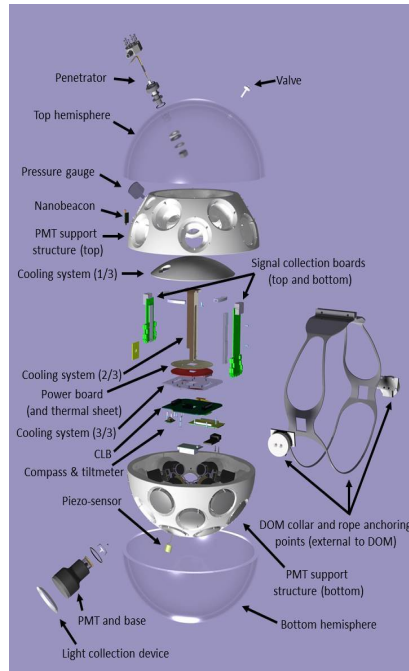


Figure 3.10: The internal structure of the optical module in KM3NeT project.

base which provides the high voltage for the PMT has been designed under a very low power requirement thus adjusting the high voltage in the range 900-1300 V. In addition to high voltage each PMT base is also responsible for the digitisation of the analogue output signal of the PMT. The output signal is converted from a charge signal to a voltage signal, followed by a conversion to a digital level by a comparator, resulting in a time over threshold (TOT) signal. The TOT signal is finally transferred to the OM central logic board (CLB) which collects the data [83].

The data collected in PMTs are transferred to the shore station via a network of electro-optical cables and junction boxes. This network also provides power flow in each detection unit and slow-control communication with the detector [80]. A position calibration system consisting of a compass-tiltmeter, an acoustic piezo sensor and a nanobeacon has been developed and located in each OM, leading to an accuracy of about 10 cm in the PMT positions. This accuracy in PMT position and direction in combination with the good timing determination of the hits in PMTs, with an RMS less than 2 ns, are necessary for an accurate muon reconstruction. The time calibration of the PMTs will be performed onshore and then the time in PMTs will be continuously monitored in situ us-

ing laser beacons located on the sea floor and LED pulsers mounted inside the OMs. All the OMs will be synchronized to sub-nanosecond level using a clock signal broadcast from shore before deployment. In addition to the aforementioned devices, the OMs include electronics for data digitization and sensors for temperature and humidity measurements while the heat from the electronics is efficiently removed and transferred to the sea via the glass sphere with the aid of a mushroom shaped aluminum structure [79], [80]. A sketch of the internal structure of the OM in KM3NeT project with its main components is presented in Figure 3.10.

3.1.3 Deep Sea Tests of Prototype Optical Module and Detection Unit of the KM3NeT detector

A first prototype OM of the KM3NeT neutrino telescope was developed and integrated in the ANTARES detector in July 2013, at a depth of 2375 m, for in-situ testing and validation (Figure 3.9). The aggregate hit rates of all PMTs in the OM were measured for a period of six months and are shown in Figure 3.11(left plot). As it can be seen in this figure, some timeframe bins show significant increases in the count rate which can be attributed to bioluminescence. As it has been already discussed in section 2.1.5, the average rate per PMT is approximately 8 kHz and is stable. Since the OM consists of multiple PMTs, a search for coincidences in the same OM can be conducted. A coincidence of hits in two (three) PMTs within a time window of 20 ns (referred to as two- and three-fold coincidences respectively) is introduced and the corresponding aggregate rates are shown in Figure 3.11 (left plot). The PMT multiplicity of the OM and its ability for single-photon counting enables the muon detection even with a single OM. This can be seen in Figure 3.11 (right plot) which shows the event rate as a function of the coincidence level. The coincidence level corresponds to the number of PMTs having a detected hit within a 20 ns time window. As it is observed, the measured event rate is in good agreement with the event rate given by the simulation of the ^{40}K decays for a coincidence level up to six. A mismatch between the data and the simulation for one coincidence level is mainly due to the contribution from bioluminescence that is not simulated and due to fact that single rates (rate of single hits in PMTs) are more sensitive to differences between the attenuation length in water and the one used for the simulation. At higher coincidence levels, the rate from simulated atmospheric

3. THE KM3NET PROJECT - ARCA DETECTOR

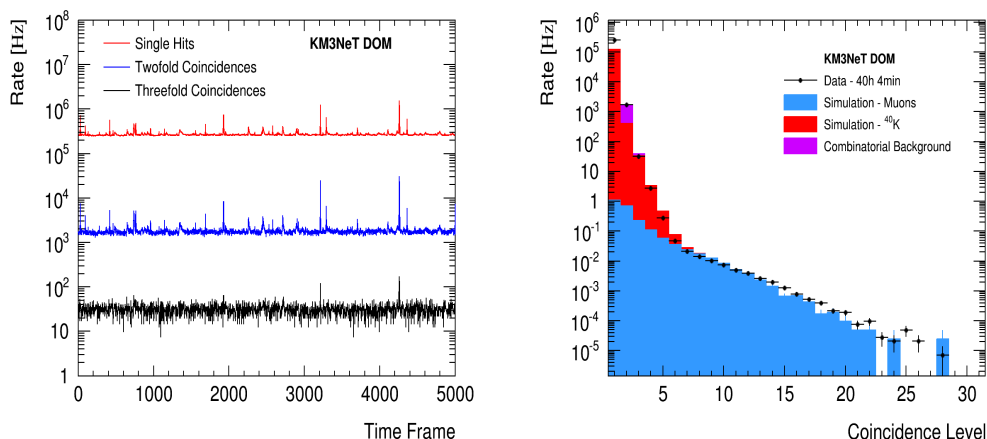


Figure 3.11: Left: Aggregate hit rates as a function of the time measured in 134 ms timeframe bins. The top trace is for single hits, while the lower traces are for two- and threefold coincidences within a 20 ns window. Right: The rate of events as a function of the coincidence level (number of PMTs with signal in a 20 ns time window). Black dots correspond to data while coloured histograms represent simulations (muons in blue, ⁴⁰K in red and accidental coincidences in purple) [52].

muons is in good agreement with the data. Therefore, atmospheric muons can be unambiguously detected with a single OM by requiring coincidences at eight PMTs [52].

In May 2014, a prototype string with three OMs at a vertical distance of 36 m was deployed at the Capo Passero site, at a depth of 3500 m. The PMTs operated at a gain of $3 \cdot 10^6$ with an intrinsic dark count rate in the range 600-1500 Hz, as measured in the laboratory, at room temperature, with a threshold of 0.3 photoelectrons. A time calibration at a nanosecond level was performed and the time offsets between the PMTs in the same OM (Intra-OM) and between all three OMs (Inter-OM) were determined. The Intra-OM time offsets primarily depend on the PMT transit time spread (up to 5 ns at FWHM) while the Inter-OM ones depend on the cable length (~ 100 km). The measured coincidences of light from ⁴⁰K background were used for the Intra-OM calibration and the LED nanobeacons (with wavelength at 470 nm) mounted inside each OM, were used for the Inter-OM calibration. Both procedures are described in detail in [53]. The data collected after 600 hours of operation were in good agreement with Monte Carlo simulations of the expected optical background and the signal from atmospheric muons (Figure 3.12 (right plot)). In this figure the rates as a function of the coincidence level (number of PMTs with hit within 25 ns) in the

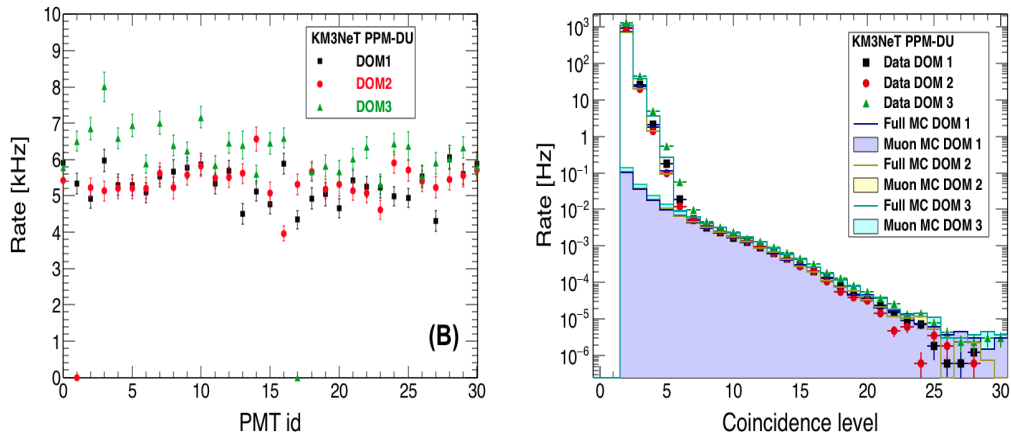


Figure 3.12: Left: Mean value of the singles rates per PMT for the 3 DOMs. The errors correspond to the standard deviation of the Gaussian of single rates for each PMT. Right: Rates of multi-fold coincidences in a time window of 25 ns for the 3 DOMs, compared to the expected Monte Carlo (MC) rates for ^{40}K background and atmospheric muons. Symbols refer to data, histograms to Monte Carlo simulations [53].

single OMs¹ are shown and compared to the rates predicted by the (full) Monte Carlo simulation of atmospheric muons (and ^{40}K background). As it can be seen, signals from ^{40}K dominate the rates for low level coincidences while at least seven coincidences are required to ensure the detection of atmospheric muons with one single OM. The mean values (of about 5.9 kHz) of the single rates mainly due to ^{40}K background for all 31 PMTs of the three OMs are also shown in Figure 3.12 (left plot). The data collected from the three OMs passed through algorithms for hit selection according to the correlations of hits in time. In this way, an almost background free final sample of muons was selected. Finally, the zenith angle of the selected muons was reconstructed with an angular accuracy of about 3° using only these three OMs.

3.1.4 Data Acquisition and Event Trigger

The readout of the KM3NeT detector is based on "all-data-to-shore" approach [88]. According to this approach all data that pass a first filtering are sent to shore via the optical fibre network. In particular, each PMT records the start time and the time over threshold (ToT) of the pulse, where the start time is the

¹The OM1, or equivalently DOM1 (Digital Optical Module), is the lowest OM to the sea depth, and DOM3 is the highest.

time at which the pulse passes beyond the threshold of 0.3 photoelectrons (level-zero filter (L0)) and ToT is the time the pulse remains above this threshold. The signals from PMTs pass to the readout electronics board (Central Logic Board [89]) of the OM. Signals are then digitised and transferred to shore. Each OM has an Internet Protocol (IP) node in an Ethernet network which allows for real time processing of the data.

Once data have been transferred to shore, online trigger algorithms are applied to filter the data and discriminate PMT pulses from physics events from pulses due to environmental background. Trigger algorithms, described in section 3.2.5.2, are searching for correlations between time and positions of PMTs with recorded pulses according to the muon or shower detection.

In addition to data from physics events, data containing the single rates of all PMTs are recorded and stored on disk. These data, referred to as summary data, are used in the simulations and the reconstruction algorithms to take into account the actual status and optical background conditions of the detector. Data from the acoustics positioning system are also transferred to shore and stored for further processing [52], [53].

3.2 Generation and Simulation Packages

Monte Carlo simulation tools are extensively used in experimental physics in order to study the parameters that affect the experimental setup and perform the optimisation studies necessary for the final detector design. In KM3NeT, the Monte Carlo generation and simulation algorithms have been used to test and optimize the design of the neutrino telescope before the construction of the detection units and their deployment to the deep sea, making in parallel estimations of the scientific results that can be achieved with the corresponding detector configuration.

The chain of software tools that are used in KM3NeT are shown schematically in Figure 3.13 and consist of event generators for neutrinos and atmospheric muons, algorithms for the simulation of particles, light and electronics, codes for event triggering and packages for the event reconstruction. The water depth, the water optical properties and background light contribution as measured in Capo Passero site, in Italy, were used for this study. The background light coming from ^{40}K decays and bioluminescence and the dark current of each PMT

were simulated. A total random background uncorrelated hit rate of 5 kHz for each PMT in a time window of 10 μ s before and after the event duration was assumed. In addition, time correlated hit rates due to genuine coincidences from ^{40}K decay have been simulated using GEANT [90] and refer to two-, three- and four fold hit coincidence in an OM. The two-fold coincidence refers to two hits within 20 ns in different PMTs of the same OM and corresponds to a rate of 500 Hz per OM, while the three- and four-fold coincidences correspond to 50 and 5 Hz respectively. These coincidence rates are in reasonable agreement with the results from the prototype optical module that was deployed in the Toulon site[52]. The contribution of light coming from bioluminescence in the Italian site is negligible (with a burst fraction of about 1%).

The chain for generating neutrinos and atmospheric muons, simulating particles, light and electronics and triggering and reconstructing events consists of several steps. Initially, the detector geometry file that contains the detector configuration and the characteristics of the site of the detector installation is created. Then, the detector file is used to generate neutrinos (GENHEN) or atmospheric muons (MUPAGE) for the corresponding detector geometry. Initial tracks are created and used to simulate charge particle interactions, the induced photons and their arrival times and distributions at PMTs (KM3). A file with the hits in the PMTs is created and used as input to JTriggerEfficiency [83]. This code is part of a set of algorithms, that simulate the PMT electronics and in parallel simulate random pulses coming from background sources. JTriggerEfficiency contains a set of criteria that check the positioning and time arrivals of photons in PMTs in order to reject hits coming from background sources. Pulses that pass the trigger level are used by the track reconstruction algorithms.

3.2.1 The detector geometry

The detector geometry file is created with the GENDET code [91]. It contains information about the configuration of the detector including the shape of the detector layout (hexagonal, circular, random, etc.), the type of photomultipliers (single-PMT or multi-PMT), PMT orientation and positioning and the distance between the optical modules. In this file the longitude, the latitude and the depth at the installation site are defined. The values used for the simulation of the ARCA detector refer to the corresponding values for the Capo Passero site and refer to a cylindrical detector at a depth of 3500 m. The layout for one block

3. THE KM3NET PROJECT - ARCA DETECTOR

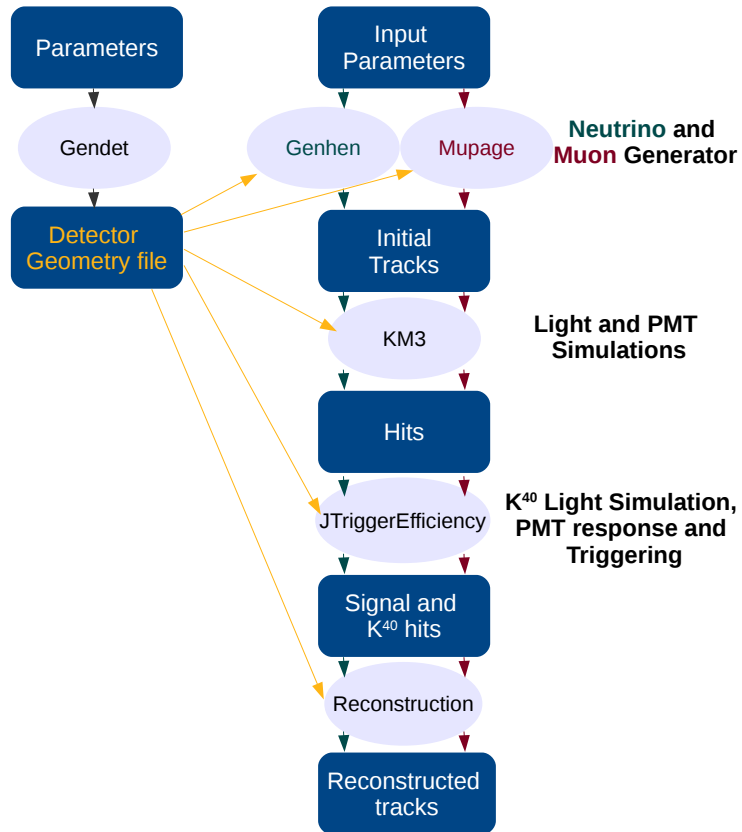


Figure 3.13: Scheme of the generation, simulation and reconstruction chain.

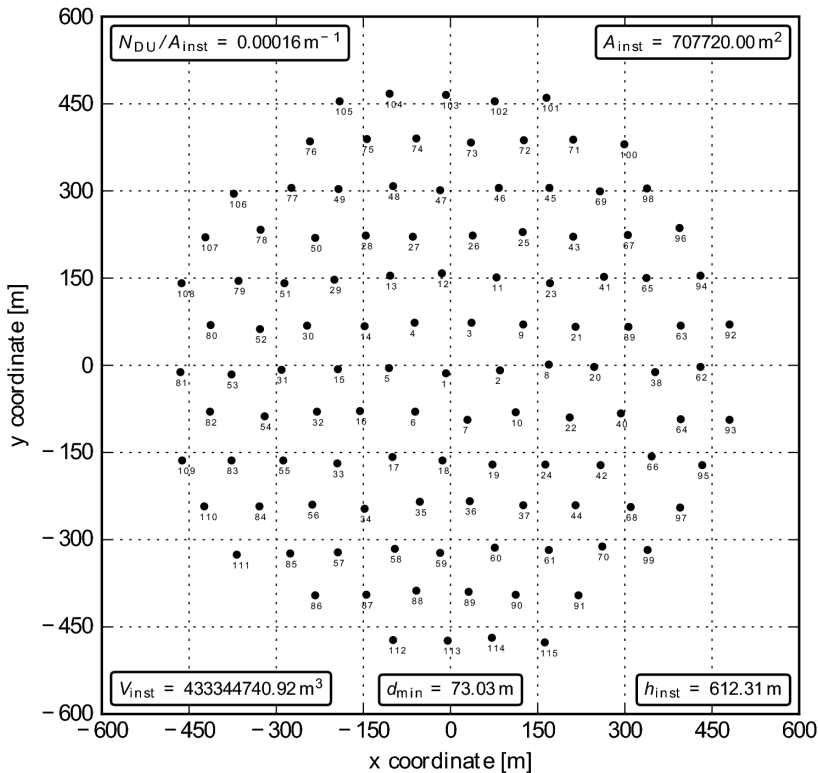


Figure 3.14: Layout of one block of the KM3NeT-ARCA detector.

of the ARCA detector produced by the simulation code is shown in Figure 3.14 and corresponds to an instrumented volume of $\simeq 0.5 \text{ km}^3$.

3.2.2 Neutrino event generation

GENHEN (GENERator of High Energy Neutrinos) [92] is a Monte Carlo event generator for high energy neutrinos that simulates the neutrino and anti-neutrino interactions with matter. The maximum energy of the (anti)neutrinos generated for this study is 10^8 GeV . The neutrinos are propagated through the Earth and the Preliminary Reference Earth Model is used to calculate the density profile [93]. The neutrino interactions are simulated with the LEPTO and RSQ packages, which are described in detail in [94], [95]. The LEPTO package computes the total cross sections and the kinematics of neutrino-nucleon charged current (CC) and neutral current (NC) interactions in the rock or the water around the detector for deep inelastic scattering, while RSQ is used to calculate the low energy quasi-elastic parts of the neutrino-nucleon interaction and Δ resonances.

3. THE KM3NET PROJECT - ARCA DETECTOR

Since the cross section of neutrino to muon interaction is very small, only neutrinos that interact to muons that are possible to be detected by the instrumented volume are generated. Thus the choice, to only simulate neutrinos that reach a defined volume, leads to a significant decrease in the computing time needed for the simulation. The ARCA instrumented volume is represented by a cylinder with radius of about 504 m and height of approximately 612 m. Cherenkov photons produced in a larger volume, which contains the cylinder and is named the can, can reach the PMTs and produce detectable signals. The radius and the height of the can is larger than the detector volume by approximately three times the absorption length of light in sea water (as can be seen in Figure 3.15) so photons produced outside the volume of the can have very low probability to reach a photomultiplier and generate signal. Following the same reasoning, the can is surrounded by a larger volume, the generation volume representing the volume where the neutrino interactions with nuclei and electrons in the matter surrounding the telescope happen, in order for muons to have a non-negligible probability to reach the can volume. The generation volume corresponds to the volume of the can expanded at the maximum lepton range in the medium (rock or sea water) for the maximum value of the energy range which is generated.

In case of neutrinos that have interacted inside the volume of the can, all particles for the neutrino interaction are simulated and recorded. If neutrinos have interacted outside the can, the shortest distance between the neutrino interaction vertex and the can is calculated. This distance is, then, compared to the maximum muon range for the corresponding neutrino energy. If this distance is smaller than the maximum muon range, the muon is transported to the can surface using one of the codes for muon propagation (MUSIC [96], MUM [97] or PropMu [98]). Otherwise the event is rejected as the muon would not reach the instrumented volume.

Neutrinos can be generated with GENHEN according to a specific $E^{-\gamma}$ spectrum where γ can be defined by the user. This energy spectrum is theoretically motivated by the Fermi shock acceleration mechanism which describes the production of high energy neutrinos. The γ index used for this analysis corresponds to $\gamma = 1.4$ as it gives reasonable statistics in the whole energy range from 10^2 GeV to 10^8 GeV. Neutrinos were uniformly generated in a zenith angle range $[0, \pi]$ and in an azimuth angle range $[0, 2\pi]$. The flux of neutrino events to the

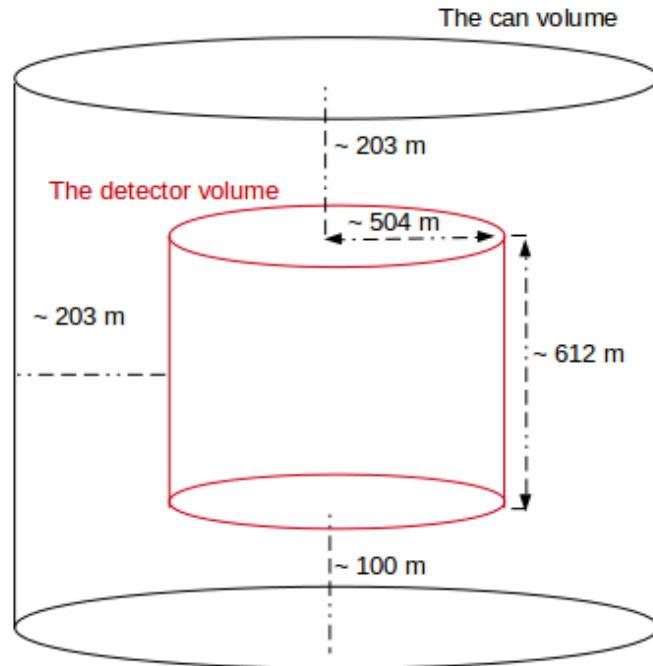


Figure 3.15: The detector and the can volume are illustrated.

ARCA detector can be re-weighted to another spectrum when it is necessary (as it is described in detail in [99]). In this spirit, the events used for the sensitivity studies in chapter 6 have been re-weighted to the astrophysical flux observed by IceCube.

3.2.3 MUPAGE: An atmospheric muon generator

The simulation of the extensive air showers that are initiated by cosmic ray interactions in the atmosphere of the Earth is a highly CPU time consuming procedure due to the high particle multiplicity of each event. In addition, the atmospheric muon flux is by several orders of magnitude higher than the astrophysical neutrino flux. Therefore, if one needs to simulate atmospheric muons for a given observation time, corresponding to the time needed to obtain adequate statistics of astrophysical neutrinos, he would end up with a huge number of atmospheric muon events. There are packages that perform detailed simulations of the extensive air showers (such as CORSIKA [100]), but the use of these packages for the simulation of the atmospheric muon flux for a detector with an instrumented volume of several cubic kilometers in terms of CPU needed, does

3. THE KM3NET PROJECT - ARCA DETECTOR

not allow the simulation of reasonable statistics. In order to simulate statistical samples of atmospheric muons that correspond to the atmospheric flux that a neutrino telescope would detect during few days or months of operation, a fast simulation program is necessary.

The MUPAGE package [101], [29] uses parametric formulas to calculate the flux of muon bundles, taking into account the muon multiplicity and the muon energy spectrum in a bundle, as a function of the distance from the axis of the shower. In particular, the flux of single and multiple muon events (consisting the muon bundle), their angular distribution and their energy spectrum has been parameterized for muons reaching the detector with zenith angles from 0° up to 85° . In the MUPAGE package the cylindrical volume where muons are generated can be defined by the user. For this study, muons are generated on the surface of the can that was used for the generation of neutrinos with the GENHEN code. A livetime for the number of simulated atmospheric muons is estimated by this package. This livetime corresponds to the time interval in which this number of muons would be generated according to the atmospheric muon flux. The parametrization of the cosmic rays interactions and the propagation of showers in the Earth's atmosphere (based on HEMAS code [29]) further reduces the time of the simulation. However, this simulation does not include the component of the secondary cosmic ray flux originating from the decay of charmed mesons and other short-lived particles produced during cosmic ray interactions in the atmosphere. Finally, muons produced by the decays of secondary mesons reaching the sea level are propagated down to a depth of 3500 m with the MUSIC code [96].

3.2.4 The KM3 simulation package

The particles are generated inside the volume of the can or are propagated up to the can surface, if they have been generated outside the can, with the codes described in the session above. The simulation of photons emitted along the path of charged particles produced by the neutrino interactions, are performed via the KM3 simulation package. The KM3 simulation package uses tabulated results, from full simulations with the GEANT package, of muons and electromagnetic cascades in the sea water to generate the number of photons reaching the PMTs. The full simulation of all the interactions of particles in the sea water and of all photons produced by these interactions is a time consuming procedure. In

order to reduce the CPU time necessary for these simulations, the KM3 package uses tables that contain information about the full wavelength dependence of Cherenkov light production, propagation, scattering and absorption in sea water, the response of the PMTs, including absorption in the glass and the optical gel, the PMT quantum efficiency and the reduced effective area for photons arriving off-axis [102].

The KM3 simulation package uses information from three different categories of tabulated results. Initially, the photon tables containing the distribution of generated photons by charged particles in sea water for segments of 2 m are read. The light coming from secondary particles is also included in these tables. Then, photon tables are used to calculate the probability that a photon hits a PMT, taking into account the intrinsic parameters of the PMT (response of the PMTs, absorption in the glass and the optical gel, the PMT quantum efficiency). Finally, the particles are propagated through the volume of the detector (using MUSIC code [96]) and the distributions of hits are produced for the PMTs of the detector configuration (defined by the user) based on the topology of each event and on the probability tables of hits that have already been created.

3.2.5 JTriggerEfficiency: Generation of pulses and optical background in PMTs and event triggering

3.2.5.1 Generation of pulses and optical background in PMTs

The hits in PMTs that have been produced with the KM3 package are used as input to JTriggerEfficiency in order to check if they can give detectable pulses in the output of PMTs, taking into account the characteristics of the PMTs used in KM3NeT, as they have been measured in the laboratory. Therefore, the transit time distribution per photon used in the simulation corresponds to an approximately Gaussian smearing with 2 ns sigma for the majority of photons. The Time over threshold (ToT) is also calculated using the information regarding the start time and the duration of the pulse and is set to a maximum of 255 ns. Moreover, the saturation of PMTs from photoelectrons arriving simultaneously has been taken into account and calculated to occur at $\simeq 40$ photoelectrons [83].

In order to simulate the light that will be collected by the PMTs in sea water, hits coming from ^{40}K decays are generated. This simulation includes both random noise hits with a rate of 5 kHz per PMT and hits at multiple

PMTs of the same OM resulting to 2, 3, 4 - fold coincidences with rates of 500, 50, 5 Hz per OM respectively.

3.2.5.2 Event triggering

Once the simulation of light that will be detected by the PMTs has been completed, a set of algorithms for event triggering are implemented in order to discriminate between hits from neutrino induced particles depositing light in the instrumented volume and noise hits producing pulses in PMTs which are misidentified as signal. In order to keep mostly hits related to neutrino interactions in sea water, the algorithms for event triggering search for OMs with hits of large amplitudes or hits on multiple PMTs of the same OM. Then, the L1 filter requires a coincidence of two or more hits from different PMTs in the same optical module within a time window of $T = 10$ ns (low scattering of light in deep sea water allows for such small time window) and consider PMTs with an angle between the PMT axes of direction less than 90° (L2 trigger). Then a directional filter is applied that uses a scan of the sky (with a step of approximately 10°) and an assumed neutrino direction in order to causally connect times within a spherical (cascade) or cylindrical (track) geometry. Finally, a requirement of at least 5 L1 hits is applied leading to a significant reduction of random coincidences due to noise hits [83].

4

Track Reconstruction

During the detector optimization studies for KM3NeT, several track reconstruction algorithms were developed. The *Chameleon* reconstruction will be described in this chapter. The performance of this reconstruction package before and after the improvements that were applied will be discussed. Finally, the *Chameleon* reconstruction will be compared with another track reconstruction, the *recoLNS*, which was also used throughout this thesis.

4.1 The Chameleon Track Reconstruction

The light collected in photomultipliers (PMTs) during the muon passage through sea water is used in order to reconstruct the muon and consequently the neutrino direction. The neutrino direction is almost co-linear with the muon track for high energy neutrinos. It is, therefore, possible to determine the parent neutrino direction by reconstructing the daughter muon track. As shown in Figure 4.1, the intrinsic angle between the muon and the neutrino direction is less than 0.5° for neutrinos with energy above 1 TeV, reaches 0.1° for neutrinos with energy above 20 TeV while it drops to less than 0.001° for neutrinos at the PeV energy range. The *Chameleon* reconstruction algorithm was used for the muon track reconstruction. This reconstruction package consists of two main parts. The hits pattern recognition which includes algorithms for the selection and grouping of PMT hits in track candidates and the fitting algorithm that uses a χ^2 minimizer in order to reconstruct the direction of the muon track [104].

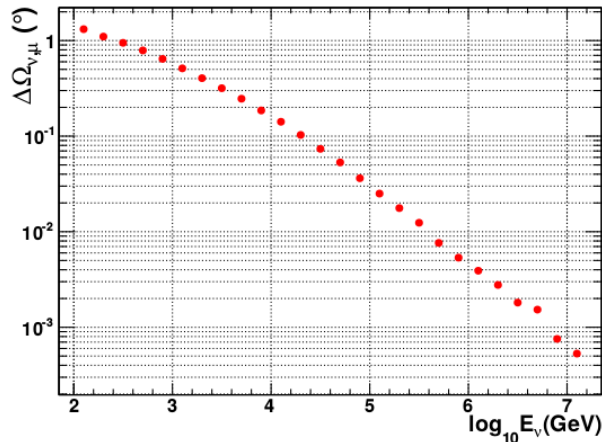


Figure 4.1: The intrinsic angle between the neutrino and muon direction ($\Delta\Omega$) as a function of $\log_{10} E_\nu$ [103].

4.1.1 Hits Pattern Recognition

One of the main sources of background noise in underwater neutrino telescopes consists of ^{40}K decays. Photons produced by random ^{40}K decays are detected by the PMTs together with photons produced by the muon passage through sea water. A χ^2 minimizer is very sensitive to hits from background noise contribution, therefore hits should be accurately selected before a fitting algorithm is applied. During the hit selection, two different filters are used to distinguish the hits from random ^{40}K decays, from hits originated by the muon passage through sea water. The first filter is based on an L1 trigger. Hits pass this trigger if there is a coincidence of two or more PMTs in the same OM in a time interval of 10 ns [83]. Throughout this analysis only L1 hits were used for the track reconstruction in order to reduce ^{40}K contribution. Then, the triggered hits pass through a series of hit selection algorithms. These algorithms, which are described in detail in [104], take into account the arrival time of hits in PMTs, the amount of charge collected per OM and the consistency of the hit pattern with the Cherenkov hypothesis in order to maintain the Cherenkov photons that are created as the muon travels through the sea water and discard hits coming from random ^{40}K decays.

4.1.2 Fitting Algorithm

The fitting algorithm uses a χ^2 minimizer in order to reconstruct the direction of the muon track. The arrival time of the hits that have passed the hit selection criteria and the corresponding PMT coordinates are recorded. The expected arrival times in these PMTs are calculated for different track candidates, assuming that these hits have been produced by Cherenkov photons and the track candidate that minimizes χ^2 is selected. The χ^2 function that is minimized is:

$$\chi^2 = \sum_i \frac{t_i^{expected} - t_i^{measured}}{\sigma_i},$$

where $t_i^{expected}$ is the expected arrival time, $t_i^{measured}$ is the measured PMT time and σ_i is the error associated with the i th hit [104].

4.2 Performance of the Track Reconstruction

A good angular resolution is critical for neutrino telescopes in order to point back to astrophysical neutrino sources. The performance of a track reconstruction algorithm is, thus, determined by the number of events which are reliably reconstructed and can point back to these sources. The angle difference between the simulated and the reconstructed track direction ($\Delta\Omega$) for all reconstructed events with the *Chameleon* reconstruction is shown in Figure 4.2. As it is shown in this figure, the direction is reconstructed very accurately ($\Delta\Omega \leq 1^\circ$) for most events. However, large angle differences leading to a loss in pointing accuracy can be observed. In particular, a peak at $\Delta\Omega \simeq 85^\circ$ is due to large uncertainties in the reconstruction of the azimuth angle ϕ . Therefore, events with $\Delta\Omega > 1^\circ$ or more indicate less accurately the origin of the parent neutrino in the sky compared to events with $\Delta\Omega \leq 1^\circ$ corresponding to pointing accuracy of sub-degree level. Throughout this thesis, events are considered and referred to as well reconstructed if tracks have an angle difference between the simulated and the reconstructed track direction less or equal to 1 degree ($\Delta\Omega \leq 1^\circ$). The track reconstruction uses the light collected in photomultipliers to reconstruct the muon direction. Therefore, it is expected to perform less efficiently for tracks passing outside the detector and do not cross the instrumented volume, thus depositing light in the borders of the detector. Although the reconstruction algorithm is applied to all events, in order to examine the overall performance of the *Chameleon*

4. TRACK RECONSTRUCTION

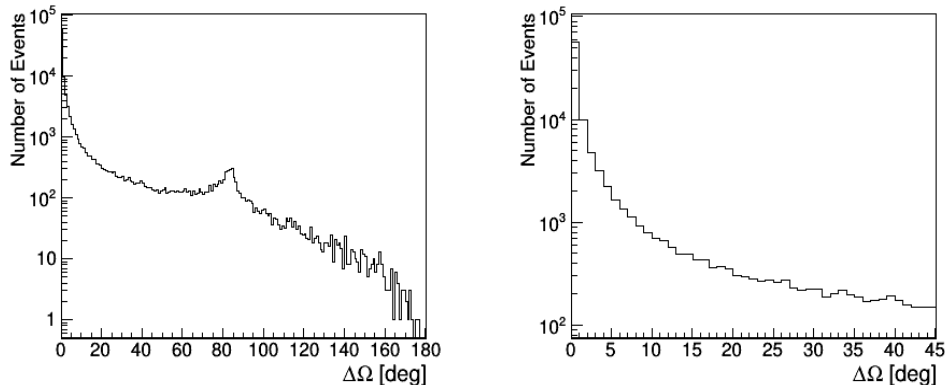


Figure 4.2: The angle difference between the simulated and the reconstructed track direction, $\Delta\Omega$, for all reconstructed events with the *Chameleon* reconstruction. The right plot is a zoom of the distribution of the angle difference for events with $\Delta\Omega < 45^\circ$.

reconstruction, only events that have crossed the detector (Figure 4.3) and the muon has deposited most of the light in the instrumented volume are considered.

The quality of a reconstruction can be defined as the ratio of the well reconstructed events over all reconstructed events. Figure 4.4 shows the distribution of the quality for the whole muon energy range. The quality of this algorithm for all the tracks that have been reconstructed is very low ($\leq 50\%$) (as can be seen in the black line of Figure 4.4) for muons in the lower energy range ($E_\mu < 10$ TeV), while for muons with higher energies ($E_\mu \geq 10$ TeV) a quality of $\simeq 65\%$ can be attained. For events crossing the detector, the quality increases for muons in the higher energy regime ($E_\mu \geq 10$ TeV) and reaches $\simeq 87\%$ for muons with energies at the PeV range. This reconstruction algorithm, based on a χ^2 fit, performs less efficiently for short tracks, as photons from the hadronic shower cannot be distinguished from Cherenkov photons leading to a misreconstruction of the track direction. High energy muons passing outside the detector (depositing the light in PMTs at the borders of the instrumented volume) are thus more likely to be misreconstructed than muons crossing the detector and so depositing the light in the instrumented volume. The quality though remains low for muons with energies $E_\mu < 10$ TeV crossing the detector as muons at these lower energies emit a smaller amount of photons compared to high energy muons. These tracks should then travel longer distances inside the detector in order to allow for the distinction of photons from the hadronic shower from Cherenkov photons and

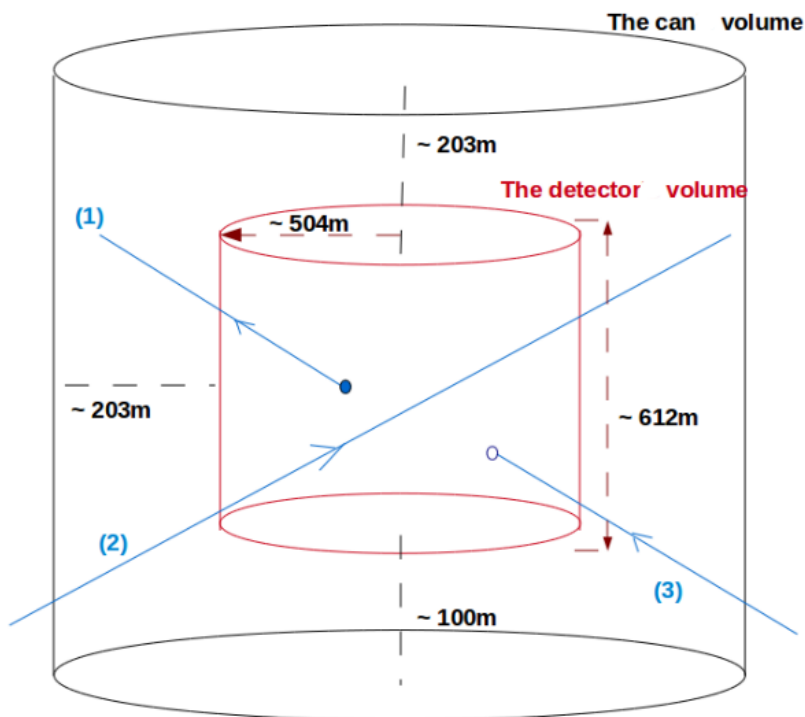


Figure 4.3: The detector and the can volume are illustrated. The events considered for this study could have been created inside the detector volume (1), could cross the detector (2) or could stop inside the detector volume (3). Events that pass outside the detector volume are not taken into account.

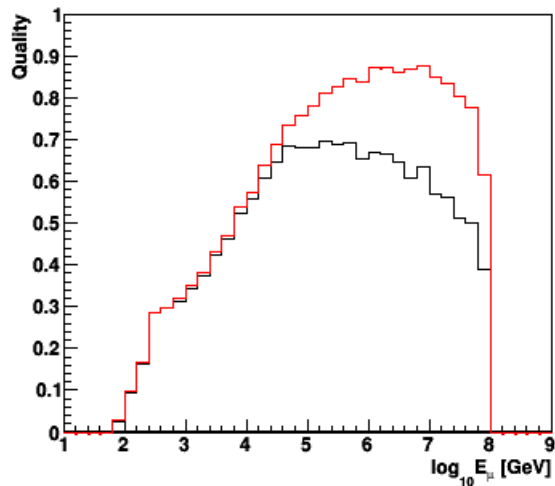


Figure 4.4: The quality of the reconstruction is shown as a function of $\log_{10} E_\mu$. The black line corresponds to all reconstructed events and the red line to all reconstructed events crossing the detector.

thus get reliably reconstructed. As it can be observed in Figure 4.4 most muons with energies $E_\mu < 10$ TeV are not likely to be reconstructed if they pass outside the detector. Finally, the drop of the quality for muons with $E_\mu \geq 60$ PeV is due to low statistics in this energy bin.

As discussed above, the events crossing the instrumented volume are more probable to get reliably reconstructed than events passing outside the detector. The percentage of poorly reconstructed events ($\Delta\Omega > 1^\circ$) passing outside the detector volume is $\simeq 20\%$ as reported in Table 4.1, while only $\simeq 3,5\%$ of the well reconstructed events do not cross the instrumented volume. The distribution of the muon energy for all reconstructed events and for events crossing the detector volume is shown in Figure 4.5. This figure also shows the ratio of well reconstructed events crossing the detector to all well reconstructed events with respect to the muon energy. Muons in the higher energy regime ($E_\mu \geq 1$ PeV) emit a large amount of very energetic photons during the passage through sea water and so these events are most probably reliably reconstructed even if they pass outside the instrumented volume. However, the selection of tracks crossing the detector volume results in a sample of reconstructed events with higher quality and so is favorable even for high energy muons.

$\frac{\text{Reconstructed events with } \Delta\Omega > 1^\circ \text{ that do not cross the detector}}{\text{All reconstructed events with } \Delta\Omega > 1^\circ}$	20%
$\frac{\text{Well reconstructed events } (\Delta\Omega \leq 1^\circ) \text{ that do not cross the detector}}{\text{All well reconstructed events } (\Delta\Omega \leq 1^\circ)}$	3.5%

Table 4.1: The percentage of poorly and well reconstructed events that do not cross the detector.

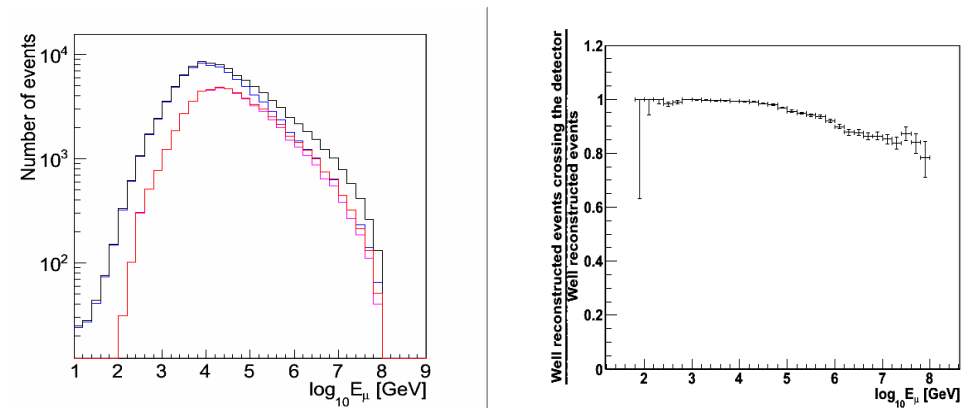


Figure 4.5: Left: The distribution of the reconstructed events for the whole muon energy range. The black line corresponds to all reconstructed events, the red line to all well reconstructed events, the blue and the magenta line correspond to all reconstructed and well reconstructed events respectively crossing the detector. Right: The ratio of well reconstructed events crossing the detector with respect to the $\log_{10} E_\mu$.

4.3 Reconstruction Improvements

The events considered here have crossed the detector and have deposited most of the light in the instrumented volume as described in section 4.2. Several improvements have been performed to the reconstruction algorithm and a quality selection has been established. In order to get a reliable reconstruction of the muon direction, the reconstructed tracks should satisfy the following quality selection.

- i. As the reconstruction is based on a χ^2 fit, a minimum number of OMs should have been hit in order to get a reliable direction determination. As it is shown in Figure 4.6, a selection of events with hits at 8 OMs used for the final fit in the reconstruction seems reasonable as an average quality of approximately 55% is achieved. A minimum number of 5 OMs with L1s is

4. TRACK RECONSTRUCTION

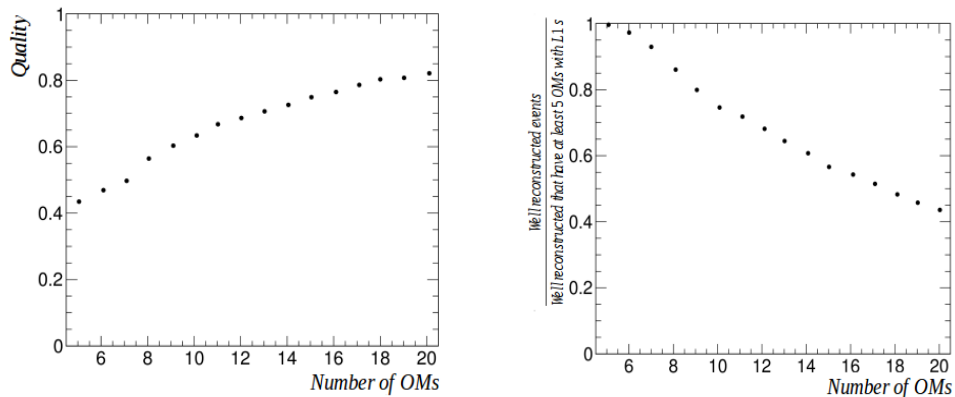


Figure 4.6: The quality of the reconstruction and the fraction of well reconstructed events with at least 5 OMs with L1s as a function of the required number of OMs with hits used by the reconstruction.

required to reconstruct an event. As it is shown in Figure 4.6 (right plot), more than 85% of the fraction of well reconstructed events satisfying this requirement, have hit at least 8 OMs. When a larger number of OMs with hits is required, the fraction of well reconstructed events that survive the selection decreases. The reconstruction algorithm is thus required to have used hits from at least at 8 OMs on at least 2 strings. This criterion enhances the efficiency for muons that have traveled an adequate path inside the instrumented volume and helps to reject tracks that pass near the border of the detector.

- ii. the *muon length* is required to be at least half the *maximum length possible*¹.

$$\frac{\text{Muon length}}{\text{Maximum length possible}} \geq 0.5$$

Muon length is defined as the distance between the first and the last photon emission point. All photons are assumed to be Cherenkov photons. *Maximum length possible* is the distance between the first photon emission point and the last possible photon production point (Figure 4.7). It is calculated by projecting the track direction to the intersection point with the detector and assuming a Cherenkov photon could hit the PMT closest to the detector border.

- iii. If the emission point of the majority of photons happens to be before the reconstructed muon vertex, the event is most probably poorly reconstructed.

¹As it has been shown in Figure 2.9, a muon with energy of 10 TeV travels more than 10 km.

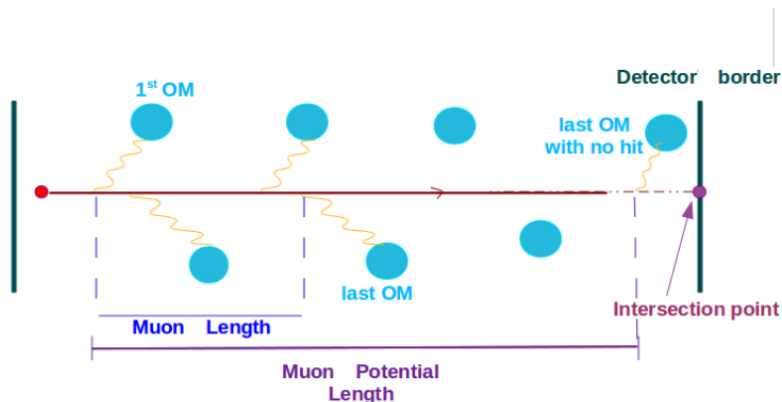


Figure 4.7: The muon length and the maximum length possible of the muon are illustrated.

This happens for events with a large amount of photons coming from the hadronic part compared to the number of Cherenkov photons or for events with only a small fraction of the muon track inside the detector. In the latter case, mostly photons from the hadronic part of the event are detected. These events can be rejected by counting the number of hits that lie behind the reconstructed vertex. A loose cut is applied: Events are accepted if less than 70% of the hits used for the reconstruction lie behind the reconstructed vertex:

$$\frac{N_{\text{hits behind the reconstructed vertex}}}{N_{\text{hits}}} \leq 0.7$$

The performance of the reconstruction after these selection criteria is investigated for all events. The number of well reconstructed events (events with angle difference $\Delta\Omega$ between the simulated and the reconstructed track direction less than 1°) that survive the selection criteria is compared to the number of misreconstructed events ($\Delta\Omega > 1^\circ$). Since in this analysis we focus on detecting a possible signal from diffuse flux, the performance of the reconstruction for high energy muon tracks with $E_\mu \geq 100$ TeV is also investigated.

Criterion (i) is the minimum criterion in order to accept reconstructed events. As the number of OMs hit depends on the muon energy, this requirement is expected to reduce the reconstruction efficiency for low energy events. The number of the events that fail to fulfill this criterion for all events and for events with $E_\mu \geq 100$ TeV are shown in Tables 4.2 and 4.3 respectively. The events rejected by this criterion refer mainly to the lower range of the energy spectrum with $E_\mu < 100$ TeV as can be seen from these tables. The 63 % of poorly

4. TRACK RECONSTRUCTION

reconstructed events fail to satisfy this requirement for the whole muon energy range, while for muons with $E_\mu \geq 100$ TeV a rejection of 13 % is achieved. The percentage of well reconstructed muons rejected by this cut is 0.12% for $E_\mu \geq 100$ TeV and 14% for the whole energy range.

$\frac{\text{Reconstructed events with } \Delta\Omega > 1^\circ \text{ rejected by the quality criterion (i)}}{\text{Reconstructed events with } \Delta\Omega > 1^\circ}$	63%
$\frac{\text{Well reconstructed events } (\Delta\Omega \leq 1^\circ) \text{ dropped by the quality criterion (i)}}{\text{Well reconstructed events } (\Delta\Omega \leq 1^\circ)}$	14%

Table 4.2: The percentage of poorly and well reconstructed events rejected by the quality criterion (i) is presented.

For $E_\mu \geq 100$ TeV:

$\frac{\text{Reconstructed events with } \Delta\Omega > 1^\circ \text{ rejected by the quality criterion (i)}}{\text{Reconstructed events with } \Delta\Omega > 1^\circ}$	13%
$\frac{\text{Well reconstructed events } (\Delta\Omega \leq 1^\circ) \text{ dropped by the quality criterion (i)}}{\text{Well reconstructed events } (\Delta\Omega \leq 1^\circ)}$	0.12%

Table 4.3: The percentage of poorly and well reconstructed events with $E_\mu \geq 100$ TeV rejected by the quality criterion (i) is presented.

$\frac{\text{Reconstructed events with } \Delta\Omega > 1^\circ \text{ rejected by the quality criteria}}{\text{Reconstructed events with } \Delta\Omega > 1^\circ \text{ satisfying the quality criterion (i)}}$	24%
$\frac{\text{Well reconstructed events } (\Delta\Omega \leq 1^\circ) \text{ dropped by the quality criteria}}{\text{Well reconstructed events } (\Delta\Omega \leq 1^\circ) \text{ satisfying the quality criterion (i)}}$	1%

Table 4.4: The percentage of poorly and well reconstructed events rejected by the quality criteria is presented.

The efficiency of the quality criteria (ii) and (iii) for well reconstructed events is $\simeq 99\%$ as inferred from Table 4.4 as only 1% of the well reconstructed events fails to meet the requirements (ii) and (iii). In Table 4.4 one can see that an additional rejection of $\simeq 24\%$ is achieved for events for which the reconstruction performs less efficiently leading to an angle difference between the simulated and the reconstructed track direction of $\Delta\Omega > 1^\circ$. The quality criteria (ii) and (iii)

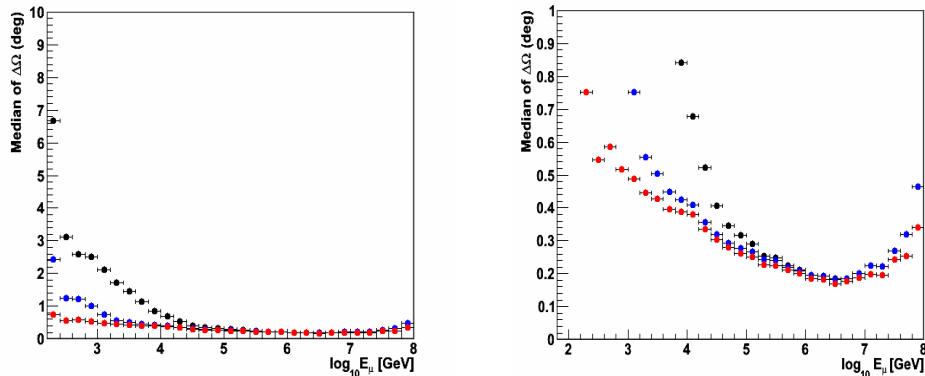


Figure 4.8: The median of the angle difference ($\Delta\Omega$) between the simulated and the reconstructed track direction is shown as a function of $\log_{10} E_\mu$. The right plot is a zoom of the distribution of the median of this angle difference for $\Delta\Omega < 1^\circ$. The black dots correspond to all events crossing the detector, the blue dots to the events that fulfill quality criterion (i) and the red dots refer to events satisfying all selection criteria ((i),(ii),(iii)).

reject $\simeq 28\%$ of poorly reconstructed events with $E_\mu \geq 100\text{TeV}$ and only $\simeq 0.2\%$ of the well reconstructed events (Table 4.5).

For $E_\mu \geq 100\text{TeV}$:

$\frac{\text{Reconstructed events with } \Delta\Omega > 1^\circ \text{ rejected by the quality criteria}}{\text{Reconstructed events with } \Delta\Omega > 1^\circ \text{ satisfying the quality criterion (i)}}$	28%
$\frac{\text{Well reconstructed events } (\Delta\Omega \leq 1^\circ) \text{ dropped by the quality criteria}}{\text{Well reconstructed events } (\Delta\Omega \leq 1^\circ) \text{ satisfying the quality criterion (i)}}$	0.2%

Table 4.5: The percentage of poorly and well reconstructed events with $E_\mu \geq 100\text{TeV}$ rejected by the quality criteria is presented.

The median of the angle difference ($\Delta\Omega$) between the simulated and the reconstructed track direction is shown in Figure 4.8. The median is less than 0.5° for $E_\mu > 1\text{TeV}$ while it reaches 0.38° for $E_\mu = 10\text{TeV}$. A very good angular resolution is achieved in the high energy regime with the median of $\Delta\Omega = 0.18^\circ$ for $E_\mu \simeq 3\text{PeV}$. For muon energies above 10PeV the calculation of the median is dominated by limited statistics.

The *effective area* is a quantity that describes the capability of a neutrino telescope to detect neutrinos from astrophysical sources. It is related to the number of detected events in a time interval for an astrophysical neutrino flux

4. TRACK RECONSTRUCTION

by:

$$\frac{N_{events}}{T} = \int dE_\nu \frac{d\Phi_\nu}{dE_\nu} A_\nu^{eff}(E_\nu)$$

where $A_\nu^{eff}(E_\nu)$ is the *effective area*, $\frac{d\Phi_\nu}{dE_\nu}$ is the astrophysical cosmic flux, T a time interval and N_{events} the number of detected events. The *effective area* gives an estimate of the ratio of the number of reconstructed events (N_{rec}) to the number of generated events (N_{gen}) for a given neutrino flux and is calculated by the following formula:

$$A_\nu^{eff}(E_\nu, \theta_\nu) = \frac{N_{rec}(E_\nu, \theta_\nu)}{N_{gen}(E_\nu, \theta_\nu)} V_{gen} \cdot \sigma(E_\nu) \cdot (\rho N_A) \cdot e^{-\sigma(E_\nu) \rho N_A z(\theta)}$$

where V_{gen} is the generation volume of the events, ρN_A is the target nucleon density, N_A the Avogadro number, σ the neutrino cross section and $z(\theta)$ the neutrino path across the Earth in a direction θ . Figure 4.9 shows the *effective area* (in m^2) for neutrinos versus $\log_{10} E_\nu$ (GeV) for all reconstructed events crossing the detector volume (black line) and for events satisfying the quality criteria (the blue line corresponds to events satisfying quality criterion (i) and the red line corresponds to events satisfying all quality criteria). A reduction of the *effective area* in the low energy range with $E_\nu < 10$ TeV can be observed as most events in this energy regime fail to satisfy the selection criteria. In the high energy range the majority of events fulfill the quality selection so as the energy increases, the selection criteria result in only a small reduction of the *effective area*. The *effective area* after the cuts is thus comparable to the initial values.

The efficiency (left plot) and the quality (right plot) of the selected events after the reconstruction are shown in Figure 4.10. The efficiency is defined as the ratio of the reconstructed events after selection cuts to the simulated events that have at least 5 OMs with L1s (trigger level condition), which is the minimum number OMs that can be used for the track reconstruction.

$$Efficiency = \frac{Reconstructed\ events\ after\ selection\ cuts}{Simulated\ events\ that\ have\ at\ least\ 5OMs\ with\ L1s}$$

The quality of the reconstruction is the ratio of the well reconstructed events to all reconstructed events satisfying the selection criteria. The events are referred as well reconstructed if the difference between the reconstructed and the simulated track direction is less or equal to 1 degree ($\Delta\Omega \leq 1^\circ$).

$$Quality = \frac{Well\ reconstructed\ events\ after\ selection\ cuts}{Reconstructed\ events\ after\ selection\ cuts}$$

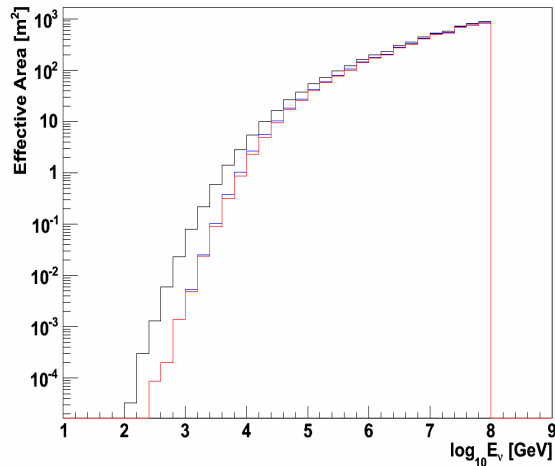


Figure 4.9: The neutrino *effective area* is shown as a function of $\log_{10} E_\nu$. The black line corresponds to all events crossing the detector, the blue line to the events that fulfill quality criterion (i) and the red line refers to events satisfying all selection criteria ((i),(ii),(iii)).

A good quality ($\geq 80\%$) of the reconstructed events especially in high energies ($E_\mu \geq 15\text{TeV}$) can be established, accompanied by an efficiency of $\simeq 67\%$ for $E_\mu \geq 15\text{TeV}$ and $\geq 82\%$ for $E_\mu \geq 40\text{TeV}$ rising with energy to approximately $\simeq 95\%$ for $E_\mu \geq 100\text{TeV}$. This can be seen in Figure 4.10, where the black line corresponds to all events crossing the detector, the blue line to the events that fulfill quality criterion (i) and the red line refers to events satisfying all selection criteria ((i),(ii),(iii)).

The several selection criteria are expected to equally favor all muon zenith angles. In order to ensure that the events surviving this selection do not depend on the incident angle of the track to the detector, the distribution of the reconstructed muon zenith angle for events that survive quality criteria (i), (ii) and (iii) is investigated. Results are shown in Figure 4.11 where one can see that all reconstructed angles are equally favored by the several selection criteria.

4. TRACK RECONSTRUCTION

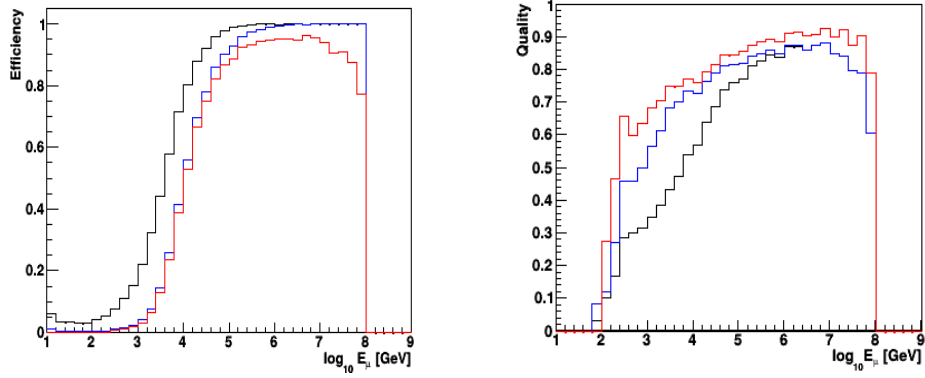


Figure 4.10: The efficiency and the quality of the reconstruction are shown as a function of $\log_{10} E_\mu$. The black line corresponds to all events crossing the detector, the blue line to the events that fulfill quality criterion (i) and the red line refers to events satisfying all selection criteria ((i),(ii),(iii)).

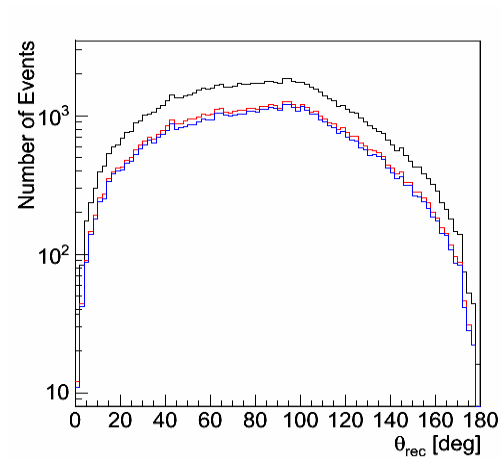


Figure 4.11: The distribution of the reconstructed muon zenith angle is shown. The black line corresponds to all events crossing the detector, the blue line to the events that fulfill quality criterion (i) and the red line refers to events satisfying all selection criteria ((i),(ii),(iii)).

4.4 Performance of the Track Reconstruction for an Alternative Detector Configuration

The performance of the *Chameleon* track reconstruction has been tested for events that were simulated with an alternative detector configuration. The distance between strings in this detector is 120 m compared to the 90 m string distance that was defined for the standard detector layout. The larger distance between strings leads to a 80% increase of the instrumented volume enhancing the detection ability for high energy neutrinos, which are of interest in these large neutrino telescopes.

For this detector configuration, the median of the angle difference ($\Delta\Omega$) between the simulated and the reconstructed track direction is shown in Figure 4.12. The median is less than 0.5° for $E_\mu > 1\text{TeV}$ while it reaches 0.4° for $E_\mu = 10\text{TeV}$. A very good angular resolution is achieved in the very high energy regime with a median of $\Delta\Omega = 0.25^\circ$ for $E_\mu \simeq 3\text{PeV}$. For muon energies above 10 PeV the calculation of the median is dominated by limited statistics.

Figure 4.13 (left plot) shows the *effective area* (in m^2) for neutrinos with respect to $\log_{10} E_\nu$ (GeV). A comparison between the *effective area* for this alternative detector layout and the effective area for the standard detector (90 m distance between strings) for events that fulfill quality criterion (i) and the selection criteria (i),(ii),(iii) is shown in Figure 4.13 (right plot). As it can be observed in this plot, the *effective area* decreases in the lower energy range for $E_\nu < 10\text{TeV}$ for the alternative detector, while it increases significantly in the high energy regime (at the PeV energy range) as the larger instrumented volume favors the detection of high energy muons. In these high energies, the vast majority of events fulfill the selection criteria and the *effective area* after the cuts is comparable to the initial values (all reconstructed events crossing the detector volume (black line)) as it is shown in Figure 4.13 (left plot).

A good quality ($\geq 80\%$) of the reconstructed events especially in high energies ($E_\mu \geq 100\text{TeV}$) can be established, accompanied by an efficiency of $\simeq 83\%$ for $E_\mu \geq 100\text{TeV}$ rising with energy to approximately $\simeq 95\%$ for muons with energy at the PeV range. This can be seen in Figure 4.14, where the black line corresponds to all events crossing the detector, the blue line to the events that fulfill quality criterion (i) and the red line refers to events satisfying all selection criteria ((i),(ii),(iii)).

4. TRACK RECONSTRUCTION

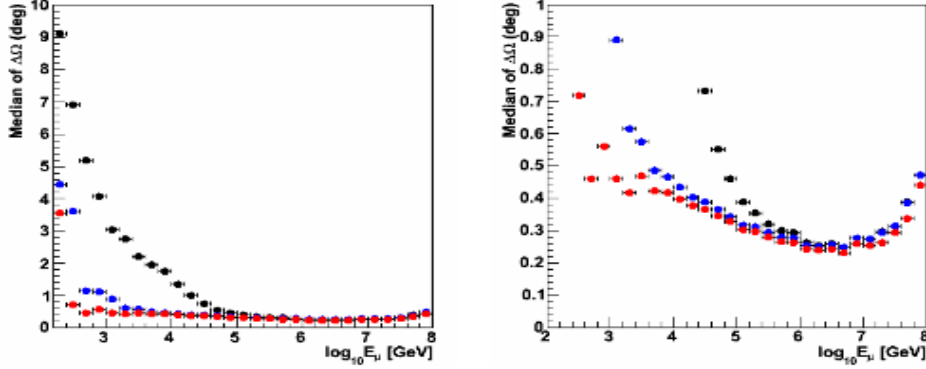


Figure 4.12: The median of the angle difference ($\Delta\Omega$) between the simulated and the reconstructed track direction is shown as a function of $\log_{10} E_\mu$ for the alternative detector configuration. The right plot is a zoom of the distribution of the median of this angle difference for $\Delta\Omega < 1^\circ$. The left plot contains all values of median with respect to $\log_{10} E_\mu$, while the black dots correspond to all events crossing the detector, the blue dots to the events that fulfill quality criterion (i) and the red dots refer to events satisfying all selection criteria ((i),(ii),(iii)).

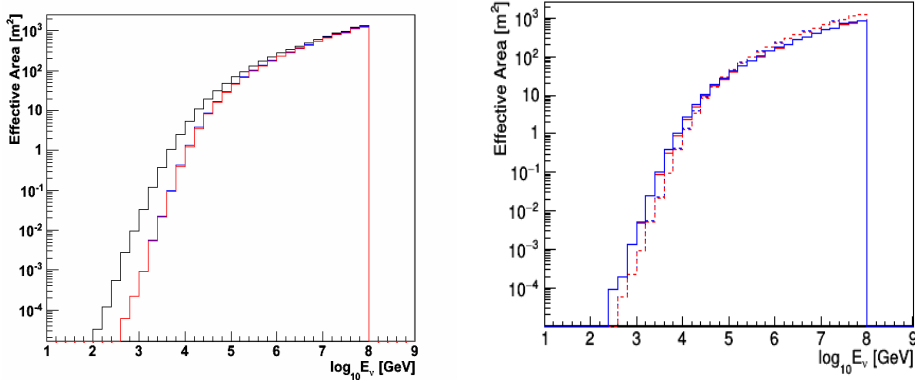


Figure 4.13: Left plot: The neutrino *effective area* is shown as a function of $\log_{10} E_\nu$ for the alternative detector geometry. The black line corresponds to all events crossing the detector, the blue line to the events that fulfill quality criterion (i) and the red line refers to events satisfying all selection criteria ((i),(ii),(iii)). Right plot: Comparison of the *effective area* for the standard (solid line) and the alternative (dashed line) detector configuration.

4.4 Performance of the Track Reconstruction for an Alternative Detector Configuration

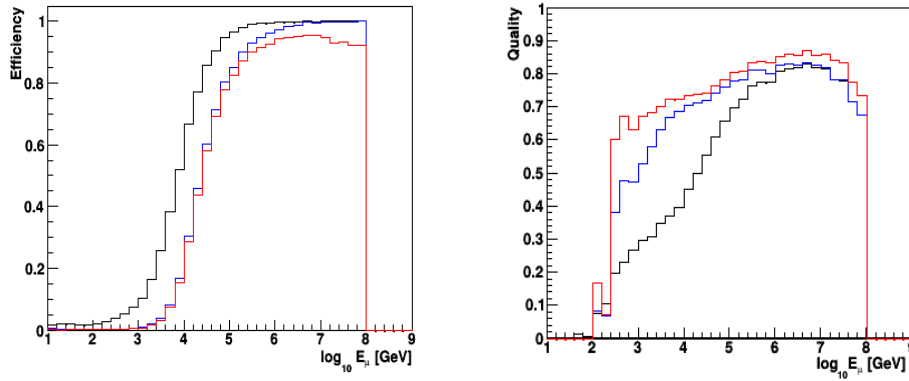


Figure 4.14: The efficiency and the quality of the reconstruction are shown as a function of $\log_{10} E_{\mu}$. The black line corresponds to all events crossing the detector, the blue line to the events that fulfill quality criterion (i) and the red line refers to events satisfying all selection criteria ((i),(ii),(iii)).

The dependence of the reconstructed muon zenith angle from the selection criteria (i), (ii) and (iii) has been studied. The distribution of the reconstructed muon zenith angle for events that survive quality criteria (i), (ii) and (iii) is shown in Figure 4.15, where one can see that all reconstructed angles are equally favored by the several selection criteria.

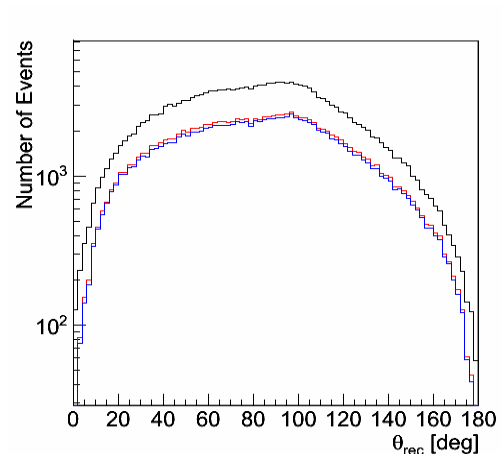


Figure 4.15: The distribution of the reconstructed muon zenith angle is shown. The black line corresponds to all events crossing the detector, the blue line to the events that fulfill quality criterion (i) and the red line refers to events satisfying all selection criteria ((i),(ii),(iii)).

4.5 Comparison between the Chameleon and the recoLNS Reconstruction Package

The performance of the *Chameleon* track reconstruction, which is based on a χ^2 fit, is compared with the performance of another track reconstruction package using a probability density function (pdf) in order to estimate the muon track direction, known as *recoLNS* [103]. All comparisons described in this section, refer to the standard detector geometry with an average distance of 90m between the strings, resulting in an instrumented volume of almost 0.5 km^3 .

In order to estimate the efficiency of each reconstruction method the number of the reconstructed tracks and the fraction of well reconstructed tracks as a function of the muon energy are investigated. Figure 4.16 shows the number of reconstructed (left plot) and well reconstructed (right plot) muon tracks as a function of $\log_{10} E_\mu$. Here, as in the previous sections, well reconstructed tracks refer to tracks that were reconstructed with an angle difference between the simulated and reconstructed muon direction less than 1° . The black line corresponds to events reconstructed with *recoLNS* and the red line refers to events reconstructed with *Chameleon*. Compared to *Chameleon*, the *recoLNS* algorithm reconstructs a larger amount of events in the lower energy range ($E_\mu < 50 \text{ TeV}$) while the number of events is comparable in the high energy regime, which is the energy regime of interest for a diffuse flux signal. A similar excess

4.5 Comparison between the Chameleon and the recoLNS Reconstruction Package

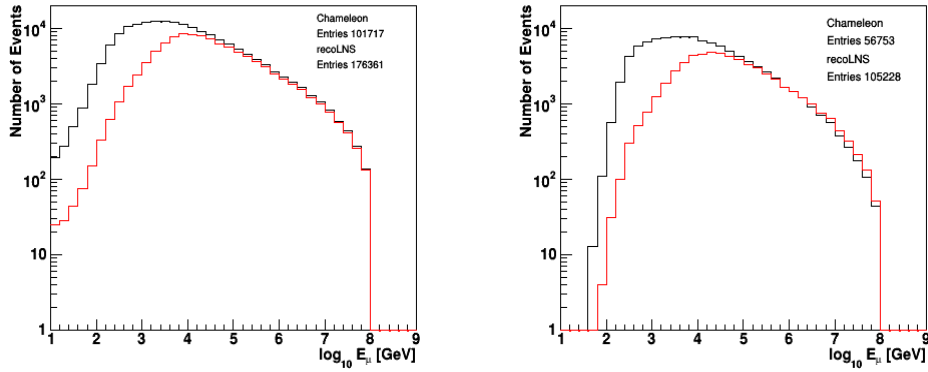


Figure 4.16: Left plot: Number of reconstructed events as a function of $\log_{10} E_\mu$. Right plot: Number of well reconstructed events ($\Delta\Omega \leq 1^\circ$) as a function of $\log_{10} E_\mu$. The black line corresponds to events reconstructed with *recoLNS* and the red line refers to events reconstructed with *Chameleon*.

of reconstructed tracks with *recoLNS* can be observed for well reconstructed events for tracks with $E_\mu < 50$ TeV. The number of well reconstructed tracks with *Chameleon* tends to be larger in the high energy regime though.

This study focuses to the measurement of the muon energy. Therefore, the events of particular interest for this study, are events that have crossed the detector (Figure 4.3) and so deposited a significant amount of the light in the instrumented volume. For this reason, the reconstruction algorithms are compared for these events and results are shown in Figure 4.17. The *recoLNS* algorithm is still more efficient for $E_\mu < 50$ TeV as both the fraction of reconstructed and well reconstructed events is larger, while for muons with higher energies ($E_\mu \geq 50$ TeV) both reconstruction algorithms have comparable behavior.

Each reconstruction package has criteria in order to select the tracks that are well reconstructed and in parallel reduce the amount of poorly reconstructed tracks in the event sample. The performance of these reconstruction packages is compared for the final event samples after this selection. The selection criteria applied for the *Chameleon* reconstruction are criteria (i), (ii) and (iii) mentioned at section 4.3, while the selection criterion for the *recoLNS* reconstruction is calculated as the maximum log-likelihood value per degree of freedom found by the fit. This criterion is named Λ and the events with $\Lambda > -5.8$ are selected in the final event sample [105], [103]. Figure 4.18 shows the energy distributions for the reconstructed events crossing the detector that are selected by these reconstruc-

4. TRACK RECONSTRUCTION

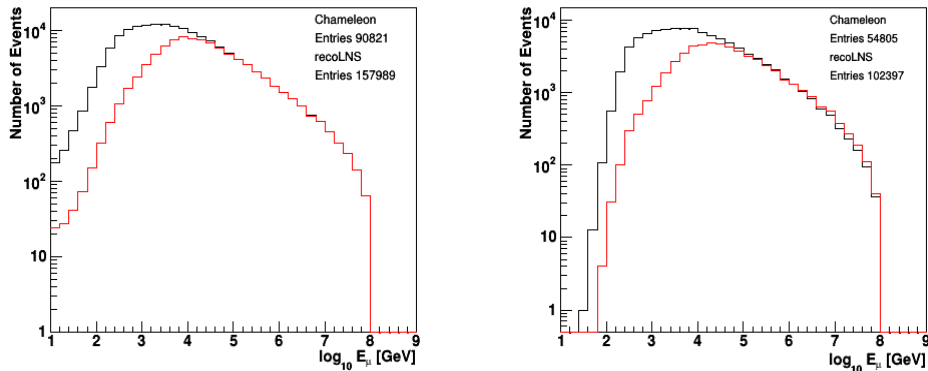


Figure 4.17: Left plot: Number of reconstructed events as a function of $\log_{10} E_\mu$ for events crossing the instrumented volume. Right plot: Number of well reconstructed events ($\Delta\Omega \leq 1^\circ$) as a function of $\log_{10} E_\mu$ for events crossing the instrumented volume. The black line corresponds to events reconstructed with *recoLNS* and the red line refers to events reconstructed with *Chameleon*.

tion algorithms. For the final event selections, the numbers of all reconstructed tracks and well reconstructed tracks are comparable for both reconstruction algorithms within the high energy range, while in the lower energies the *recoLNS* reconstructs a small portion of additional tracks.

In order to make the comparison of the reconstruction algorithms more precise, a study of the angular resolution is essential. The pointing accuracy that is obtained with the *recoLNS* method is shown in Figure 4.19. Compared to the *Chameleon* (Figure 4.8), the *recoLNS* reconstruction provides a better angular resolution for $E_\mu < 50$ TeV. For muons with energies in the high energy range the results are comparable for both reconstructions, while *Chameleon* has a better pointing accuracy for muons at the PeV energy range.

4.5 Comparison between the Chameleon and the recoLNS Reconstruction Package

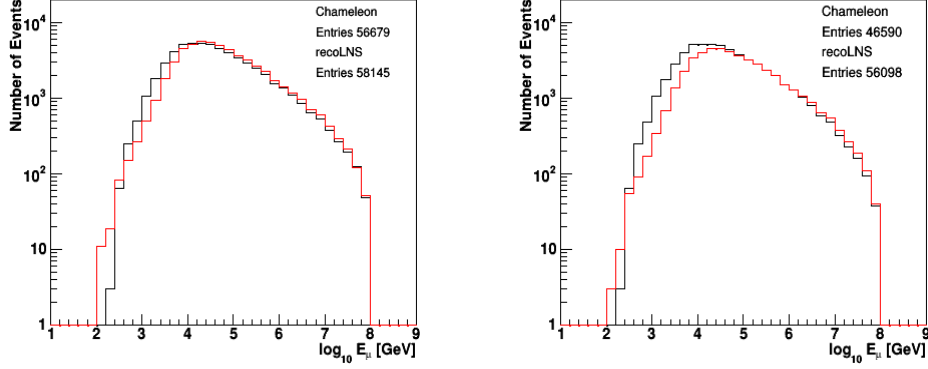


Figure 4.18: Left plot: Number of reconstructed events as a function of $\log_{10} E_\mu$ for events crossing the instrumented volume and survive the selection criteria. Right plot: Number of well reconstructed events ($\Delta\Omega \leq 1^\circ$) as a function of $\log_{10} E_\mu$ for events crossing the instrumented volume and survive the selection criteria. The black line corresponds to events reconstructed with *recoLNS* and the red line refers to events reconstructed with *Chameleon*.

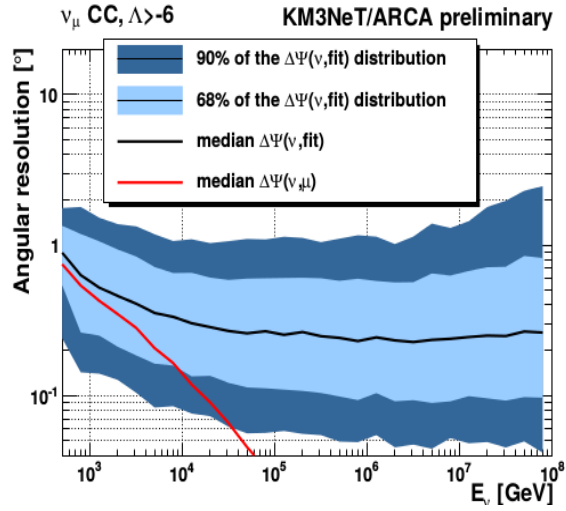


Figure 4.19: The median of the angle difference ($\Delta\Omega$) between the simulated and the reconstructed track direction with 68% and 90% quantiles is shown as a function of $\log_{10} E_\nu$, taken from [103]. The red line refers to the intrinsic angle between the neutrino and muon direction.

4. TRACK RECONSTRUCTION

5

Energy Reconstruction with Neural Networks (EReNN)

5.1 Scientific Motivation

The reconstruction of muon and consequently the neutrino energy is critical in neutrino telescopes. The spectrum of astrophysical neutrinos that constitute the signal of the detector extends to higher energies compared the to background from atmospheric ν_μ that reach the detector volume and mimic our signal (Figure 5.1). The energy estimation is, therefore, essential for the discrimination of neutrinos and muons coming from the CC interactions of astrophysical neutrinos with the water or the rock below the detector, from atmospheric ν_μ and μ events. Moreover, the determination of the energy is a major parameter in the identification of the neutrino sources that affects all analyses performed in Cherenkov detectors, such as searches for point sources of neutrinos, diffuse extraterrestrial neutrinos, neutrino oscillations, and measurements of the total neutrino-nucleon cross section via neutrino absorption in the Earth.

Muons lose energy via ionization and by stochastic processes, such as bremsstrahlung, pair production, and photonuclear interactions. The total average energy loss of the muon is:

$$\frac{-dE}{dx} = a(E) + b(E) \cdot E_\mu \quad (5.1)$$

where $a \simeq 0.274 \text{ GeV } m^{-1}$ accounts for the energy loss due to ionization and $b \simeq 0.000349 \text{ m}^{-1}$ is due to the stochastic energy loss. Muons with $E_\mu > 1 \text{ TeV}$ lose energy stochastically, while for lower energies ionization dominates as can be

5. ENERGY RECONSTRUCTION WITH NEURAL NETWORKS (ERENN)

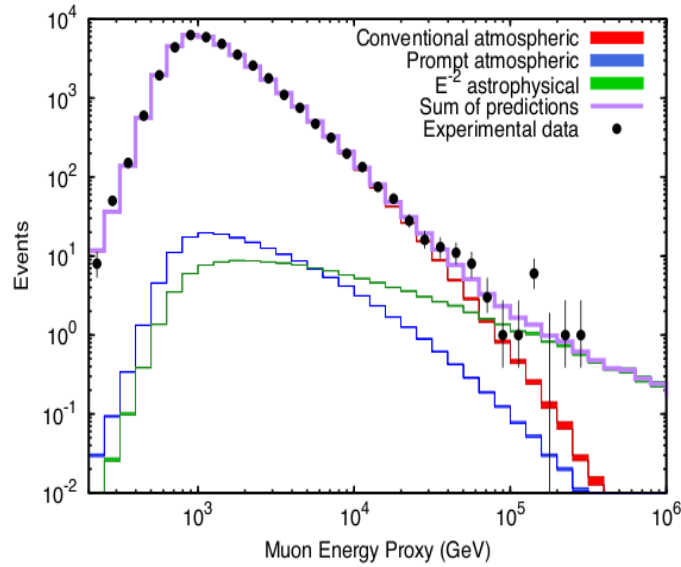


Figure 5.1: The energy spectrum for atmospheric neutrinos and neutrinos of astrophysical origin as predicted by theoretical models. The black dots correspond to the experimental data from the IceCube Collaboration [33].

seen in Figure 5.2 [106]. In the following sections we describe a method to derive muon (and neutrino) energy from the light collected along its passage through the detector volume.

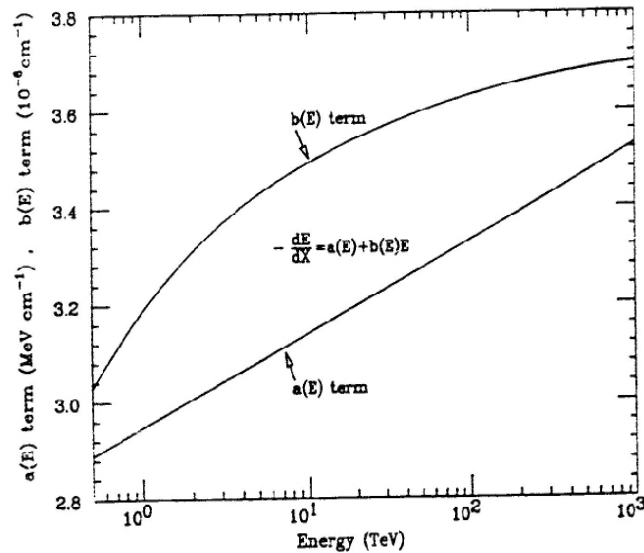


Figure 5.2: The evolution of parameters a and b as a function of energy for muons traveling in water [106].

5.2 Data Selection

Since the determination of neutrino and muon energy is based on the collection of light in PMTs, some minimum requirements should be fulfilled in order to get a reliable energy estimator.

Muons should travel an adequate distance inside the instrumented volume thus depositing the light in photomultipliers before an attempt to evaluate their energy is made. In order to select such events (that cross the detector) (Figure 4.3) and in parallel separate them from events with the muon passing outside the instrumented volume that mostly deposit the light in the border strings of the detector, the following formula is introduced:

$$\frac{\text{Number of border strings}}{\text{Number of strings}} < \frac{1}{2} \quad (5.2)$$

where the *number of strings* refers to the total number of strings with hits that have been used for the final fit of the track reconstruction and the *number of border strings* refers to the total number of these strings that lie in the circumference of the detector.

Figure 5.3 shows the events that satisfy (left plot) and do not satisfy this condition (right plot) as a function of $\log_{10}E_{\mu}$. As can be seen in this figure, 85.4% of the events that cross the detector satisfy this criterion and are referred to as well contained events, while 77.7% of the events that do not satisfy this selection pass outside the instrumented volume. Most events with muon energy at the PeV range are reconstructed to cross the detector. Muons at these high energies emit energetic photons that are detected from both the border and the internal strings of the detector. High energy muons can, therefore, satisfy the condition (5.2) even if they pass outside the instrumented volume.

A minimum muon path inside the instrumented volume is required for well contained muons. Only well contained muons for which the direction of the muon track has been reliably reconstructed (events that satisfy the selection criteria (i), (ii) and (iii) described in section 4.3) are considered. In order to determine this minimum muon path one should take into account that the optical modules (OMs) in the detector configuration are not homogeneously distributed in space. The distance of OMs on a string is 36 m while the distance between neighboring strings is approximately 90m. Consequently, a horizontal muon traveling a distance in the detector would meet approximately 50% less OMs

5. ENERGY RECONSTRUCTION WITH NEURAL NETWORKS (ERENN)

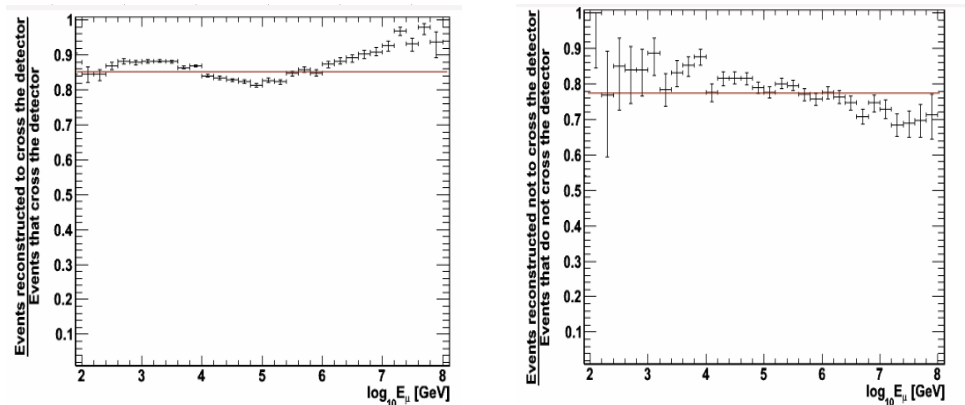


Figure 5.3: Left: The ratio of the events that are reconstructed to cross the detector based on equation (5.2) to the events that cross the detector with respect to $\log_{10} E_\mu$. Right: The ratio of the events that are reconstructed not to cross the detector based on equation (5.2) to the events that do not cross the detector with respect to $\log_{10} E_\mu$.

along its path compared to a vertical muon traveling the same distance. In order to account for this inhomogeneity in the spatial distribution of OMs, the minimum muon path through the detector should differ with the muon zenith angle. We define the minimum muon path (L) by the formula:

$$L = \frac{1}{2} \cdot h + (R - \frac{1}{2} \cdot h) \cdot \sin \theta_{rec} \quad (5.3)$$

where L : the distance traveled inside the instrumented volume by a well contained muon, h : the detector height, R : the detector radius and θ_{rec} : the reconstructed muon zenith angle. According to this formula the minimum muon path for horizontal muons ($\theta_{rec}=90^\circ$) is the detector radius ($L=504\text{m}$), while for vertical muons it is half the height of the string ($L=306\text{m}$)¹. This can be seen in Figure 5.4 which shows the minimum muon path as a function of the sine of the reconstructed muon zenith, $\sin \theta_{rec}$.

We calculate the maximum distance of the PMT positions, L_{rec} , considering PMTs that have been used by the track reconstruction. Specifically, we find the pair of PMTs for which the distance between their positions is maximum. This calculation does not include the reconstructed track direction in order to avoid bias due to poorly reconstructed events. Then, we accept events that fulfill the requirement:

¹The path length for a muon with energy of 10 TeV exceeds 10 km, as shown in Figure 2.9.

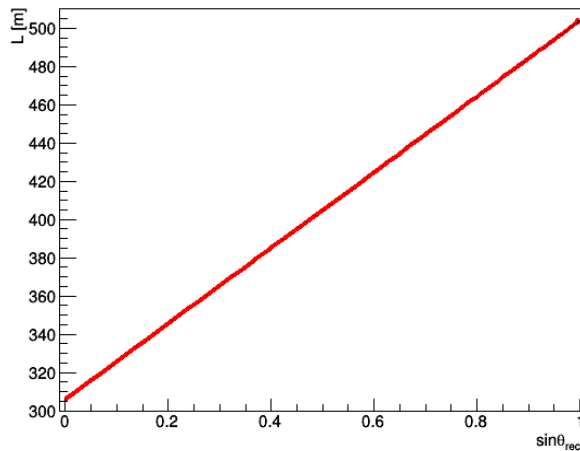


Figure 5.4: The minimum muon path, L , as a function of the sine of the reconstructed muon zenith, $\sin\theta_{rec}$.

$$L_{rec} \geq 0.3L \quad (5.4)$$

The events that satisfy this condition are expected to be better candidates for the estimation of energy. It has been observed, though, that the muon and neutrino energy is underestimated if the majority of detected hits are not compatible with the Cherenkov hypothesis but are either due to photons coming from the hadronic shower, corresponding to tracks that escape the detector volume or due to scattered photons from particles other than the muon. These types of events can be excluded by setting a limit on the χ_{nDoF}^2 value:

$$\chi_{nDoF}^2 = \frac{\sum \frac{(t_{exp} - t_{meas})^2}{error^2}}{N_{hits} - (nDoF - 1)} < 2. \quad (5.5)$$

where N_{hits} stands for the number of hits used by the track reconstruction, $nDoF$ stands for the number of Degrees of Freedom and $nDoF - 1 = 5$, $error \simeq 2.5$ ns, t_{meas} is the time (in ns) measured in the PMT, t_{exp} is the expected arrival time of the photon in the PMT using the direction of the muon from the track fit and assuming this is a Cherenkov photon.

In order to enhance the contribution of Cherenkov photons, only photons with an angle $\theta < 60^\circ$ between the photon from the reconstructed track and the PMT direction are considered for the evaluation of χ_{nDoF}^2 .

5. ENERGY RECONSTRUCTION WITH NEURAL NETWORKS (ERENN)

If the

$$L_{rec} \geq L \quad (5.6)$$

the condition (5.5) can be loosened to:

$$\chi_{nDoF}^2 < 5.5 \quad (5.7)$$

as the muon has already traveled enough distance inside the detector volume and the energy can be determined.

According to the above requirements the muon and neutrino energy is determined if one of the following set of criteria is satisfied:

i. $0.3L \leq L_{rec} < L$ and $\chi_{nDoF}^2 < 2$

or

ii. $L_{rec} \geq L$ and $\chi_{nDoF}^2 < 5.5$

The events that satisfy the criteria mentioned above (that will be referred as containment selection) have deposited the light inside the instrumented volume and the muon energy can be reliably reconstructed. This can be seen in Figure 5.5. This figure shows the number of hits used by the track reconstruction as a function of the muon energy for events satisfying (left plot) and not satisfying (right plot) the containment selection. The number of hits for events satisfying the containment selection shows a strong dependence on the muon energy. Consequently, the muon energy for these events can be reliably estimated. On the other hand, the events that fail the containment selection have deposited only a portion of the light inside the detector leading to a weak dependence of the number of hits with the muon energy (Figure 5.5 right plot). Therefore, the muon energy cannot be reliably determined. For these events only a lower limit of the muon energy will be reported. In order to reconstruct the muon and neutrino energy an artificial Neural Network with appropriate input variables is employed. The operation of neural networks is described in section 5.3 and the input variables that are used to estimate the energy are presented in section 5.4.

5.3 Artificial Neural Networks

Artificial Neural Networks (NNs) are gaining ground as a multipurpose, robust computational methodology which is able to perform effectively in many analyses.

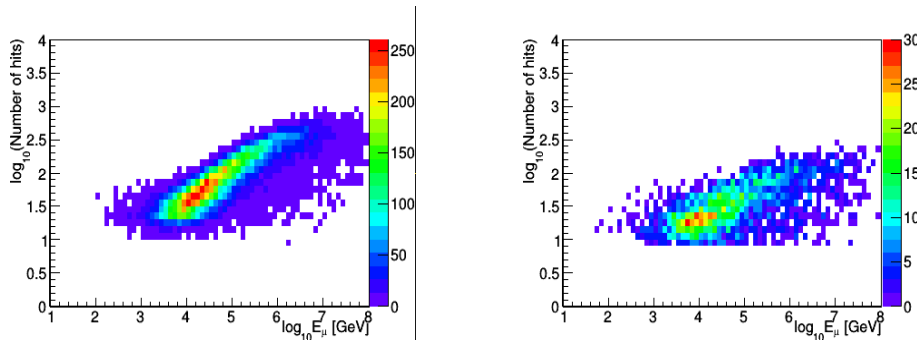


Figure 5.5: The number of hits used by the track reconstruction with respect to $\log_{10} E_\mu$ for events satisfying the criteria (i), (ii) (left plot) and events failing to satisfy these criteria (right plot).

The idea to use neural networks in data analysis is based on the function of biological neural networks in the brain of animals and humans.

The human brain is a highly complex organ consisting of about 10^{11} neurons with 10^{15} connections between them [107]. Compared to the human brain, the artificial neural networks are based in a less complex architecture. NNs are composed of individual elements, the neurons and the neural connections between them. Each neuron receives an initial incentive and transmits the information to the neighboring neuron, mimicking the neuronal connections in our brain. The response of an artificial neural network is determined by the layout of the neurons, the weights of the inter-neuron connections and the neuron response function which describes the response of the neurons to the input variable (the initial incentive).

5.3.1 Multi-Layer Perceptron Neural Network

This analysis is based on the employment of a Multi-Layer Perceptron (MLP) Neural Network which is part of the TMVA package included in ROOT [108]. The neurons in such kind of neural network are organized in layers and direct connections from a given layer are allowed only to the following layer resulting in a less complex system. The first layer of a MLP is the input layer. Each neuron holds an input variable. The last layer is the output layer that holds the output variable, the neural network estimator. All intermediate layers are the hidden layers of the NN. A weight is associated to each directional connection between the output of one neuron and the input of another neuron (Figure 5.6). During the calculation of the input value to the response function of a neuron,

5. ENERGY RECONSTRUCTION WITH NEURAL NETWORKS (ERENN)

these weights are multiplied with the output values of all neurons connected to this given neuron [108].

The NN used for the current analysis consists of three layers. The first layer holds four input variables, the hidden layer consists of 10 nodes and the output layer returns the network result. The choice of one hidden layer for this analysis is based on the *Universal Approximation Theorem*. According to this theorem, "a feed-forward neural network with a single hidden layer consisting of a finite number of neurons (such as a MLP Neural Network) can arbitrarily well approximate continuous functions on compact subsets of \mathbf{R}^n , using any continuous sigmoidal (or hyperbolic tangent) nonlinearity as the activation function" [109]. The neuron activation function used for this analysis is the hyperbolic tangent while the weights were adjusted with the use of the Broyden-Fletcher-Goldfarb-Shannon (BFGS) method [110]. After several tests, the hidden layer was chosen to contain 10 nodes as this NN architecture leads to faster and better convergence between the simulated and the reconstructed muon energy during the different epochs of NN training.

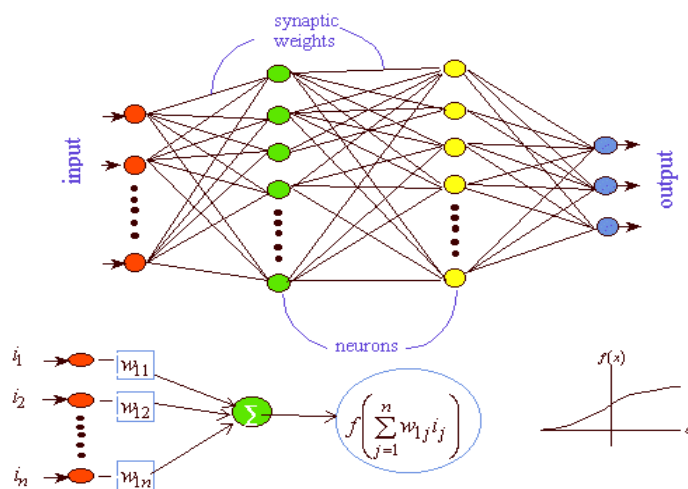


Figure 5.6: Example of a Multilayer Perceptron Neural Network with two hidden layers.

5.4 Input Parameters of the Neural Network

For all events for which the direction of the muon track has been reliably reconstructed (events that satisfy the selection criteria (i), (ii) and (iii) described in

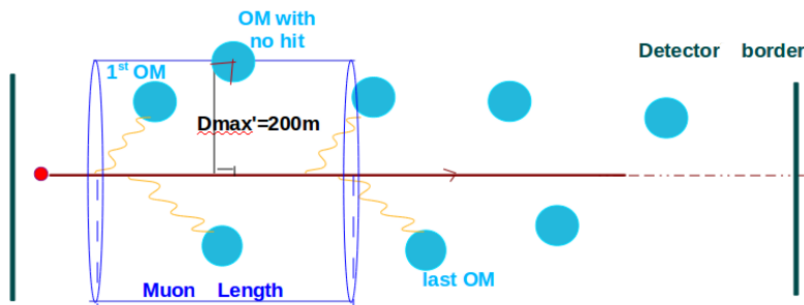


Figure 5.7: The layout of PMTs without hits that are considered for the muon energy estimation, is illustrated. These PMTs are located in a cylinder with height equal to the muon length and radius of 200m.

section 4.3), we make use of additional information which depends on the muon energy. However, these events are discriminated to events that satisfy the containment selection (described in section 5.2) for which the muon energy can be reliably reconstructed and events that fail to satisfy the containment selection for which only a lower limit of the muon energy will be reported.

We take into account the PMTs that have recorded hits, as well as the PMTs that have no hit but are possible candidates of having hits according to the reconstructed track direction. We consider a cylinder (shown in Figure 5.7) with a radius of 200 m¹ and height equal to the muon length. The muon length is defined as the distance between the first and the last photon emission point. All photons are assumed to be Cherenkov photons. PMTs that have not been hit are considered if the supplementary angle between the track and the PMT direction is in the range ($6^\circ, 86^\circ$] in order to consider photons of the Cherenkov wavefront (as it can be seen in Figure 5.8).

The quantities which depend on the muon (and neutrino) energy and are used as input variables to feed the Neural Network are:

- i. The *number of OMs* used in the reconstruction divided by the *maximum length possible* (as explained in Figure 4.7). This variable helps to discriminate between events with low energies that stop traveling inside the detector from events with higher energies that have hit comparable number of OMs but escape the instrumented volume.

¹Taking into account the absorption length, most photons will have been absorbed after this distance.

5. ENERGY RECONSTRUCTION WITH NEURAL NETWORKS (ERENN)

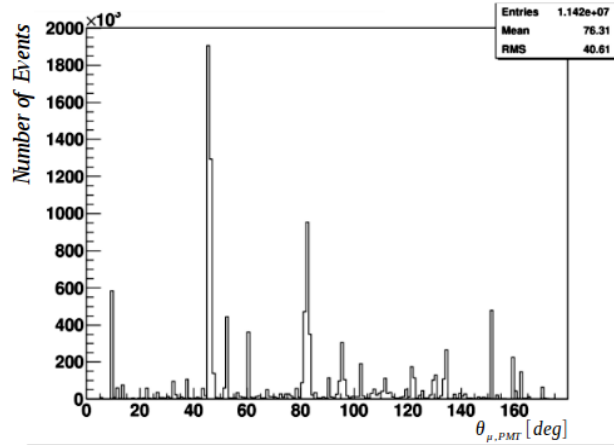


Figure 5.8: The angular distribution between the muon track and the PMT direction for simulated muons traveling through sea water.

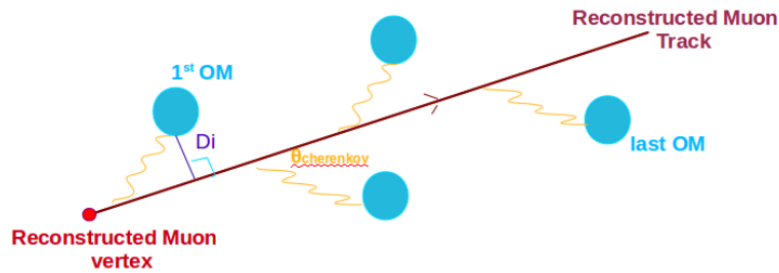


Figure 5.9: Each PMT is weighted according to its vertical distance (D_i) from the reconstructed track.

$$\frac{\text{Number of OMs}}{\text{Maximum length possible}}$$

ii. The *number of PMTs* that have L1 pulses and were used in the reconstruction weighted according to the vertical distance from the track as explained in Figure 5.9.

$$\sum_{i=1} \text{Number of PMTs} \frac{D_i}{D_{max}}$$

where D_i is the vertical distance between the PMT and the reconstructed track and D_{max} the corresponding maximum distance. Figure 5.10 shows the maximum vertical distance between the PMTs with hits and the simulated muon track. As it can be seen, for the majority of events D_{max} is less than 500 m ¹.

¹ Given the absorption length, there is a negligible probability that photons have not been absorbed after this distance.

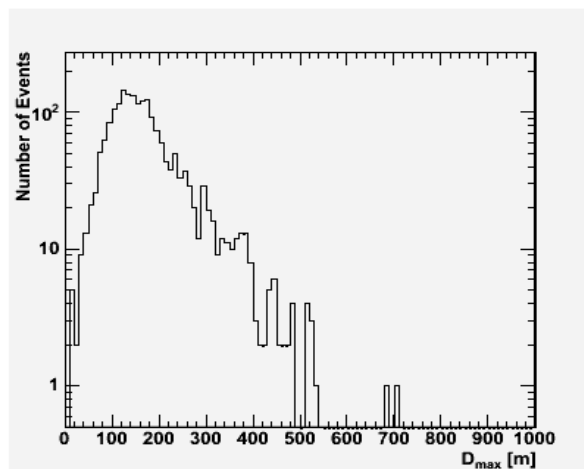


Figure 5.10: The maximum vertical distance, D_{max} , between the PMT and the simulated muon track.

iii. The ratio of the total number of PMTs that have L1 pulses and were used in the reconstruction to the number of PMTs that could be hit according to the track and the PMT direction (as shown in Figure 5.7) but have not recorded any pulses.

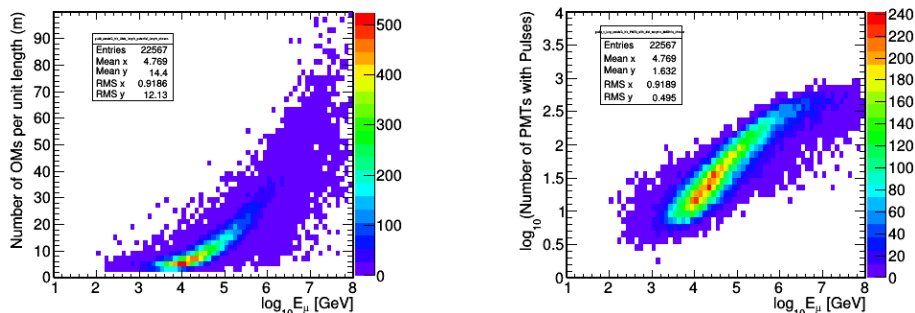
$$\frac{\text{Number of PMTs with hits}}{\text{Number of PMTs with no hits}}$$

iv. The *Total Time over Threshold (ToT)* of all PMTs used in the reconstruction.

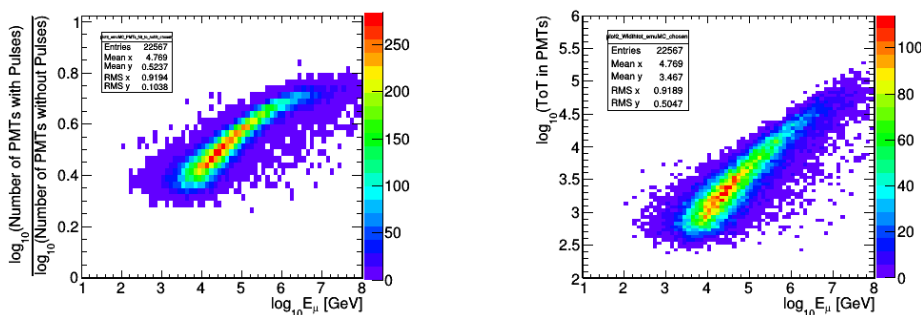
$$\sum_{i=1}^{\text{Number of PMTs}} ToT$$

The distributions of quantities (i)-(iv) as function of $\log_{10} E_{\mu}$ for events that fulfill the containment selection are illustrated in Figure 5.11. All quantities show a strong dependence on the muon energy which justifies their choice as input variables for the neural network training. The distributions of the corresponding quantities for the events that do not fulfill the requirements mentioned above and therefore the muon energy is not expected to be reliably determined are displayed in Figure 5.12. Only a weak dependence on the muon energy is exhibited indicating that only a lower limit of the muon energy can be calculated.

5. ENERGY RECONSTRUCTION WITH NEURAL NETWORKS (ERENN)



(a) The N_{OMs} per unit length (multiplied by 360 to prevent from having many decimals) with respect to $\log_{10} E_{\mu}$. (b) The $\log_{10} N_{PMTs \text{ with pulses}}$ with respect to $\log_{10} E_{\mu}$.



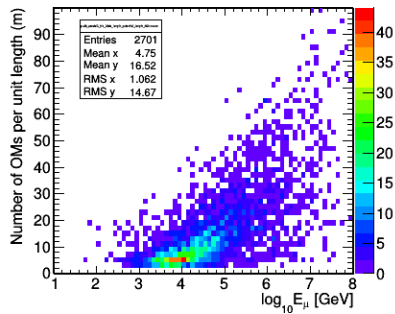
(c) The ratio $\frac{\log_{10} N_{PMTs \text{ with pulses}}}{\log_{10} N_{PMTs \text{ without pulses}}}$ with respect to $\log_{10} E_{\mu}$. (d) The $\log_{10} \text{ToT}$ (Total Time over Threshold) with respect to $\log_{10} E_{\mu}$.

Figure 5.11: The correlation of the input variables for the neural network to the muon energy for events that satisfy the containment selection is shown.

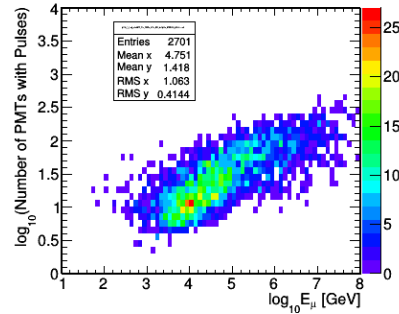
5.5 Training the Neural Network

The input variables described in section 5.4 are inserted to the Neural Network, which is trained and tested in order to achieve the best network performance. Half the event sample is used for NN training and testing while the other half is used for the evaluation of NN and the energy reconstruction. From the first half of the event sample, 70% of the events are used for the NN training and the rest (30%) for testing the NN performance in order to check the NN convergence of the mean square estimator during the different epochs and the deviation of the reconstructed from the simulated muon energy.

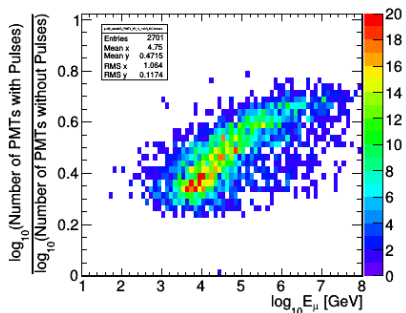
The deviation of the estimated $\log_{10} E_{\mu}$ from the MC $\log_{10} E_{\mu}$ as a function of MC $\log_{10} E_{\mu}$ during the NN training and test phase is shown in Figure 5.13 (a) and (b), respectively. The convergence of the mean square estimator for the



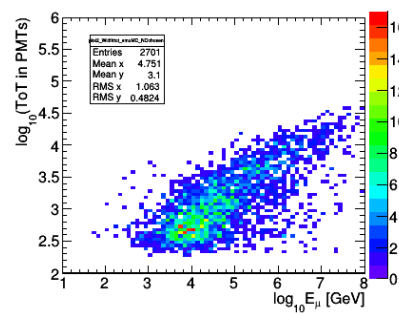
(a) The N_{OMs} per unit length (multiplied by 360 to prevent from having many decimals) with respect to $\log_{10} E_\mu$.



(b) The $\log_{10} N_{PMTs \text{ with pulses}}$ with respect to $\log_{10} E_\mu$.



(c) The ratio $\frac{\log_{10} N_{PMTs \text{ with pulses}}}{\log_{10} N_{PMTs \text{ without pulses}}}$ with respect to $\log_{10} E_\mu$.

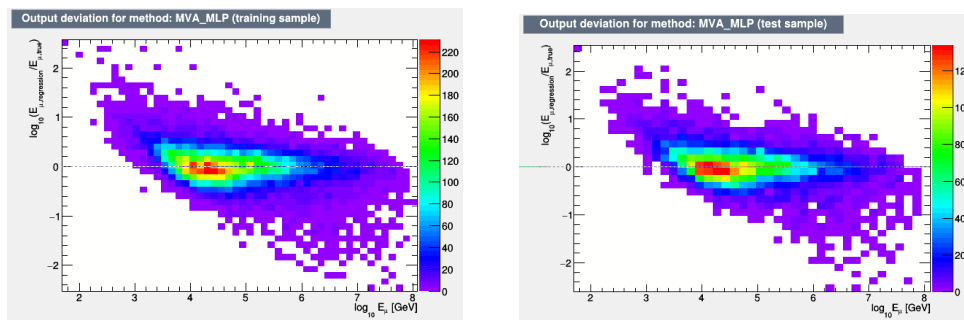


(d) The $\log_{10} \text{Tot}$ (Total Time over Threshold) with respect to $\log_{10} E_\mu$.

Figure 5.12: The correlation of the input variables for the neural network to the muon energy for events that fail the containment selection is shown.

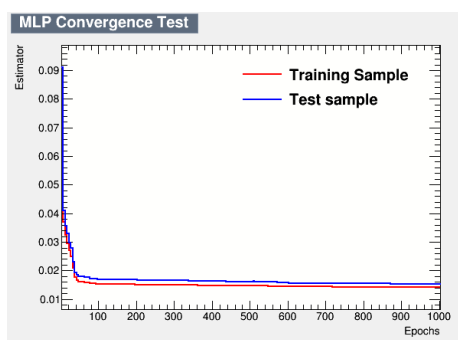
the NN training and test phase during the different epochs of training is shown in Figure 5.13(c). The epochs of NN training refer to the number of iterations performed over the data set in order to train the NN. The average deviation of the estimated $\log_{10} E_\mu$ from the MC $\log_{10} E_\mu$ during the NN training (open squares) and test (filled squares) phase is shown in Figure 5.13(d) (blue squares). The average deviation for 90% of the events, for which the deviation of the estimated $\log_{10} E_\mu$ from the MC $\log_{10} E_\mu$ is closer to the average deviation during the NN training (open squares) and test (filled squares) phase, is calculated and is shown in Figure 5.13(d) (black squares). For the muon energy estimation an average deviation $\simeq 0.23$ is achieved for both training and test samples for 90% of the events (black squares). It can be concluded that the NN has a stable performance for this energy estimator and it can be applied to a different event sample for evaluation.

5. ENERGY RECONSTRUCTION WITH NEURAL NETWORKS (ERENN)

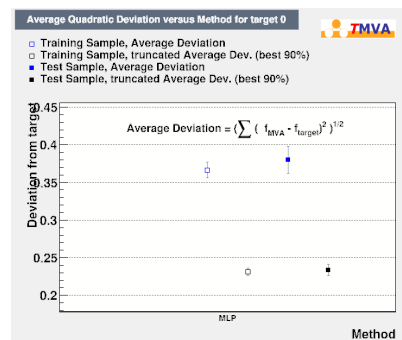


(a) The deviation $\log_{10} E_{\mu,estimated} - \log_{10} E_{\mu,true}$ with respect to $\log_{10} E_{\mu}$ during the NN training phase.

(b) The deviation $\log_{10} E_{\mu,estimated} - \log_{10} E_{\mu,true}$ with respect to $\log_{10} E_{\mu}$ during the NN test phase.



(c) The convergence of the mean square estimator of the training and test sample through the epochs.



(d) The average deviation of the estimated $\log_{10} E_{\mu}$ from the MC $\log_{10} E_{\mu}$ for the training and test sample.

Figure 5.13: The performance of the Neural Network for the muon energy is shown.

5.6 Performance of the Energy Reconstruction

Once the weights of the inter-neuron connections of the NN have been produced, a different sample of ν_{μ} events is used for the evaluation of the Neural Network and for the estimation of muon and neutrino energy. The input variables are created for this new sample and they are inserted in the NN which returns the reconstructed energy.

The relation between the estimated and the MC energy for events that satisfy the containment selection (described in section 5.2) and for all reconstructed tracks is presented in Figure 5.14. An overestimation of the muon energy for $E_{\mu} < 6$ TeV can be observed which decreases as the energy increases resulting to a linear correlation for $E_{\mu} \geq 10$ TeV. This overestimation is expected as ionization dominates for muons at the GeV range and these low energy muons

that travel long distances inside the detector produce comparable amount of hits to that of muons at the TeV range that travel shorter distances. In addition, muons with energies lower than 6 TeV that pass the selection criteria are more likely to have been created inside or in the neighborhood of the detector leaving photons from the hadronic part inside the instrumented volume, leading to an overestimation of their energy. This effect is absent at higher energies where stochastic losses take place.

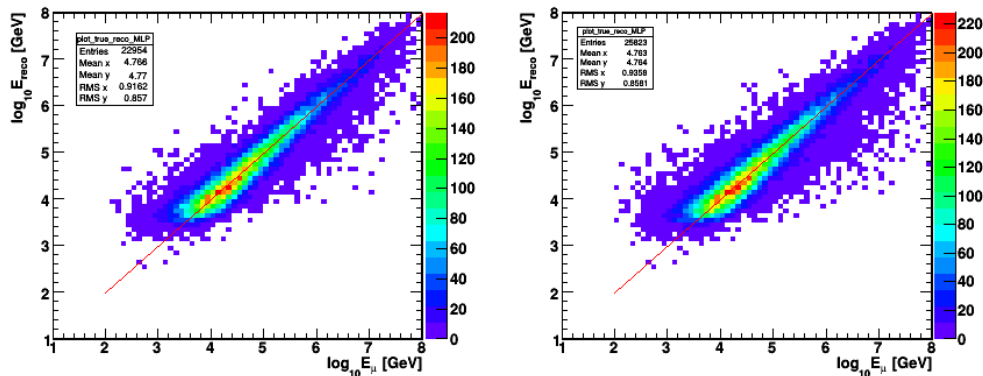


Figure 5.14: The reconstructed energy ($\log_{10}E_{reco}$) with respect to the MC muon energy ($\log_{10}E_{\mu}$) for events that satisfy the containment selection (left plot) and for all reconstructed events (right plot).

As a measure of the quality of this energy estimator, the median of $\log_{10}(E_{reco}/E_{\mu})$ is used, where E_{reco} is the reconstructed energy and E_{μ} is the MC muon energy. This median with 68% and 90% quantiles is reported in Figure 5.15 with respect to the logarithm of the MC muon energy for events that satisfy the containment selection (left plot) and for all reconstructed tracks (right plot). An overestimation can be observed for muons with energy $E_{\mu} < 6$ TeV while the median of $\log_{10}(E_{reco}/E_{\mu})$ gets close to zero for events with higher muon energies ($E_{\mu} \geq 10$ TeV) which is the energy regime we are mostly interested in for a diffuse flux observation. The median reaches $\simeq 0.05$ for muons with $E_{\mu} \geq 10$ TeV while for muon energies $E_{\mu} > 1$ PeV the calculation suffers from limited statistics. However, an underestimation of the muon energy can be observed for muons at the PeV energy range (right plot in Figure 5.15). These highly energetic muons have deposited light in the instrumented volume and their track direction can be reliably reconstructed, but at these energies, muons are expected to travel

5. ENERGY RECONSTRUCTION WITH NEURAL NETWORKS (ERENN)

several kilometers, therefore the tracks escape the detector, allowing only a lower limit estimate of the muon energy.

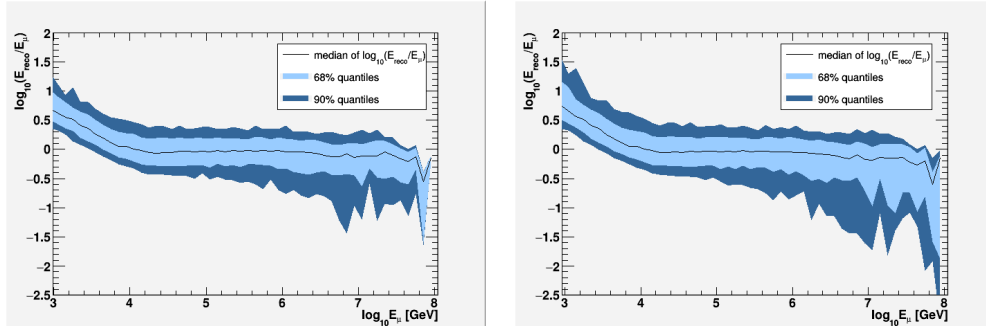


Figure 5.15: The median of $\log_{10}(E_{reco}/E_{\mu})$ (with 68% and 90% quantiles) with respect to the MC muon energy ($\log_{10}E_{\mu}$) for events that satisfy the containment selection (left plot) and for all reconstructed events (right plot).

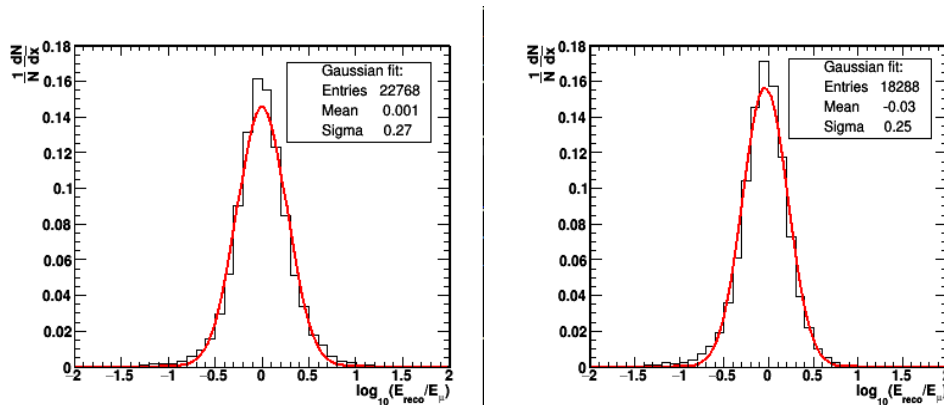


Figure 5.16: The distribution of $\log_{10}(E_{reco}/E_{\mu})$ for events that satisfy the containment selection with $E_{\mu} \geq 1$ TeV (left plot) and events with $E_{\mu} \geq 10$ TeV (right plot). The y axis corresponds to $\frac{1}{N} \frac{dN}{dx}$ where $x = \log_{10}(E_{reco}/E_{\mu})$. A Gaussian fit is applied.

Figure 5.16 shows the distribution of $\log_{10}(E_{reco}/E_{\mu})$ for events that satisfy the containment selection. The left plot shows the distribution for muons with $E_{\mu} \geq 1$ TeV while the right plot shows the distribution for muons with $E_{\mu} \geq 10$ TeV. A Gaussian fit is applied to estimate the energy resolution. The energy resolution is 0.27 for muons with $E_{\mu} \geq 1$ TeV and reduces to 0.25 for muons with $E_{\mu} \geq 10$ TeV. The larger energy resolution for muons with energies above 1 TeV is due to the overestimation of energy for $1 \text{ TeV} < E_{\mu} < 10 \text{ TeV}$, that is apparent in Figure 5.15. The energy resolution of this energy estimator is also determined for all reconstructed events and the dN corresponding distributions are shown in

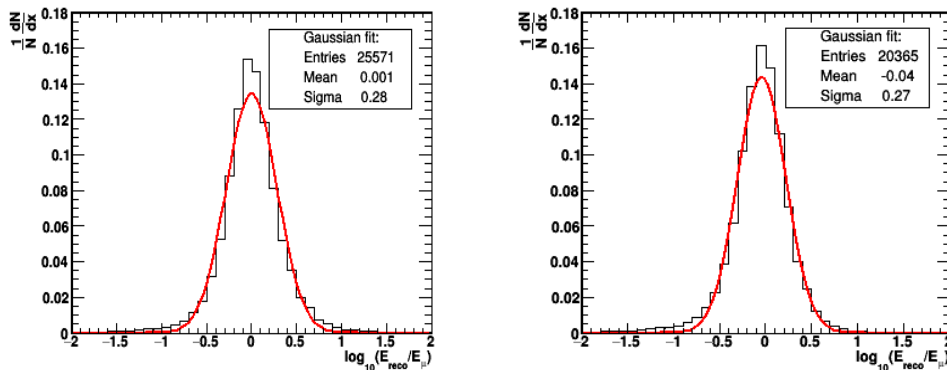


Figure 5.17: The distribution of $\log_{10}(E_{reco}/E_{\mu})$ for all reconstructed events with $E_{\mu} \geq 1$ TeV (left plot) and events with $E_{\mu} \geq 10$ TeV (right plot). The y axis corresponds to $\frac{1}{N} \frac{dN}{dx}$ where $x = \log_{10}(E_{reco}/E_{\mu})$. A Gaussian fit is applied.

Figure 5.17. The distributions are more broad compared to the corresponding distributions in Figure 5.16 as the energy is underestimated for events that fail to satisfy the containment selection resulting to an energy resolution of 0.28 and 0.27 for muons with $E_{\mu} \geq 1$ TeV and $E_{\mu} \geq 10$ TeV, respectively.

5.7 Efficiency of the Energy Reconstruction

The efficiency of this energy estimator is investigated for all muon tracks that cross the detector (as described in section 5.2) and have survived from the selection criteria (i), (ii) and (iii) that are described in section 4.3 and are used to select events for which the track direction has been reliably reconstructed (well reconstructed tracks). The efficiency is defined as the ratio:

$$Efficiency = \frac{Number\ of\ events\ that\ pass\ the\ containment\ selection}{Number\ of\ events\ that\ pass\ the\ reconstruction\ selection}$$

The efficiency as a function of $\log_{10} E_{\mu}$ is shown in Figure 5.18 and represents the percentage of events for which the energy is reliably reconstructed. An efficiency of $\simeq 89\%$ can be established that reaches $\simeq 91\%$ for muons with $E_{\mu} \geq 30$ TeV, while for muons with energy at the PeV region the calculation suffers from limited statistics. However, a decrease of efficiency can be observed since high energy muons (with energy at the PeV range) pass the reconstruction selection even if they only have a short path in the instrumented volume (close to the borders of the detector), but they deposit only a small fraction of the light inside the instrumented volume and the energy cannot be reliably reconstructed.

5. ENERGY RECONSTRUCTION WITH NEURAL NETWORKS (ERENN)

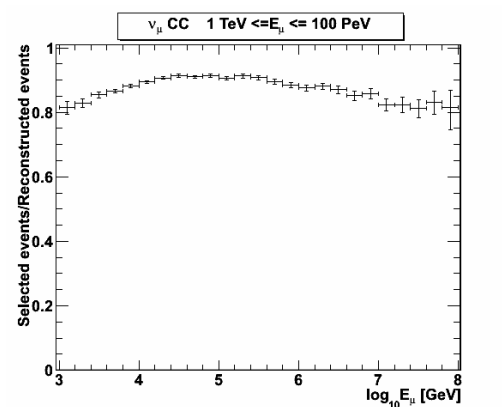
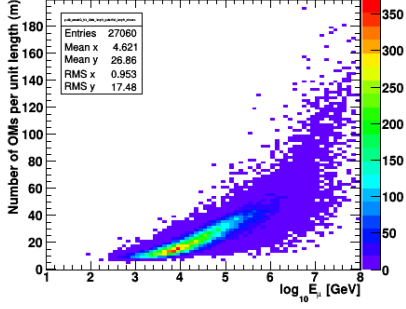


Figure 5.18: The efficiency of the energy reconstruction for events selected from the direction reconstruction is shown as a function of $\log_{10} E_{\mu}$.

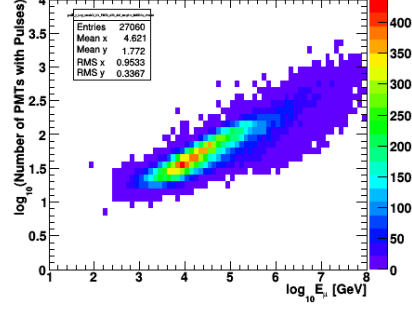
5.8 Estimating the Energy for Reconstructed Events with the recoLNS Track Reconstruction Algorithm

The simulated events pass through a track reconstruction before an attempt to estimate their energy is made. In order to establish that the energy reconstruction can also be applied to other reconstruction methods and that it does not depend on the specific algorithm used for the track fit, we estimated the energy for an event sample for which the track direction had been reconstructed with a different reconstruction package. The reconstruction algorithm, *recoLNS*, employs a probability density function and the hit selection is different compared to the hit selection performed in the *Chameleon* reconstruction package (as described in section 4.5). This difference in the hit selection results in different distributions of the NN input variables and the Neural Network has to be re-trained. The events that are inserted to the NN are well reconstructed tracks with *recoLNS* algorithm ($\Lambda > -5.8$ where Λ is the maximum log-likelihood value per degree of freedom found by the fit) satisfying the containment selection. The containment selection has been modified for this reconstruction algorithm as a larger amount of hits coming from ^{40}K survive the hit selection resulting to larger values of χ_{nDoF}^2 . The muon and the neutrino energy are determined for well contained tracks (as described in section 5.2) satisfying the selection criteria (i), (ii) and (iii) (described in section 4.3). The selection criteria (i), (ii) and (iii)

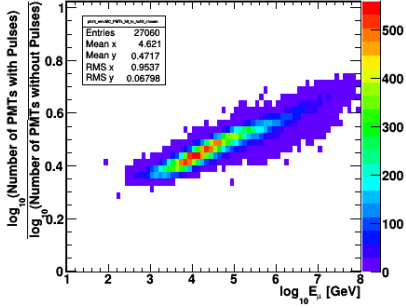
5.8 Estimating the Energy for Reconstructed Events with the recoLNS Track Reconstruction Algorithm



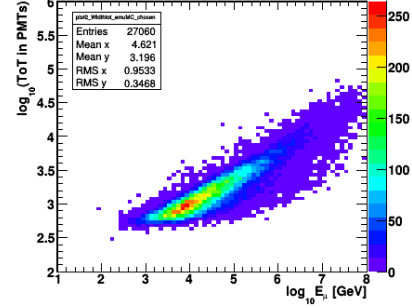
(a) The N_{OMs} per unit length (multiplied by 360 to prevent from having many decimals) with respect to E_μ .



(b) The $\log_{10} N_{PMTs \text{ with pulses}}$ with respect to E_μ .



(c) The ratio $\frac{\log_{10} N_{PMTs \text{ with pulses}}}{\log_{10} N_{PMTs \text{ with no hits}}}$ with respect to E_μ .



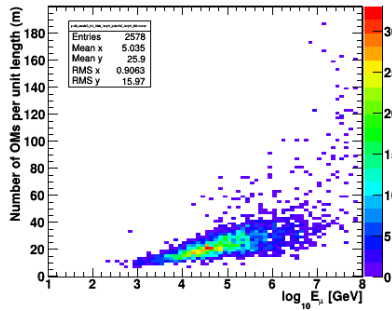
(d) The $\log_{10} \text{ToT}$ (Total Time over Threshold) with respect to E_μ .

Figure 5.19: The correlation of the input variables for the neural network to the muon energy for events that satisfy the containment selection is shown.

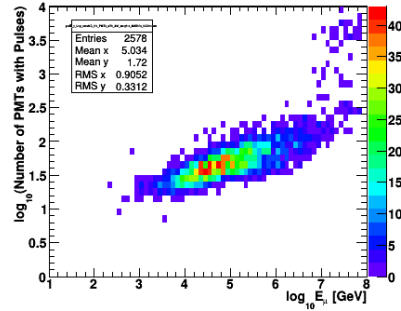
are required in order to discriminate events that have deposited light from the hadronic shower and escape the detector from events that deposit light across the muon path and travel longer distances inside the instrumented volume. The containment selection has been modified to allow for a looser cut on χ_{nDoF}^2 . The energy is reliably reconstructed for events that satisfy the containment selection, otherwise a lower limit for the energy is reported.

Figures 5.19 show the distributions of quantities (i)-(iv) (that are described in section 5.4) as function of E_μ for events satisfying the containment selection. These quantities show a strong dependence on the muon energy and can be used as input variables for the neural network training. The distributions of the corresponding quantities for events failing to satisfy the requirements, mentioned in section 5.2, and therefore the muon energy cannot be reliably determined, are shown in Figure 5.20. In this figure, an excess of hits for muons with $E_\mu > 10$

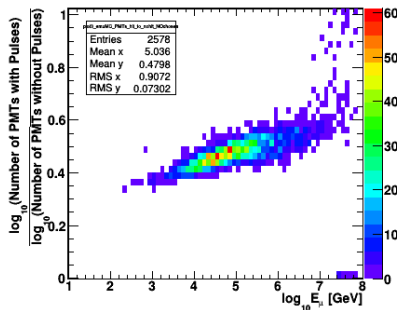
5. ENERGY RECONSTRUCTION WITH NEURAL NETWORKS (ERENN)



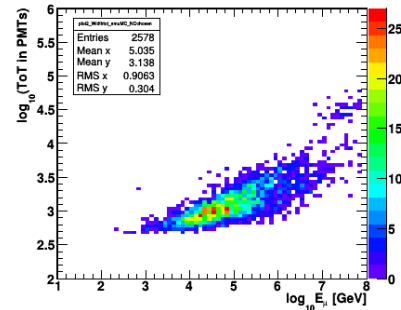
(a) The N_{OMs} per unit length (multiplied by 360 to prevent from having many decimals) with respect to $\log_{10} E_\mu$.



(b) The $\log_{10} N_{PMTs\ with\ pulses}$ with respect to $\log_{10} E_\mu$.



(c) The ratio $\frac{\log_{10} N_{PMTs\ with\ pulses}}{\log_{10} N_{PMTs\ with\ no\ hits}}$ with respect to $\log_{10} E_\mu$.



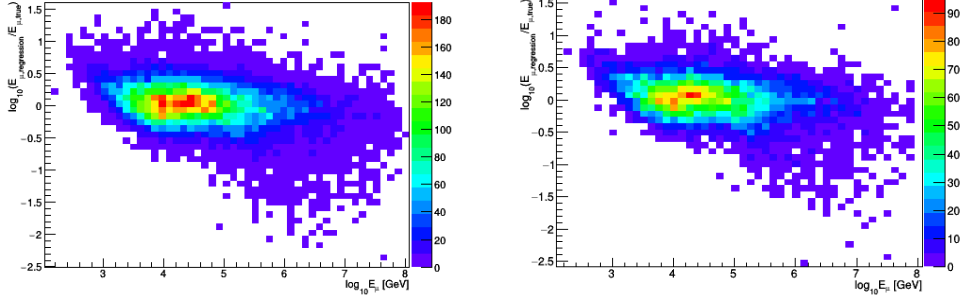
(d) The \log_{10} ToT (Total Time over Threshold) with respect to $\log_{10} E_\mu$.

Figure 5.20: The correlation of the input variables for the neural network to the muon energy for events that fail the containment selection is shown.

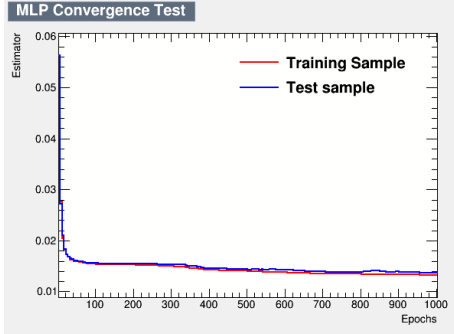
PeV can be observed. These hits come mostly from ^{40}K decays in distant PMTs and survive the hit selection leading to large values of $\log_{10} N_{PMTs\ with\ pulses}$ as it is shown in Figure 5.20 (b). These quantities are inserted to the Neural Network which, as for the *Chameleon* reconstruction, is trained and tested with half the event sample. The other half is used for the energy reconstruction.

Figures 5.21 (a)-(d) show the results of the training and test phase of the NN. The deviation of the estimated $\log_{10} E_\mu$ from the MC $\log_{10} E_\mu$ as a function of MC $\log_{10} E_\mu$ during the NN training and test phase is shown in Figure 5.21 (a) and (b). Figure 5.21(c) shows the convergence of the mean square estimator for the the NN training and test phase during the different epochs of NN training. The average deviation of the estimated $\log_{10} E_\mu$ from the MC $\log_{10} E_\mu$ during the NN training (open squares) and test (filled squares) phase is shown in Figure 5.21(d) (blue squares). The average deviation for 90% of the events for which

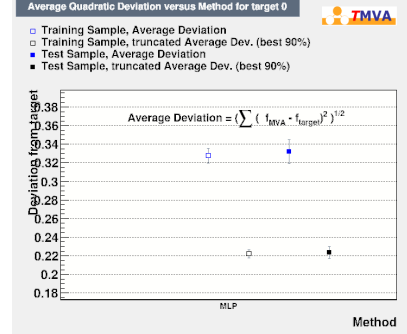
5.8 Estimating the Energy for Reconstructed Events with the recoLNS Track Reconstruction Algorithm



(a) The deviation $\log_{10} E_{\mu,estimated} - \log_{10} E_{\mu,true}$ with respect to $\log_{10} E_{\mu}$ during the NN training phase. (b) The deviation $\log_{10} E_{\mu,estimated} - \log_{10} E_{\mu,true}$ with respect to $\log_{10} E_{\mu}$ during the NN test phase.



(c) The convergence of the mean square estimator of the training and test sample through the epochs.



(d) The average deviation of the estimated $\log_{10} E_{\mu}$ from the MC $\log_{10} E_{\mu}$ for the training and test sample.

Figure 5.21: The performance of the Neural Network for the muon energy is shown.

the deviation of the estimated $\log_{10} E_{\mu}$ from the MC $\log_{10} E_{\mu}$ is closer to the the average deviation during the NN training (open squares) and test (filled squares) phase is calculated and is shown in Figure 5.21(d) (black squares). For the muon energy estimation an average deviation $\simeq 0.22$ is achieved for both training and test samples. The energy can be evaluated for a different event sample since the NN has a stable performance for this energy estimator.

5.8.1 Performance of the Energy Reconstruction

The results of the muon and neutrino energy reconstruction for events that have been reconstructed with the *recoLNS* direction reconstruction are reported in this section. The relation between the estimated and the MC energy for events that satisfy the containment selection (described above) and for all reconstructed

5. ENERGY RECONSTRUCTION WITH NEURAL NETWORKS (ERENN)

tracks is presented in Figure 5.22. A linear correlation can be observed for events with $E_\mu \geq 6$ TeV.

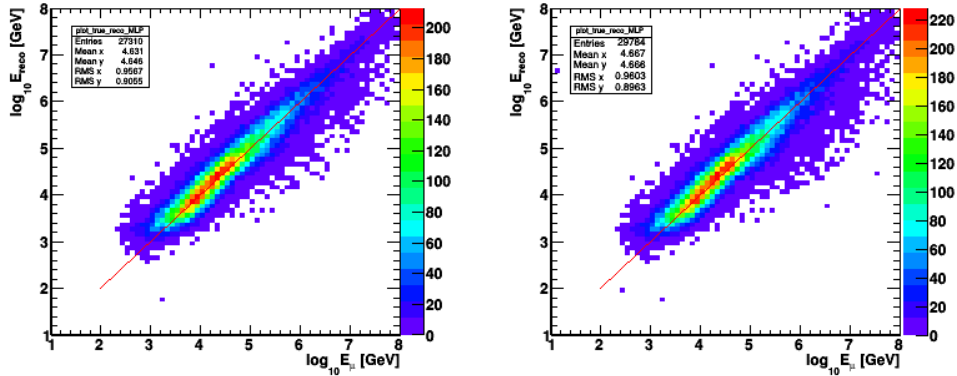


Figure 5.22: The reconstructed energy ($\log_{10} E_{reco}$) with respect to MC muon energy ($\log_{10} E_\mu$) for events that satisfy the containment selection (left plot) and for all reconstructed events (right plot).

Figure 5.23 shows the median of $\log_{10}(E_{reco}/E_\mu)$ with 68% and 90% quantiles, where E_{reco} is the reconstructed energy and E_μ is the MC muon energy, with respect to the logarithm of the MC muon energy for events that satisfy the containment selection (left plot) and for all reconstructed tracks (right plot). An overestimation of the muon energy for $E_\mu < 6$ TeV due to the detection of photons from the hadronic shower can be observed which decreases as the energy increases resulting to a median of 0.02 for $E_\mu \geq 10$ TeV. Although the calculation suffers from limited statistics, an underestimation of the muon energy can be observed for muons at the PeV energy range (right plot in Figure 5.23) since muons have deposited light in the instrumented volume and the track direction of these highly energetic muons can be reliably reconstructed but the tracks escape the detector thus allowing only a lower limit estimate of the muon energy. To facilitate comparisons, Figure 5.24 shows the median of $\log_{10}(E_{reco}/E_\mu)$ with 68% and 90% quantiles, with respect to the MC muon energy for events that satisfy the containment selection (left plot) and for all reconstructed tracks (right plot) for muons with high energies ($E_\mu \geq 10$ TeV) which is the energy range we are mostly interested in for a diffuse flux analysis.

Figure 5.25 shows the distribution of $\log_{10}(E_{reco}/E_\mu)$ for events that satisfy the containment selection. The left plot shows the distribution for muons with $E_\mu \geq 1$ TeV while the right plot shows the distribution for muons with

5.8 Estimating the Energy for Reconstructed Events with the recoLNS Track Reconstruction Algorithm

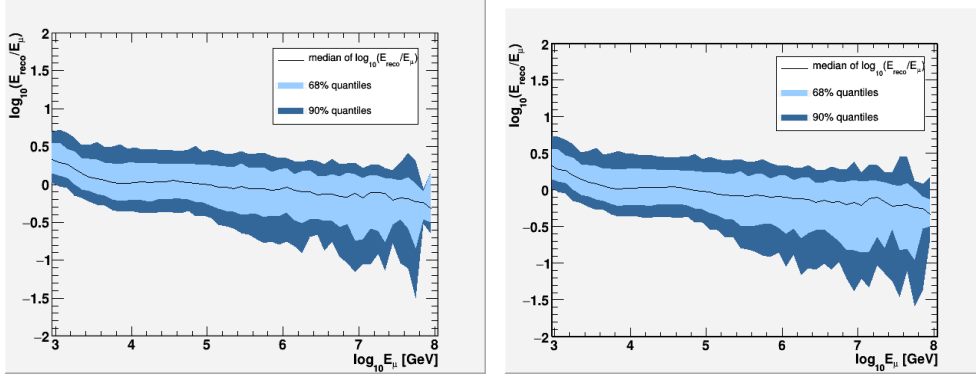


Figure 5.23: The median of $\log_{10}(E_{reco}/E_{\mu})$ (with 68% and 90% quantiles) with respect to the MC muon energy ($\log_{10}E_{\mu}$) for events that satisfy the containment selection (left plot) and for all reconstructed events (right plot).

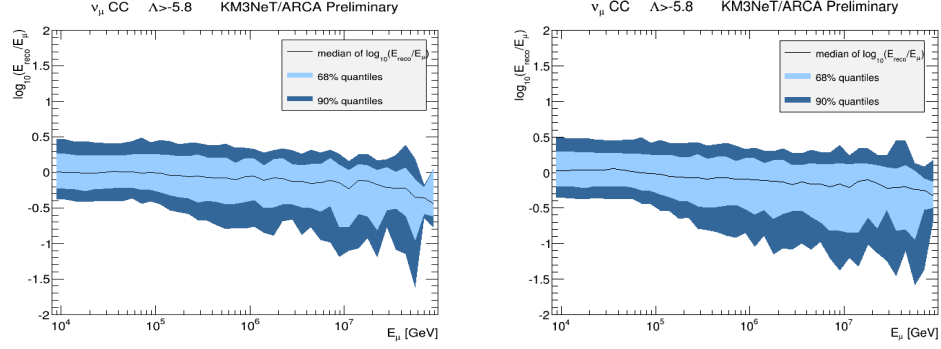


Figure 5.24: The median of $\log_{10}(E_{reco}/E_{\mu})$ (with 68% and 90% quantiles) with respect to the MC muon energy ($\log_{10}E_{\mu}$) for events that satisfy the containment selection (left plot) and for all reconstructed events (right plot).

$E_{\mu} \geq 10$ TeV. A Gaussian fit is applied to estimate the energy resolution. The energy resolution is 0.27 for both energy intervals, while an offset of the mean of the distribution of 0.02 for muons with energies above 1 TeV is due to the overestimation of muon energy for $1 \text{ TeV} < E_{\mu} < 10 \text{ TeV}$, that is apparent in Figure 5.23. The energy resolution of this energy estimator is determined for all reconstructed events and the corresponding distributions are shown in Figure 5.26. The distributions are slightly broader and have larger tails in the left part compared to the corresponding distributions in Figure 5.25 as the energy is underestimated for events that fail to satisfy the containment selection resulting to an energy resolution of 0.28 both for muons with $E_{\mu} \geq 1 \text{ TeV}$ and $E_{\mu} \geq 10 \text{ TeV}$.

5. ENERGY RECONSTRUCTION WITH NEURAL NETWORKS (ERENN)

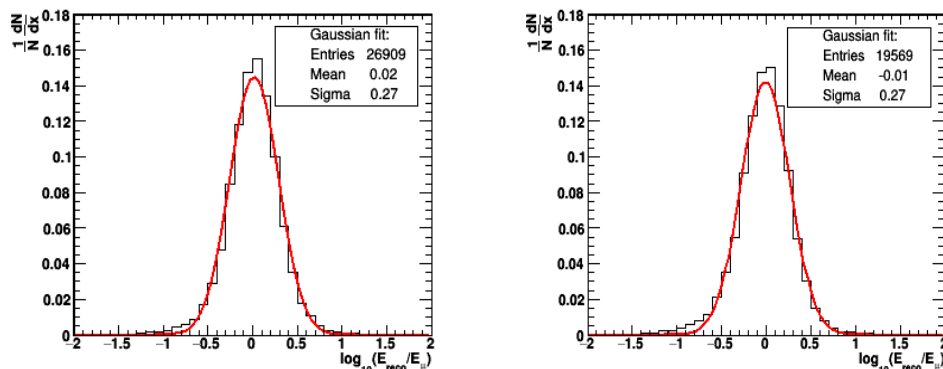


Figure 5.25: The distribution of $\log_{10}(E_{reco}/E_{\mu})$ for events that satisfy the containment selection with $E_{\mu} \geq 1$ TeV (left plot) and events with $E_{\mu} \geq 10$ TeV (right plot). The y axis corresponds to $\frac{1}{N} \frac{dN}{dx}$ where $x = \log_{10}(E_{reco}/E_{\mu})$. A Gaussian fit is applied.

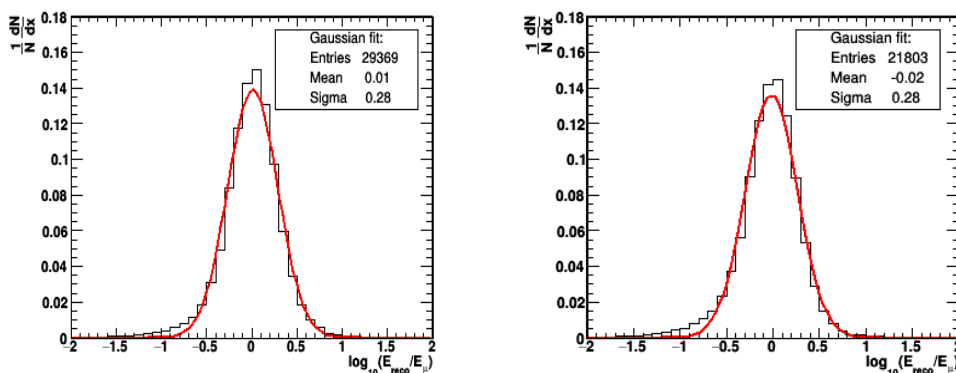


Figure 5.26: The distribution of $\log_{10}(E_{reco}/E_{\mu})$ for all reconstructed events with $E_{\mu} \geq 1$ TeV (left plot) and events with $E_{\mu} \geq 10$ TeV (right plot). The y axis corresponds to $\frac{1}{N} \frac{dN}{dx}$ where $x = \log_{10}(E_{reco}/E_{\mu})$. A Gaussian fit is applied.

5.8.2 Contribution of Background in the Energy Estimation

The contribution of hits coming from background sources, and specifically decays of radioactive ^{40}K , in the energy reconstruction is studied in this section. The ratio of hits coming from the muon passage through sea water to hits coming from ^{40}K decays with respect to the MC muon energy for events reconstructed with *recoLNS* that satisfy the containment selection is shown in Figure 5.27. In order to study the effect of the contribution of noise hits to the muon energy reconstruction for events for which the energy can be reliably reconstructed, the median of $\log_{10}(E_{reco}/E_{\mu})$ with 68% and 90% quantiles, with respect to the

5.8 Estimating the Energy for Reconstructed Events with the recoLNS Track Reconstruction Algorithm

MC muon energy for events that satisfy the containment selection is shown in Figure 5.28. It can be observed (Figure 5.27) that if the ratio of the number of the reconstructed hits coming from the muon passage through sea water to the number of reconstructed noise hits is less than 2.5, the energy is overestimated (Figure 5.28). The effect of the contribution of noise hits to the hits selected by the track fit is more significant for events that have hit fewer PMTs. This leads to an overestimation of the energy which is apparent in the energy bins that contain a small amount of hits. Specifically for $E_\mu \simeq 45$ PeV, where there are events for which the fraction of noise hits is $\simeq 33\%$ of the total reconstructed hits (corresponding to a ratio of $\simeq 2$ in y axis of Figure 5.27) we have an overestimation of the muon energy of about 30% which can also be observed in Figure 5.28. In the lower energy regime, for muons with $E_\mu < 10$ TeV, this effect is less evident as the detection of photons from the hadronic shower is the main effect that results to the overestimation of the muon energy so the contribution of noise hits to this overestimation can only be observed in event by event base.

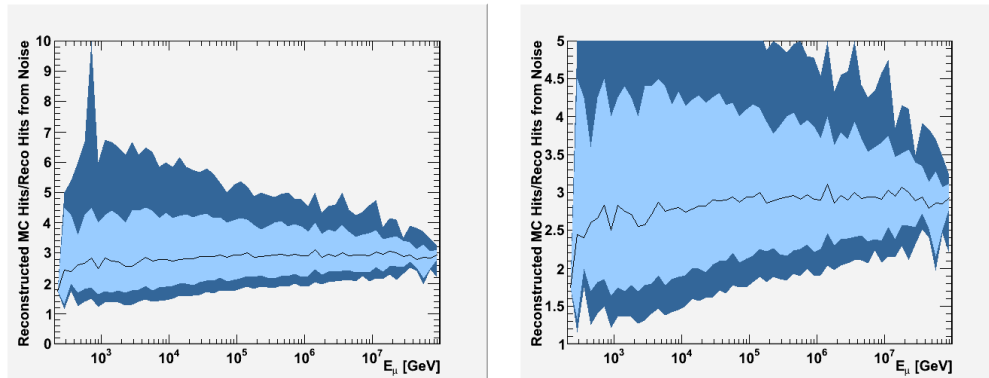


Figure 5.27: The ratio of reconstructed hits coming from the muon passage through sea water to reconstructed hits coming from ^{40}K decays with respect to the MC muon energy for events that satisfy the containment selection. The right plot is a zoom of this ratio.

5. ENERGY RECONSTRUCTION WITH NEURAL NETWORKS (ERENN)

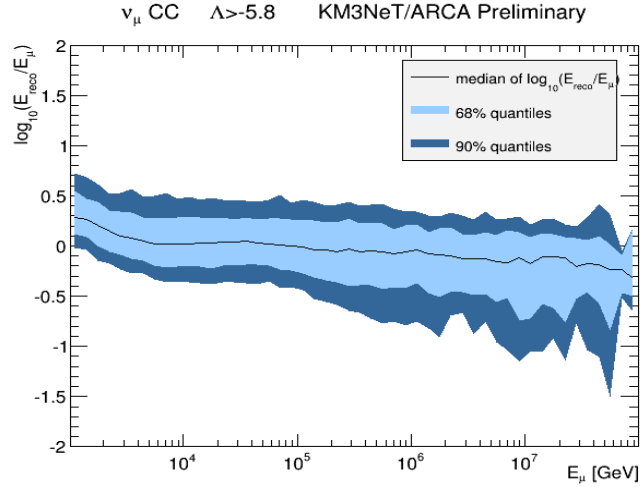


Figure 5.28: The median of $\log_{10}(E_{reco}/E_{\mu})$ (with 68% and 90% quantiles) with respect to MC muon energy ($\log_{10}E_{\mu}$) for events that satisfy the containment selection.

5.8.3 Efficiency of the Energy Reconstruction

The efficiency of this energy estimator for the *recoLNS* reconstruction is investigated for all muons that cross the detector (as described in section 5.2) and have survived the $\Lambda > -5.8$ criterion. The efficiency is defined as the ratio:

$$Efficiency = \frac{Number\ of\ events\ that\ pass\ the\ containment\ selection}{Number\ of\ events\ with\ \Lambda > -5.8\ that\ cross\ the\ detector}$$

Figure 5.29 shows the *efficiency* as a function of E_{μ} representing the percentage of events for which the energy is reliably reconstructed. A very high efficiency of $\simeq 99.5\%$ can be established for the tracks that cross the detector volume while the efficiency decreases for muons with energy at the PeV region. These muons are expected to travel distances much larger than the instrumented volume, but have a short path in the detector (close to the detector borders) so only a fraction of the light can be detected and do not satisfy the containment selection. In these high energies the calculation suffers from limited statistics.

The efficiency of the energy reconstruction is also investigated for all reconstructed muons with $\Lambda > -5.8$ and it is reported in Figure 5.30. The efficiency is then defined as the ratio:

$$Efficiency = \frac{Number\ of\ events\ that\ pass\ the\ containment\ selection}{Number\ of\ events\ with\ \Lambda > -5.8}$$

5.8 Estimating the Energy for Reconstructed Events with the recoLNS Track Reconstruction Algorithm

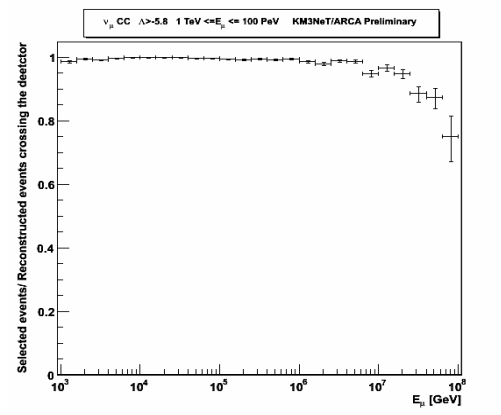


Figure 5.29: The efficiency of the energy reconstruction for events selected from the track direction reconstruction that cross the detector as a function of E_μ .

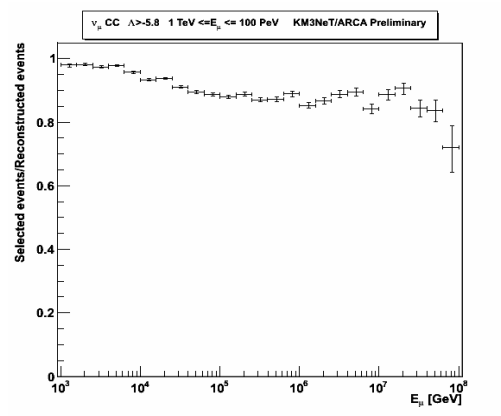


Figure 5.30: The efficiency of the energy reconstruction for all events selected from the track direction reconstruction as a function of E_μ .

An efficiency of approximately 90% is achieved for the whole energy range while for muons with energies $E_\mu > 10$ PeV the efficiency decreases since muons of that high energy are reconstructed reliably even if they have a short path in the detector but they deposit a small fraction of the light inside the instrumented volume and their energy cannot be reliably reconstructed.

5.8.4 Systematic Uncertainties

The simulations of the optical properties in sea water take into account the standard optical properties as measured by G. Riccobene et al at Capo Passero [81]. However, both the scattering and the absorption length have uncertainties of the order of $\pm 10\%$. The uncertainty on the scattering length is expected to be due to contribution of particulates in sea water as the scattering in pure sea water is well established. This uncertainty is modeled by varying the particulate contribution from 0.0075 ppm to 0.0085 ppm (leading to more scattering and lower scattering length) and 0.00665 (less scattering, higher scattering length) in the 'particulate' model as described in [111]. This variation results to the observed $\pm 10\%$ uncertainty in the total scattering probability over the 400-500 nm range, for which the water transparency and the efficiency of the PMTs are maximal and thus this is the range of the wavelength that most Cherenkov photons will be detected. The absorption length was also varied by a uniform $\pm 10\%$ over the full wavelength range.

The ANTARES experiment has reported a reduction of the PMT effective area up to 11% when the simulations with GEANT4 were used to predict the two-fold ^{40}K coincidence rate taken into account that the PMT efficiency (probability of a liberated photoelectron to produce a PMT signal) is 90%¹. In addition, the measurements in different PMTs (large PMTs used in ANTARES) have resulted to variations of 10%. The uncertainty in the PMT effective area of 10% is an overestimation when referring to the small PMTs (3 inches diameter) that are used in KM3NeT for which the PMT efficiency is expected to be 90%. However, an uncertainty of 10% has been modeled in order to observe a noticeable effect in the simulations.

The systematic uncertainties of 10% on scattering length, absorption length and on the effective area of the PMTs have been considered and the effects of these uncertainties to the energy reconstruction are reported in Table 5.1. The distributions of $\log_{10}(E_{reco}/E_{\mu})$ for muons with $E_{\mu} \geq 10$ TeV that satisfy the containment selection have been produced and a Gaussian fit has been applied in order to calculate the energy resolution. The mean value of these distributions as it is deduced by the Gaussian fit is reported as well. The first row of this table corresponds to the values that have been calculated by the standard simulation

¹an efficiency of $\simeq 80\%$ seems to better match the data

5.8 Estimating the Energy for Reconstructed Events with the recoLNS Track Reconstruction Algorithm

$\nu_\mu CC$ $10 \text{ TeV} \leq E_\mu \leq 100 \text{ PeV}$ *KM3NeT / ARCA Preliminary*

Energy Resolution

$\Lambda > 5.8$	Gaussian fit: Mean (%)	Gaussian fit: σ (%)
Simulation Values:	-1.0%	27%
Absorption Length: -10%	-9.5%	26%
Absorption Length: +10%	5.3%	27%
Scattering Length: -10%	-2.4%	27%
Scattering Length: +10%	-0.8%	27%
PMT Effective Area: -10%	-6.0%	27%
PTM Effective Area: +10%	2.0%	27%

Table 5.1: The systematic errors for events that satisfy the containment selection.

as it is shown in Figure 5.25 (right plot). For this standard simulation, the energy resolution for muons with $E_\mu \geq 10 \text{ TeV}$ is $\simeq 27\%$ while the muon energy is underestimated by $\simeq 1\%$. The systematic uncertainties slightly affect the energy resolution that remains almost constant as it can be observed in Table 5.1. On the other hand an overestimation ($\simeq 5.3\%$) of the muon energy can be reported if the absorption length is increased by 10% while a corresponding decrease of the absorption length results to an energy underestimation of $\simeq 9.5\%$. The corresponding energy underestimation for a 10% increase of the scattering length is $\simeq 0.8\%$ while the muon energy underestimation increases to $\simeq 2.4\%$ if the scattering length is decreased by 10%. Finally, a 10% decrease (increase) in the PMT effective area results to an under(over)estimation of $\simeq 6\%$ ($\simeq 2\%$) of the muon energy.

5.8.5 Neutrino Energy Reconstruction

The neutrino energy cannot be reliably reconstructed for events that either do not cross the detector, or cross the detector but the neutrino interaction vertex lies outside the instrumented volume. In such cases most photons from the hadronic activity are not detected, thus only a lower limit on the neutrino energy can be estimated. This limit corresponds to the reconstructed muon energy. In order to ensure that the muon and neutrino energy are reliably reconstructed

5. ENERGY RECONSTRUCTION WITH NEURAL NETWORKS (ERENN)

for events with the neutrino vertex close or inside the instrumented volume, we consider events with the reconstructed vertex inside a fiducial volume with radius $R = 420$ m and height $h = 540$ m (compared with $R_{detector} = 504$ m and $h_{detector} = 612$ m). The events under consideration have been reconstructed with *recoLNS*, satisfy the $\Lambda > -5.8$ and the containment criterion (as described in section 5.8). The reconstructed vertex has been determined by *recoLNS* [103]. Table 5.2 shows the ratio of events that have interacted inside and outside the detector volume (using the MC vertex) to the number of events with the reconstructed vertex inside a fiducial volume ($N_{In\ Fiducial}$). It can be observed that 65.5% of $N_{In\ Fiducial}$ have interacted outside the detector resulting to an underestimation of the neutrino energy as photons from the hadronic part have a lower probability (depending on the vertex position) to be detected. In order to select events that have interacted inside the instrumented volume and particularly $N_{In\ Fiducial}$ we apply the selection criteria for atmospheric muon rejection that have been established in [112], [113]. This selection keeps most $N_{In\ Fiducial}$ and rejects events with high activity on border strings. Moreover, events with activity upstream of the reconstructed vertex that is compatible with the track hypothesis are examined and rejected if they have given pulses in PMTs at the edge of the detector. The majority (99,5%) of $N_{In\ Fiducial}$ that also satisfy these criteria have interacted inside the detector as it is shown in Table 5.3 and are good candidates for the neutrino energy reconstruction as most photons from the hadronic part will most probably be detected.

$\frac{\text{Events that have interacted inside the detector volume}}{\text{Events that have been reconstructed to interact inside the fiducial volume}}$	34.5%
$\frac{\text{Events that have interacted outside the detector volume}}{\text{Events that have been reconstructed to interact inside the fiducial volume}}$	65.5%

Table 5.2: The ratio of events that have interacted in(out)side the detector volume to the number of events that have been reconstructed to have the vertex inside a fiducial volume.

The results on the muon and neutrino energy reconstruction for events with the reconstructed vertex inside a fiducial volume, $N_{In\ Fiducial}$, that also satisfy the criteria for atmospheric muon rejection are presented in Figure 5.31. The overestimation of the muon energy (left plot) is due to the fact that photons

5.8 Estimating the Energy for Reconstructed Events with the recoLNS Track Reconstruction Algorithm

Events that satisfy the selection criteria for atmospheric muon rejection:

$\frac{\text{Events that have interacted inside the detector volume}}{\text{Events that have been reconstructed to interact inside the fiducial volume}}$	99.5%
$\frac{\text{Events that have interacted outside the detector volume}}{\text{Events that have been reconstructed to interact inside the fiducial volume}}$	0.5%

Table 5.3: The ratio of events that have interacted in(out)side the detector volume to the number of events that have been reconstructed to have the vertex inside a fiducial volume for tracks that satisfy the selection for atmospheric muon rejection.

from the hadronic shower are detected and a fraction of them is attributed to the muon track. A very good linear relation between the reconstructed energy and the neutrino energy can be observed in Figure 5.31 (right plot) leading to a reliable reconstruction of the neutrino energy for tracks that interact well inside the instrumented volume. For events crossing the detector which satisfy the muon containment selection a good linear relation between the reconstructed energy and the muon energy has been achieved as it can be seen in Figure 5.32.

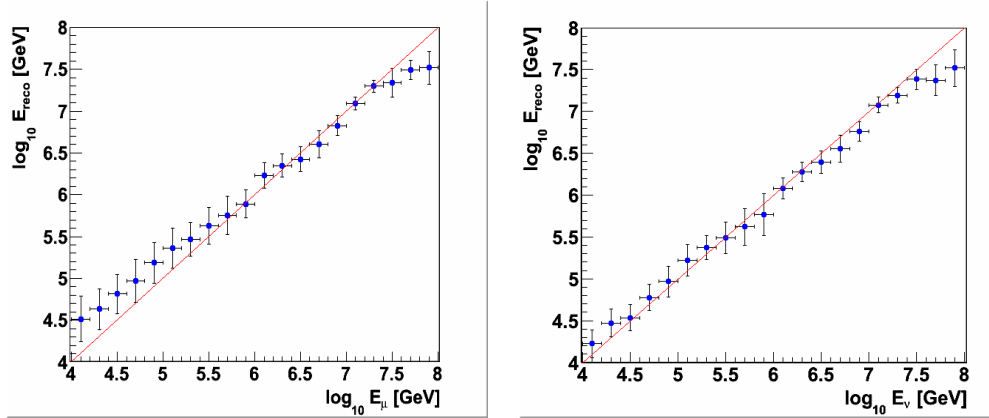


Figure 5.31: Left (Right) plot: The reconstructed energy ($\log_{10} E_{reco}$) with respect to MC muon energy ($\log_{10} E_{\mu}$) (MC neutrino energy, $\log_{10} E_{\nu}$) for events (with $E_{\mu} \geq 10$ TeV) that satisfy the containment selection and the interaction vertex is inside a fiducial volume. The mean with RMS error is shown.

5. ENERGY RECONSTRUCTION WITH NEURAL NETWORKS (ERENN)

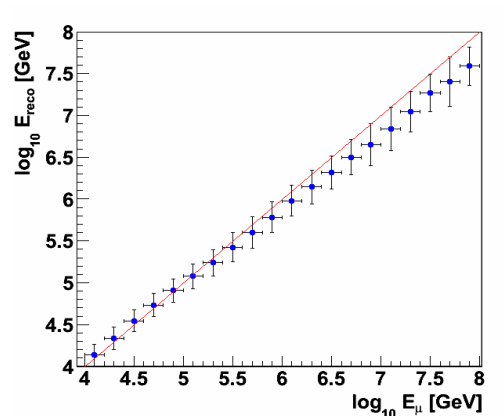


Figure 5.32: The reconstructed energy ($\log_{10} E_{reco}$) with respect to MC muon energy ($\log_{10} E_{\mu}$) for events (with $E_{\mu} \geq 10$ TeV) that satisfy the containment selection. The mean with RMS error is shown.

5.9 Estimating the Energy for an Alternative Detector Configuration

The performance of this energy estimator has been tested for an alternative detector configuration as the final settings for the distance between strings is still under consideration by the KM3NeT Collaboration. The distance between strings in this detector is 120 m compared to the 90 m string distance that was defined for the standard detector layout. The larger distance between strings leads to an 80% increase of the instrumented volume, while the detection ability for high energy neutrinos, which are of interest in these large neutrino telescopes is maintained (Figure 4.13). The track direction for these events is reconstructed once with the *Chameleon* and once using the *recoLNS* reconstruction algorithms separately. Then, the events pass through the containment selection as described in section 5.2 and 5.8 correspondingly, in order to distinguish events for which the energy can be reliably reconstructed from events that pass outside the detection volume and for which a lower limit on the energy is reported. The χ_{nDoF}^2 conditions can be loosened for the *Chameleon* reconstruction, as the efficiency of this algorithm (which is based on a χ^2 minimization) increases for high energy muons crossing the detector since this larger instrumented volume allows for longer track segments. The hit selection criteria for the energy reconstruction can, thus, be loosened as the events that fulfill the containment selection deposit the light in a larger detector volume and are most probably good candidates

5.9 Estimating the Energy for an Alternative Detector Configuration

for a reliable energy reconstruction. The *recoLNS* algorithm does not explicitly depend on the increase of the detector volume and for this bigger volume has a larger contribution of hits coming from ^{40}K decays. Therefore, the selection criteria applied to the 90 m configuration for the distinction of events for which the energy can be reliably reconstructed from events passing outside the detector are maintained. The Neural Network is retrained separately for reconstructed events with the *Chameleon* and *recoLNS*. The results of the energy reconstruction for this detector configuration are shown below.

Figure 5.33 shows the median of $\log_{10}(E_{reco}/E_{\mu})$ as a function of $\log_{10}E_{\mu}$ with 68% and 90% quantiles, where E_{reco} is the reconstructed energy and E_{μ} is the MC muon energy for events that were reconstructed with *Chameleon* and satisfy the containment selection (left plot) and for all reconstructed tracks (right plot). An underestimation of the energy for muons at the PeV energy range is observed in Figure 5.33 (right plot) leading to an energy resolution of 0.27 for all reconstructed tracks (Figure 5.34 right plot) with $E_{\mu} \geq 10$ TeV and 0.26 for tracks that in addition satisfy the containment selection (Figure 5.34 left plot). This energy resolution is comparable with the corresponding energy resolution for the standard detector configuration when the hit selection and the track reconstruction of the *Chameleon* algorithm are used.

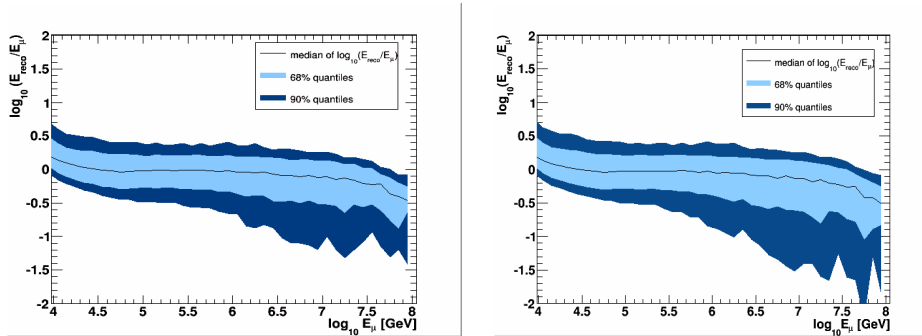


Figure 5.33: The median of $\log_{10}(E_{reco}/E_{\mu})$ (with 68% and 90% quantiles) with respect to MC muon energy ($\log_{10}E_{\mu}$) for events that satisfy the containment selection (left plot) and for all reconstructed events (right plot).

5. ENERGY RECONSTRUCTION WITH NEURAL NETWORKS (ERENN)

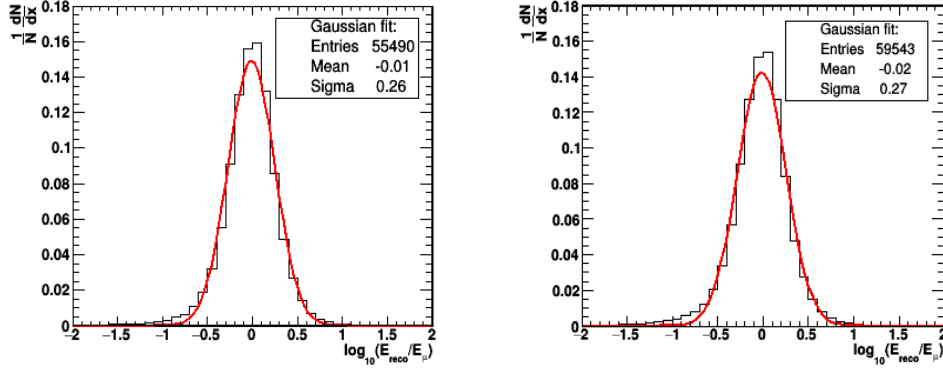


Figure 5.34: The distribution of $\log_{10}(E_{reco}/E_{\mu})$ for muons with $E_{\mu} \geq 10$ TeV for events that satisfy the containment selection (left plot) and for all reconstructed events (right plot). The y axis corresponds to $\frac{1}{N} \frac{dN}{dx}$ where $x = \log_{10}(E_{reco}/E_{\mu})$. A Gaussian fit is applied.

The results on muon energy for tracks that have been reconstructed with *recoLNS* are shown in Figures 5.35 and 5.36. The energy resolution is 0.26 for all reconstructed tracks with $E_{\mu} \geq 10$ TeV and 0.25 for tracks that also satisfy the containment selection leading to a slight improvement compared to the energy resolution for the standard detector layout. An overestimation of the muon energy, which is noticeable in the 68% and 90% quantiles in Figure 5.35, for muons in the PeV energy range, is due to the high contribution of hits from ^{40}K decays that survive the hit selection.

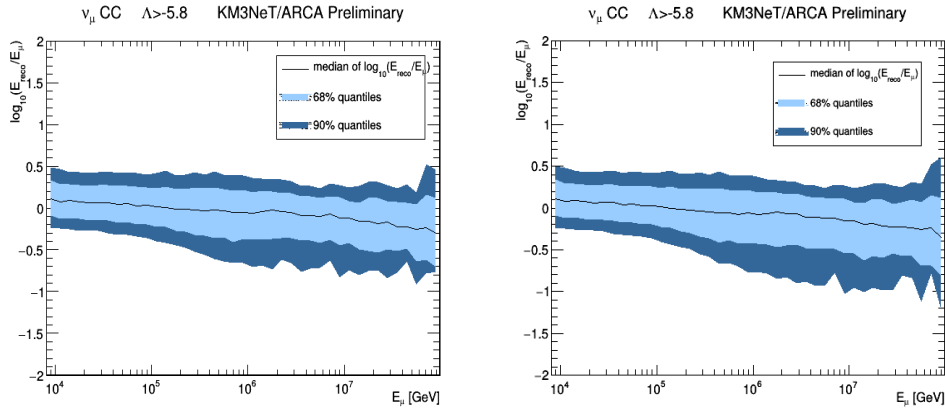


Figure 5.35: The median of $\log_{10}(E_{reco}/E_{\mu})$ (with 68% and 90% quantiles) with respect to MC muon energy ($\log_{10}E_{\mu}$) for events that satisfy the containment selection (left plot) and for all reconstructed events (right plot).

5.9 Estimating the Energy for an Alternative Detector Configuration

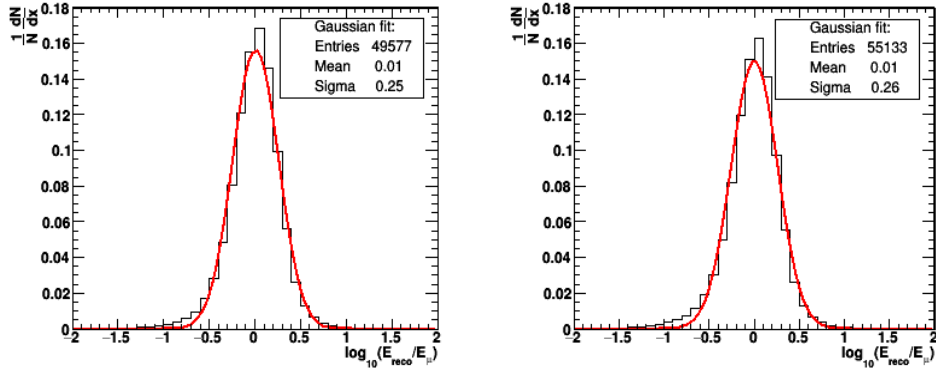


Figure 5.36: The distribution of $\log_{10}(E_{reco}/E_{\mu})$ for muons with $E_{\mu} \geq 10$ TeV for events that satisfy the containment selection (left plot) and for all reconstructed events (right plot). The y axis corresponds to $\frac{1}{N} \frac{dN}{dx}$ where $x = \log_{10}(E_{reco}/E_{\mu})$. A Gaussian fit is applied.

5. ENERGY RECONSTRUCTION WITH NEURAL NETWORKS (ERENN)

6

Sensitivity and Discovery Potential

The aim of the KM3NeT project is to search for high energy neutrinos of astrophysical origin. The potential for a discovery of extraterrestrial neutrinos and the detector sensitivity to a neutrino signal are investigated via Monte Carlo simulations and the corresponding calculations for the KM3NeT-ARCA detector are presented in this chapter.

The "binned" and the "unbinned" approach are the main statistical methods used to search for a neutrino signal among background events and calculate the sensitivity and the discovery potential of a detector. These approaches use the probability density functions (pdf) of the signal and background events in different ways. The "binned" approach separates the energy distribution¹ of the signal and background events in several bins and searches for an excess of signal over background events in each bin. In this way, all the events are either classified as events that pass the selection and are counted or as events that fail to pass the selection and are neglected. This results in a possible loss of signal events and consequently the loss of information that is contained in the event distribution and could indicate a relative agreement of the event with the signal or background hypothesis. Moreover, the selection that optimizes the sensitivity can generally be different than the selection that optimizes the discovery potential thus leading to a necessary sacrifice of one for the other. In order to overcome these problems the "unbinned" approach for the calculation of the sensitivity and discovery

¹The energy distribution is used for this study. In general, the distribution of any quality can be used to differentiate between signal and background events.

6. SENSITIVITY AND DISCOVERY POTENTIAL

potential can be used. This approach takes full advantage of the shape of the pdf for signal and background while it determines the relative contribution of the signal and background hypothesis to each event. Although this approach is more precise, it requires a significantly higher computing time. The "binned" method is used for this study in order to provide a first estimation of the impact of the energy resolution to the sensitivity and discovery potential of the KM3NeT-ARCA detector.

6.1 Sensitivity

The sensitivity of the detector to a neutrino signal refers to the theoretical neutrino flux that can be excluded at a certain confidence level (e.g. 90%) if no neutrino signal is detected. A method for the unbiased sensitivity optimization for an analysis has been proposed by Feldman and Cousins [114]. This method that was historically developed for experiments searching for neutrino oscillations, avoids non-physical confidence intervals in contrast to classical construction for upper limits. An implementation of this method for neutrino detectors is described in detail in [115].

The sensitivity of an experiment is determined by Monte-Carlo simulations and is independent from the experimental data of a neutrino telescope. For a given theoretical signal flux Φ_s which results to a mean number of signal events $\langle n_s \rangle$, the sensitivity flux at 90% confidence level Φ_{90} is calculated by:

$$\Phi_{90} = \Phi_s \times \frac{\bar{\mu}_{90}(\langle n_b \rangle)}{\langle n_s \rangle} \quad (6.1)$$

where $\bar{\mu}_{90}(\langle n_b \rangle)$ is the average upper limit expected from an ensemble of experiments with no real signal. $\bar{\mu}_{90}(\langle n_b \rangle)$ is used instead of the event upper limit $\mu_{90}(\langle n_b \rangle)$ in order to avoid the dependence on the experimentally observed number of events n_{obs} . In this way the sensitivity calculation avoids bias due to the number of observed events. The average upper limit is calculated as the sum of the expected upper limits weighted by the Poisson probability of occurrence $P(n_{obs}, \langle n_b \rangle)$. This is the probability to observe n_{obs} events given an expected number of background events $\langle n_b \rangle$. $\bar{\mu}_{90}(\langle n_b \rangle)$ is then derived by the formula:

$$\bar{\mu}_{90}(\langle n_b \rangle) = \sum_{n_{obs}=0}^{\infty} \mu_{90}(n_{obs}, \langle n_b \rangle) P(n_{obs}, \langle n_b \rangle)$$

and is related to $\langle n_b \rangle$ through a parabolic relation as shown in Figure 6.1.

In this study, the sensitivity flux, Φ_{90} , is computed at 90% confidence level (CL) but it is possible to calculate it at other levels of confidence by computing the average maximum limits at these confidence levels. The ratio $\bar{\mu}_{90}(\langle n_b \rangle)/\langle n_s \rangle$ is called the Model Rejection Factor (MRF) and the optimal selection of cuts corresponds to the one that minimises the MRF and so sets the strongest constraint on the theoretically expected signal flux.

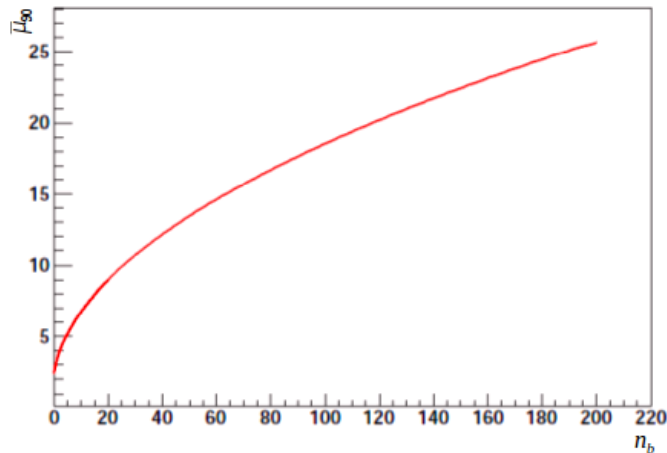


Figure 6.1: The average upper limit $\bar{\mu}_{90}$ as a function of the mean number of background events.

6.2 Discovery Potential

The discovery potential refers to the minimum number of events needed to be observed with a very small p-value ¹ resulting in a very small probability that these events originate purely from background fluctuations. Given that the background follows a Gaussian distribution, we consider a discovery if the minimum number of observed events, n_{obs} , corresponds to a p-value:

$$P(\geq n_{obs} | \langle n_b \rangle) < a, \text{ where } a = \int_{5\sigma}^{\infty} \frac{1}{\sqrt{2\pi}} e^{-\frac{x^2}{2}} dx = 5.73 \cdot 10^{-7}$$

¹The level of marginal significance within a statistical hypothesis test, representing the probability of the occurrence of a given event. The p-value is used to provide the smallest level of significance at which the background only hypothesis would be rejected. The smaller the p-value, the stronger the evidence is in favor of the signal hypothesis.

6. SENSITIVITY AND DISCOVERY POTENTIAL

is the area in the two-sided Gaussian tails beyond 5σ and $\langle n_b \rangle$ is the expected number of background events. When a signal flux Φ_s is also taken into account, the probability to observe n_{obs} events and claim a discovery considering both the signal and background distributions is: $P(\geq n_{obs} | \langle n_s \rangle + \langle n_b \rangle) < a$, where $\langle n_s \rangle$ is the mean number of signal events [116]. This probability represents the statistical power $1 - \beta$ of the discovery potential calculation, while β is the false negative rate that refers to the failure to discover something that is present. As the statistical power increases the chances of a false negative rate are decreasing. Then, the minimum number of detected events $n_{x\sigma}^{X\%CL}$ that leads to p-value less than a ($x\sigma$) in a fraction of $1 - \beta$ of the experiments, leading to $1 - \beta$ confidence level, can be determined. The $n_{x\sigma}^{X\%CL}$ depends only on the expected number of background events $\langle n_b \rangle$ as it is shown in Figure 6.2. The minimum number of detected events with a significance of 5σ at a confidence level of 50% ($n_{5\sigma}^{50\%CL}$) will be calculated in this study.

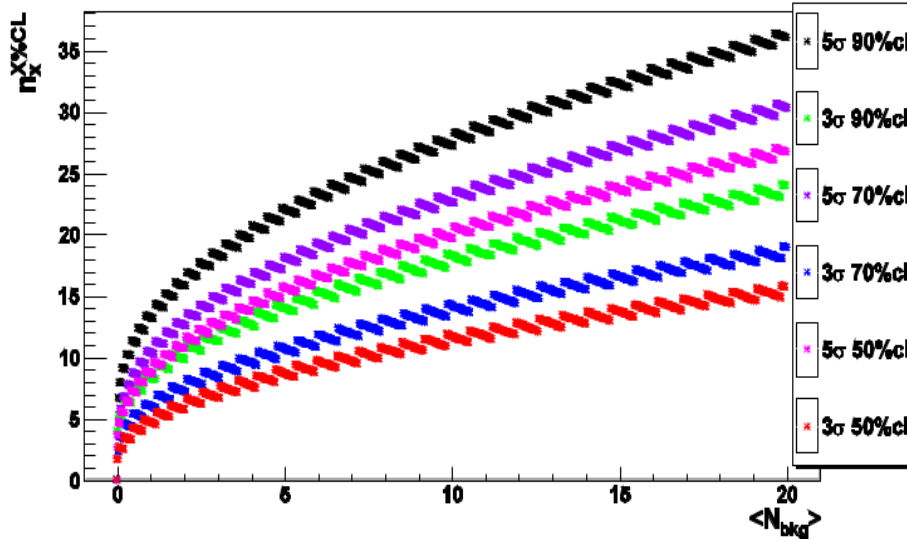


Figure 6.2: The number of events requested for a discovery with significance of 3σ and 5σ in several confidence levels (CL) with respect to the mean number of background events.

Given a theoretical signal flux Φ_s which results to a mean number of signal events $\langle n_s \rangle$, the discovery potential flux with a significance of 5σ at a confidence level of 50% is calculated by:

$$\Phi_{5\sigma} = \Phi_s \times \frac{n_{5\sigma}^{50\%CL}(\langle n_b \rangle)}{\langle n_s \rangle} \quad (6.2)$$

where the ratio $n_{5\sigma}^{50\%CL}(\langle n_b \rangle) / \langle n_s \rangle$ is called the Model Discovery Potential (MDP). As for the MRF, the selection of cuts that minimise the MDP, minimises the theoretical signal flux Φ_s that is required to obtain an observation without any original assumption of the signal scale.

6.3 Calculations of the Sensitivity and the Discovery Potential for the KM3NeT detector

In this section the sensitivity and discovery potential for 1 year of operation of the KM3NeT-ARCA detector are calculated. The astrophysical neutrino flux $\Phi(E_\nu)$ observed by IceCube was taken into account and was modeled as an isotropic, muon neutrino (and anti-neutrino) flux following a power law spectrum with a cutoff at few PeV. The existence of a cutoff is not fully investigated but rather implied by the absence of observed events with energies in the 2-10 PeV energy range during the analysis of the first events that were detected by IceCube [73]. Recently, a high energy muon event has been observed crossing the IceCube instrumented volume depositing energy of about 2.6 PeV which is expected from a muon with energy between 4 and 5 PeV indicating that the cutoff at the high energy regime may not be real [75]. The calculations for the sensitivity and the discovery potential of the KM3NeT-ARCA detector were repeated for a spectrum without cutoff in the PeV energy range. Only atmospheric ν_μ and $\bar{\nu}_\mu$ were assumed as the detector background since they correspond to the irreducible background that mainly affects the calculations for the sensitivity and discovery potential, while the atmospheric muons were not considered for these studies as their contribution in the final event sample can be neglected in a first approximation. The flux of atmospheric neutrinos corresponds to the so-called Honda flux [117] with a prompt component as calculated by Enberg [118]. The prompt component is assumed to be isotropic in the full solid angle while the Honda parameterization includes an anisotropy due to the magnetic field of the Earth.

The single-flavor energy spectrum for the IceCube astrophysical neutrino flux with cutoff at 3 PeV [73] has been parametrized as:

$$\Phi(E_\nu) = 1.2 \cdot 10^{-8} \cdot \frac{E_\nu^{-2}}{1 \text{ GeV}} \cdot e^{-E_\nu/3 \text{ PeV}} \quad [GeV^{-1} sr^{-1} s^{-1} cm^{-2}]$$

where E_ν is the neutrino energy in GeV. Although this study does not take into account the background events coming from atmospheric muons in the cal-

6. SENSITIVITY AND DISCOVERY POTENTIAL

ulation of the sensitivity and the discovery potential, the conditions that reject atmospheric muons have been considered in order to get a realistic estimate of these quantities. In order to reject atmospheric muons the Earth can be used as a shield that absorbs muons that come below the horizon while neutrinos can cross the Earth unaffected. The sensitivity and discovery potential have thus been calculated both for tracks with reconstructed zenith angle all over 2π and separately for upgoing and horizontal tracks with reconstructed angle, θ_{reco} , less than 100° (corresponding to reconstructed zenith angle greater than 80°) in order to suppress the contribution of atmospheric muons¹. Nevertheless, atmospheric muons that have been misreconstructed may survive this selection. The events that have been reconstructed with the *Chameleon* and the *recoLNS* reconstruction algorithms and survive the final selection of each reconstruction are considered for the calculations in this section in order to consider events for which the track direction has been reliably reconstructed. In this way, we avoid taking into account poorly reconstructed events and specifically atmospheric muons that are reconstructed as upgoing (with reconstructed zenith angle greater than 80°). The criteria that select well reconstructed tracks for the *Chameleon* reconstruction have been described in section 4.3 while the criteria applied for the *recoLNS* reconstruction refer to the estimator of the fit quality, Λ and the uncertainty of the track direction, β . As it is discussed in [83] a cut of $\Lambda > -5.8$ rejects most atmospheric muons and keeps most well reconstructed tracks. In order to reduce the uncertainty of the track direction a cut in β is applied while the final cut values obtained by minimising the MDP for the *recoLNS* reconstruction refer to $\Lambda \geq -5.7$ and $\beta < 1.2$. These cuts are applied for the event selection of tracks reconstructed with *recoLNS* in this section. For reconstructed tracks with the *Chameleon* reconstruction only events for which the energy is reliably reconstructed (as described in section 5.2) were taken into account as this additional selection rejects the majority of the atmospheric muons with bundle energy more than 50 TeV that constitute the main atmospheric muon contribution at the energy range above 60 TeV which is the energy range of interest for these studies.

Prior to the estimation of the sensitivity and the discovery potential, the values of the reconstructed muon energy that minimise the MRF and MDP and

¹Upgoing neutrinos with energy at about one PeV are not expected and so downgoing tracks are taken into account in order to study high energy neutrinos (above few PeV).

6.3 Calculations of the Sensitivity and the Discovery Potential for the KM3NeT detector

For a neutrino flux $\Phi(E_\nu) = 1.2 \cdot 10^{-8} \cdot \frac{E_\nu^{-2}}{1 \text{ GeV}} \cdot e^{-E_\nu/3 \text{ PeV}} \text{ [GeV}^{-1} \text{ sr}^{-1} \text{ s}^{-1} \text{ cm}^{-2}\text{]}$:

θ_{reco}	<i>MRF</i>	<i>MDP</i>	ν_{sig}	ν_{atm}
$[0^\circ, 180^\circ]$	0.563 at $E_\mu = 10^{5.15} \text{ GeV}$	1.653 at $E_\mu = 10^{5.15} \text{ GeV}$	16.26	20.82
$[0^\circ, 100^\circ)$	1.036 at $E_\mu = 10^{5.15} \text{ GeV}$	3.135 at $E_\mu = 10^{5.15} \text{ GeV}$	7.61	14.81

Table 6.1: The reconstructed E_μ that minimises the Model Rejection Factor (MRF) and the Model Discovery Potential (MDP) and the points of minimisation are reported for events that have been reconstructed with the *Chameleon* reconstruction. The number of signal ν_{sig} and background events ν_{atm} at these points are calculated.

For a neutrino flux $\Phi(E_\nu) = 1.2 \cdot 10^{-8} \cdot \frac{E_\nu^{-2}}{1 \text{ GeV}} \cdot e^{-E_\nu/3 \text{ PeV}} \text{ [GeV}^{-1} \text{ sr}^{-1} \text{ s}^{-1} \text{ cm}^{-2}\text{]}$:

θ_{reco}	$\Phi_{90} \text{ [GeV}^{-1} \text{ sr}^{-1} \text{ s}^{-1} \text{ cm}^{-2}\text{]}$	$\Phi_{5\sigma} \text{ [GeV}^{-1} \text{ sr}^{-1} \text{ s}^{-1} \text{ cm}^{-2}\text{]}$
$[0^\circ, 180^\circ]$	$0.68 \cdot 10^{-8}$	$1.98 \cdot 10^{-8}$
$[0^\circ, 100^\circ)$	$1.24 \cdot 10^{-8}$	$3.76 \cdot 10^{-8}$

Table 6.2: Calculations for the sensitivity and the discovery potential for 1 year of operation of the KM3NeT-ARCA detector for events that have been reconstructed with the *Chameleon* reconstruction.

the points of minimisation are calculated. The results for events that have been reconstructed with the *Chameleon* and the *recoLNS* algorithm are reported in Tables 6.1 and 6.3 respectively. As it can be observed in Table 6.3 both the MRF and the MDP are usually minimised at higher values when events that reach the detector from all the zenith angles are considered as in this case more events are taken into account. Then the sensitivity flux at 90% CL, Φ_{90} and the discovery potential flux with a significance 5σ at 50% CL, $\Phi_{5\sigma}$, are estimated according to relations (6.1) and (6.2) for both reconstruction algorithms and results are reported in Tables 6.2 and 6.4 respectively. As it is shown in Table 6.2 no constraint can be set to the expected flux during the first year of operation of the KM3NeT-ARCA detector for events reconstructed with the *Chameleon* algorithm when only upgoing and horizontal tracks are considered while a light constraint can be achieved for events that are reconstructed with *recoLNS* (Table

6. SENSITIVITY AND DISCOVERY POTENTIAL

For a neutrino flux $\Phi(E_\nu) = 1.2 \cdot 10^{-8} \cdot \frac{E_\nu^{-2}}{1 \text{ GeV}} \cdot e^{-E_\nu/3 \text{ PeV}} \text{ [GeV}^{-1} \text{ sr}^{-1} \text{ s}^{-1} \text{ cm}^{-2}\text{]}$:

θ_{reco}	<i>MRF</i>	<i>MDP</i>	ν_{sig}	ν_{atm}
$[0^\circ, 180^\circ]$	0.509 at $E_\mu = 10^{5.15} \text{ GeV}$	(1.537 at $E_\mu = 10^{5.15} \text{ GeV}$)	18.72	22.90
	(0.525 at $E_\mu = 10^{5.25} \text{ GeV}$)	1.534 at $E_\mu = 10^{5.25} \text{ GeV}$	15.51	15.86
$[0^\circ, 100^\circ)$	0.952 at $E_\mu = 10^{4.85} \text{ GeV}$	2.838 at $E_\mu = 10^{4.85} \text{ GeV}$	13.69	46.84

Table 6.3: The reconstructed E_μ that minimises the Model Rejection Factor (MRF) and the Model Discovery Potential (MDP) and the points of minimisation are reported for events that have been reconstructed with the *recoLNS* reconstruction. The number of signal ν_{sig} and background events ν_{atm} at these points are calculated.

For a neutrino flux $\Phi(E_\nu) = 1.2 \cdot 10^{-8} \cdot \frac{E_\nu^{-2}}{1 \text{ GeV}} \cdot e^{-E_\nu/3 \text{ PeV}} \text{ [GeV}^{-1} \text{ sr}^{-1} \text{ s}^{-1} \text{ cm}^{-2}\text{]}$:

θ_{reco}	$\Phi_{90} \text{ [GeV}^{-1} \text{ sr}^{-1} \text{ s}^{-1} \text{ cm}^{-2}\text{]}$	$\Phi_{5\sigma} \text{ [GeV}^{-1} \text{ sr}^{-1} \text{ s}^{-1} \text{ cm}^{-2}\text{]}$
$[0^\circ, 180^\circ]$	$0.61 \cdot 10^{-8}$	$1.84 \cdot 10^{-8}$
$[0^\circ, 100^\circ)$	$1.14 \cdot 10^{-8}$	$3.41 \cdot 10^{-8}$

Table 6.4: Calculations for the sensitivity and the discovery potential for 1 year of operation of the KM3NeT-ARCA detector for events that have been reconstructed with the *recoLNS* reconstruction.

6.4) but a discovery cannot be claimed in either case. If the event sample is not restricted in upgoing tracks a strong constraint can be set on the expected flux corresponding to a sensitivity flux of about $0.68 \cdot 10^{-8} \text{ [GeV}^{-1} \text{ sr}^{-1} \text{ s}^{-1} \text{ cm}^{-2}\text{]}$ for events reconstructed with *Chameleon* and $0.61 \cdot 10^{-8} \text{ [GeV}^{-1} \text{ sr}^{-1} \text{ s}^{-1} \text{ cm}^{-2}\text{]}$ for events reconstructed with *recoLNS* algorithm. This however implies that a very efficient atmospheric muon rejection can be achieved.

The corresponding calculations were repeated for the astrophysical neutrino flux $\Phi(E_\nu)$ observed by IceCube without cutoff which was then parametrized as:

$$\Phi(E_\nu) = 1.2 \cdot 10^{-8} \cdot \frac{E_\nu^{-2}}{1 \text{ GeV}} \text{ [GeV}^{-1} \text{ sr}^{-1} \text{ s}^{-1} \text{ cm}^{-2}\text{]}$$

As it can be observed in Tables 6.5 and 6.7 the MRF and MDP are minimised

6.3 Calculations of the Sensitivity and the Discovery Potential for the KM3NeT detector

in higher values of the reconstructed energy, as expected due to the contribution of muons with energy at the PeV energy range. A very strong constraint can be set in the expected neutrino flux even in the case that only upgoing and horizontal tracks are considered while a discovery can be claimed during the first year of operation of the KM3NeT-ARCA detector if tracks that reach the detector from below and above the horizon are taken into account (as it is shown in Tables 6.6, 6.8).

For a neutrino flux $\Phi(E_\nu) = 1.2 \cdot 10^{-8} \cdot \frac{E_\nu^{-2}}{1 \text{ GeV}} [GeV^{-1} sr^{-1} s^{-1} cm^{-2}]$:

θ_{reco}	MRF	MDP	ν_{sig}	ν_{atm}
$[0^\circ, 180^\circ]$	0.282 at $E_\mu = 10^{5.55} GeV$	0.792 at $E_\mu = 10^{5.55} GeV$	15.83	3.14
$[0^\circ, 100^\circ]$	0.623 at $E_\mu = 10^{5.55} GeV$	1.718 at $E_\mu = 10^{5.55} GeV$	6.24	1.95

Table 6.5: The reconstructed E_μ that minimises the Model Rejection Factor (MRF) and the Model Discovery Potential (MDP) and the points of minimisation are reported for events that have been reconstructed with the *Chameleon* reconstruction. The number of signal ν_{sig} and background events ν_{atm} at these points are calculated.

For a neutrino flux $\Phi(E_\nu) = 1.2 \cdot 10^{-8} \cdot \frac{E_\nu^{-2}}{1 \text{ GeV}} [GeV^{-1} sr^{-1} s^{-1} cm^{-2}]$:

θ_{reco}	$\Phi_{90} [GeV^{-1} sr^{-1} s^{-1} cm^{-2}]$	$\Phi_{5\sigma} [GeV^{-1} sr^{-1} s^{-1} cm^{-2}]$
$[0^\circ, 180^\circ]$	$0.34 \cdot 10^{-8}$	$0.95 \cdot 10^{-8}$
$[0^\circ, 100^\circ]$	$0.75 \cdot 10^{-8}$	$2.06 \cdot 10^{-8}$

Table 6.6: Calculations for the sensitivity and the discovery potential for 1 year of operation of the KM3NeT-ARCA detector for events that have been reconstructed with the *Chameleon* reconstruction.

6. SENSITIVITY AND DISCOVERY POTENTIAL

For a neutrino flux $\Phi(E_\nu) = 1.2 \cdot 10^{-8} \cdot \frac{E_\nu^{-2}}{1 \text{ GeV}}$ [$\text{GeV}^{-1} \text{sr}^{-1} \text{s}^{-1} \text{cm}^{-2}$]:

θ_{reco}	MRF	MDP	ν_{sig}	ν_{atm}
$[0^\circ, 180^\circ]$	0.284 at $E_\mu = 10^{5.55} \text{ GeV}$	0.824 at $E_\mu = 10^{5.55} \text{ GeV}$	17.38	4.36
$[0^\circ, 100^\circ]$	0.589 at $E_\mu = 10^{5.35} \text{ GeV}$	1.729 at $E_\mu = 10^{5.35} \text{ GeV}$	8.92	5.25

Table 6.7: The reconstructed E_μ that minimises the Model Rejection Factor (MRF) and the Model Discovery Potential (MDP) and the points of minimisation are reported for events that have been reconstructed with the *recoLNS* reconstruction. The number of signal ν_{sig} and background events ν_{atm} at these points are calculated.

For a neutrino flux $\Phi(E_\nu) = 1.2 \cdot 10^{-8} \cdot \frac{E_\nu^{-2}}{1 \text{ GeV}}$ [$\text{GeV}^{-1} \text{sr}^{-1} \text{s}^{-1} \text{cm}^{-2}$]:

θ_{reco}	Φ_{90} [$\text{GeV}^{-1} \text{sr}^{-1} \text{s}^{-1} \text{cm}^{-2}$]	$\Phi_{5\sigma}$ [$\text{GeV}^{-1} \text{sr}^{-1} \text{s}^{-1} \text{cm}^{-2}$]
$[0^\circ, 180^\circ]$	$0.34 \cdot 10^{-8}$	$0.99 \cdot 10^{-8}$
$[0^\circ, 100^\circ]$	$0.71 \cdot 10^{-8}$	$2.07 \cdot 10^{-8}$

Table 6.8: Calculations for the sensitivity and the discovery potential for 1 year of operation of the KM3NeT-ARCA detector for events that have been reconstructed with the *recoLNS* reconstruction.

6.4 Improvements on the Energy Reconstruction

It is interesting to check the effect of the imprecise knowledge of the muon (neutrino) energy on the calculations of the sensitivity and the discovery potential. For this, the simulated energy can be used to compare the MRF and the MDP for the case of "perfect" energy reconstruction.

The muon energy is underestimated for muons with energy at the PeV range leading to a shift of events to lower energy bins of the reconstructed energy resulting to a deficit of events in the high energy regime which is the energy range in which there is a lack of atmospheric neutrinos and a domination of the signal events. The MRF and the MDP are thus minimised in higher bins of the reconstructed energy while the values at these points of minimisation are larger with respect to the corresponding quantities if the MRF and the MDP

6.4 Improvements on the Energy Reconstruction

For a neutrino flux $\Phi(E_\nu) = 1.2 \cdot 10^{-8} \cdot \frac{E_\nu^{-2}}{1 \text{ GeV}} [\text{GeV}^{-1} \text{sr}^{-1} \text{s}^{-1} \text{cm}^{-2}]$:

θ_{reco}	<i>MRF</i>	<i>MDP</i>
[0°, 180°]	0.284 at $E_\mu^{reco} = 10^{5.55} \text{ GeV}$	0.824 at $E_\mu^{reco} = 10^{5.55} \text{ GeV}$
[0°, 180°]	0.216 at $E_\mu^{MC} = 10^{5.35} \text{ GeV}$	0.612 at $E_\mu^{MC} = 10^{5.45} \text{ GeV}$

Table 6.9: The reconstructed E_μ that minimise the Model Rejection Factor (MRF) and the Model Discovery Potential (MDP) and the points of minimisation are reported for events that have been reconstructed with the *recoLNS* reconstruction. The corresponding quantiles for the MC muon energy for the expected astrophysical IceCube neutrino flux without cutoff are calculated.

are calculated for the MC muon energy as it can be observed in Table 6.9¹. As the muon energy underestimation affects the points and the values of the MRF and the MDP minimisation and consequently the calculations on the sensitivity and the discovery potential for the neutrino telescope, an effort to reduce the underestimation of muon energy is made.

Despite the good energy reconstruction achieved, as described in sections 5.6 and 5.8.1, the muon energy is often underestimated for events that travel only short distances in the detector or escape the detector and thus deposit only a fraction of the light in the instrumented volume. Therefore, the introduction to the NN of additional quantities to account for the distance that the muon has traveled inside the instrumented volume is considered. Apart from the variables (described in section 5.4) that show a strong dependence on the muon energy and are used for the energy reconstruction, the length of the muon track and the maximum length possible (calculated as described in section 4.3) in the detector volume were used. In contrast to the NN input variables, these quantities do not show a strong dependence on the muon energy and thus are not used for the standard energy estimation. However, they are inserted to the NN to further enhance the distinction between events that have deposited comparable amount of light in the detector but have entered the detector in different points and have traveled different distances in the instrumented volume. The ratio of these quantities to the maximum distance, L_{max} that a muon can travel inside the

¹Events have been reconstructed with the *recoLNS* reconstruction package.

6. SENSITIVITY AND DISCOVERY POTENTIAL

instrumented volume according to its zenith angle, was estimated as:

- i. *maximum length possible* / L_{max}
- ii. *muon length* / L_{max}

where L_{max} : is the maximum distance that can be traveled inside the instrumented volume by a well contained muon and depends on the reconstructed muon zenith θ_{rec} . It is calculated as:

$$L_{max} = h + (2R - h) \cdot \sin \theta_{rec}$$

given h : the detector height, R : the detector radius. This distance corresponds to the detector diameter ($L_{max} = 1008$ m) for a horizontal track ($\theta_{rec} = 90^\circ$) and to the detector height ($L_{max} = 612$ m) for a vertical track (Figure 6.3).

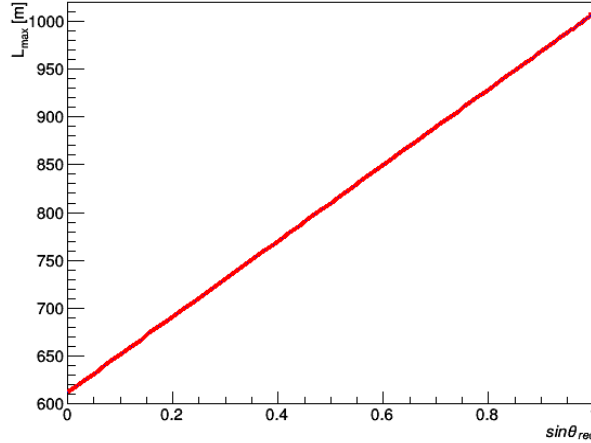


Figure 6.3: The maximum distance that can be traveled inside the instrumented volume by a well contained muon, L_{max} , as a function of the sine of the reconstructed muon zenith, $\sin \theta_{rec}$.

The variable (i) accounts for tracks that enter the detector in a point that corresponds to a short maximum length possible (or alternatively a short geometrical distance) inside the instrumented volume while the second variable (ii) differentiates tracks that stop inside the detector without traveling the maximum length possible from tracks that escape the detector. The aforementioned quantities are inserted in the Neural Network (NN) complementing the quantities (i)-(iv) that are described in section 5.4 in the muon energy reconstruction.

6.4 Improvements on the Energy Reconstruction

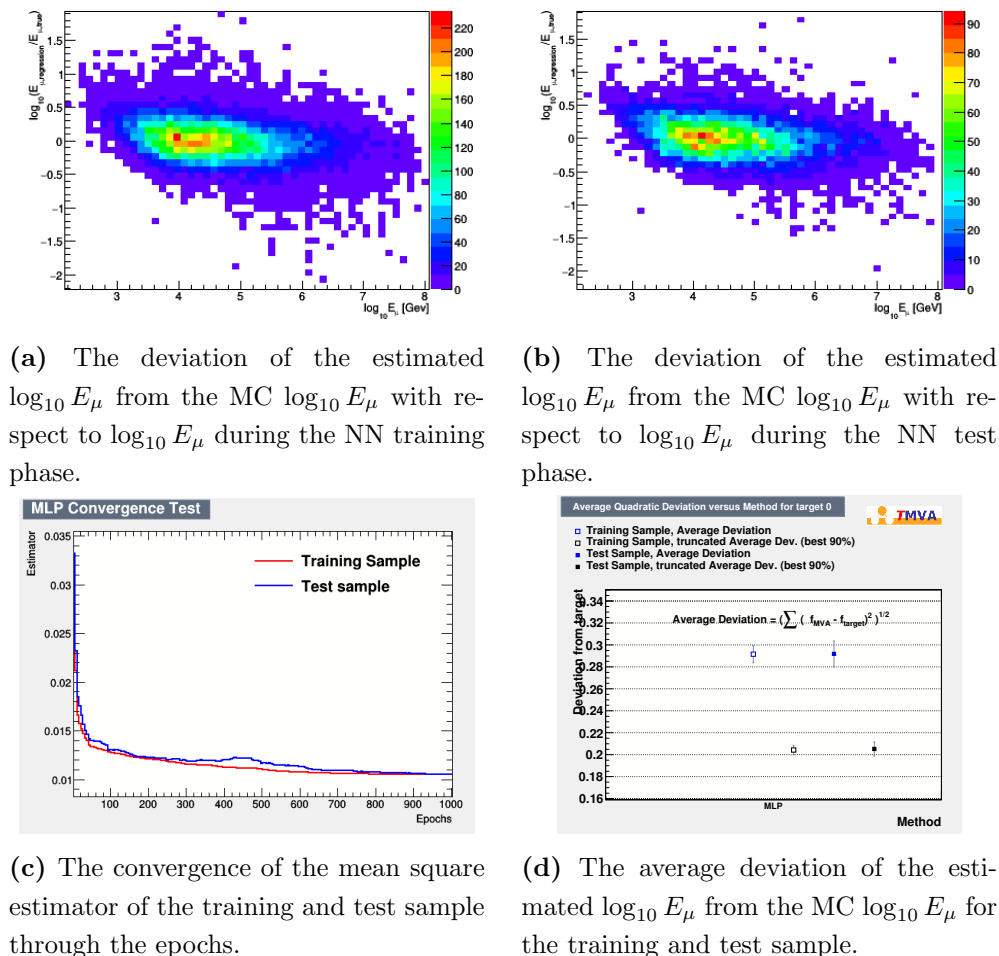


Figure 6.4: The performance of the Neural Network for the muon energy is shown.

6.4.1 Training the Neural Network

As it is described above, the first layer of this NN holds six input variables while the hidden layer consists of 13 nodes. The neuron activation function used was the hyperbolic tangent while the weights were adjusted with the use of the Broyden-Fletcher-Goldfarb-Shannon (BFGS) method [110]. Again, one half of the reconstructed event sample was used to train and test the NN and the other half for NN evaluation. The results of the training and test phase of the NN are reported in Figure 6.4. Figures 6.4 (a) and (b) show the deviation of the estimated $\log_{10} E_\mu$ from the MC $\log_{10} E_\mu$ as a function of MC $\log_{10} E_\mu$ during the NN training and test phase. The convergence of the mean square estimator for the NN training and test phase as calculated during the different epochs of

6. SENSITIVITY AND DISCOVERY POTENTIAL

training, is shown in Fig.6.4(c). The average deviation of the estimated $\log_{10} E_\mu$ from the MC $\log_{10} E_\mu$ (blue squares) and the corresponding quantity for 90% of the events for which the deviation is closer to this average (black squares) during the NN training (open squares) and test (filled squares) phase is shown in Fig.6.4(d). An average deviation of less than 0.21 for the muon energy is achieved for both training and test samples. The NN performance is stable, therefore, the energy can be evaluated for the second half of the reconstructed ν_μ event sample (as it is mentioned in section 5.5).

6.4.2 Performance of the Improved Energy Reconstruction

The input variables for the sample of ν_μ events that are used for the energy reconstruction are inserted in the Neural Network. The energy is estimated through the employment of the weights of the inter-neuron connections that were calculated during the training phase and the results are presented in Figures 6.6 and 6.8. These results refer to events that have been reconstructed with the *recoLNS* reconstruction and satisfy the $\Lambda > -5.8$ criterion. Figure 6.6 shows the reconstructed muon energy ($\log_{10} E_{reco}$) with respect to the MC muon energy ($\log_{10} E_\mu$) for well contained tracks (as described in section 5.2) and for all reconstructed tracks. The corresponding plots for the previous training of the NN (with four input variables) are shown in Figure 6.5 for comparison. As it can be observed in these figures, the new NN that takes into account the length and the maximum length possible of the track inside the detector compensates for the underestimation of the muon energy at the high energy regime leading to a linear relation of the reconstructed and the MC muon energy that extends to the entire energy range. This improvement in the muon energy reconstruction is more apparent in Figure 6.8 which shows the median of $\log_{10}(E_{reco}/E_\mu)$ with 68% and 90% quantiles with respect to $\log_{10} E_\mu$. Compared to the corresponding plot with the previous NN (as it is shown in Figure 6.7) the new energy reconstruction is an improvement as it leads to narrower quantiles and similar results for events that satisfy the containment selection and for all reconstructed tracks.

The energy resolution of this improved energy estimator for muons with energy $E_\mu \geq 10$ TeV is reported in Figure 6.9 and is equal to 0.25 both for events that satisfy the containment selection (left plot) and for all reconstructed tracks (right plot). Compared to the corresponding distributions of $\log_{10}(E_{reco}/E_\mu)$ with the previous NN which are shown in Figures 5.25, 5.26(right plots) an

6.4 Improvements on the Energy Reconstruction

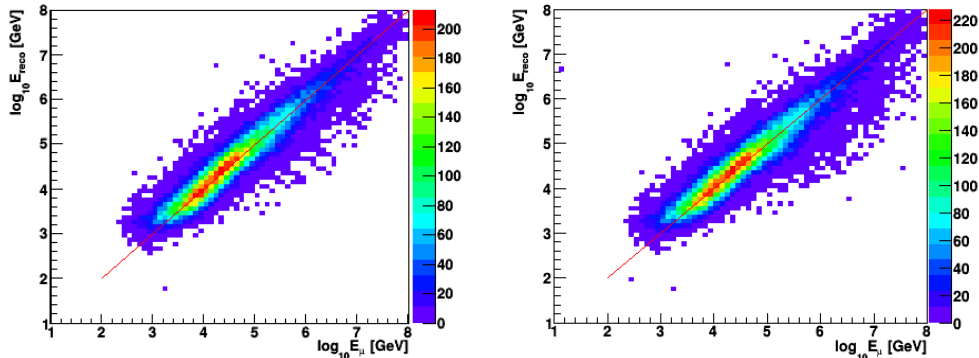


Figure 6.5: The reconstructed energy ($\log_{10} E_{reco}$) with respect to the MC muon energy ($\log_{10} E_{\mu}$) for events that satisfy the containment selection (left plot) and for all reconstructed events (right plot) before improvements. To guide the eye, the line at 45° is drawn.

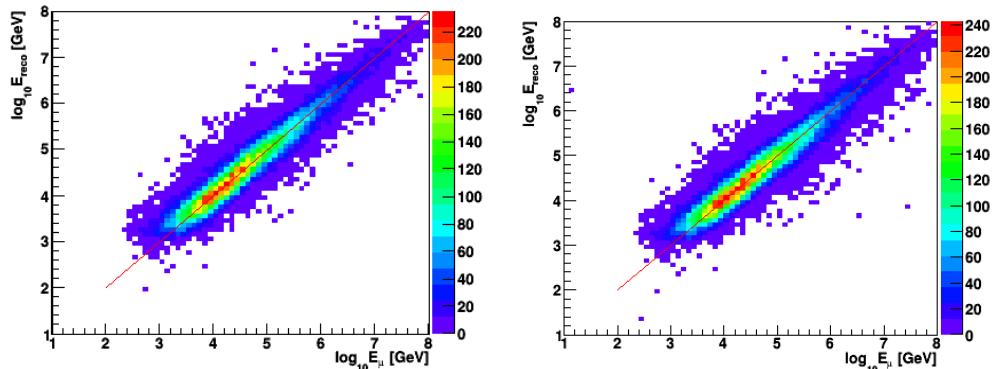


Figure 6.6: The reconstructed energy ($\log_{10} E_{reco}$) with respect to the MC muon energy ($\log_{10} E_{\mu}$) for events that satisfy the containment selection (left plot) and for all reconstructed events (right plot) after improvements. To guide the eye, the line at 45° is drawn.

improvement of about 7.5% for events that survive the containment selection and about 11% for all reconstructed events with $\Lambda > -5.8$ has been achieved. This improvement can be observed in Figure 6.10 where the black line corresponds to the previous NN training and the red line to the improved energy estimator. The distributions of $\log_{10}(E_{reco}/E_{\mu})$ are more symmetric while the number of events for which the energy has been underestimated is reduced for this new Neural Network.

6. SENSITIVITY AND DISCOVERY POTENTIAL

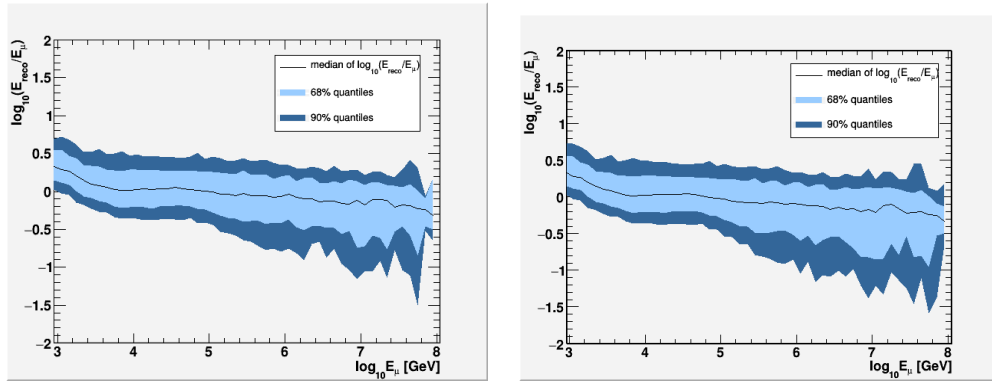


Figure 6.7: The median of the logarithm of the ratio of the reconstructed to the MC muon energy (with 68% and 90% quantiles) with respect to the MC muon energy ($\log_{10}E_{\mu}$) for events that satisfy the containment selection (left plot) and for all reconstructed events (right plot) before improvements.

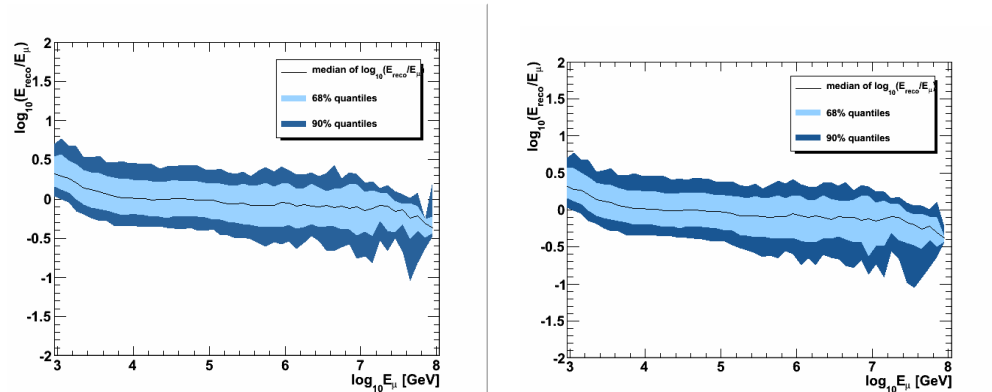


Figure 6.8: The median of the logarithm of the ratio of the reconstructed to the MC muon energy (with 68% and 90% quantiles) with respect to the MC muon energy ($\log_{10}E_{\mu}$) for events that satisfy the containment selection (left plot) and for all reconstructed events (right plot) both after the improvements.

6.5 Calculations for KM3NeT detector using the Improved Energy Reconstruction

The calculations of the sensitivity and the discovery potential for 1 year of operation of the KM3NeT-ARCA detector as it is determined by the points of minimisation of the MRF and the MDP with respect to the reconstructed muon energy with the improved energy estimator have been repeated for reconstructed events with the *recoLNS* algorithm that satisfy the Λ and β cuts (described in section 6.3). In order to study the effect of the energy resolution to the estimation of the sensitivity and the discovery potential for the whole energy range we con-

6.5 Calculations for KM3NeT detector using the Improved Energy Reconstruction

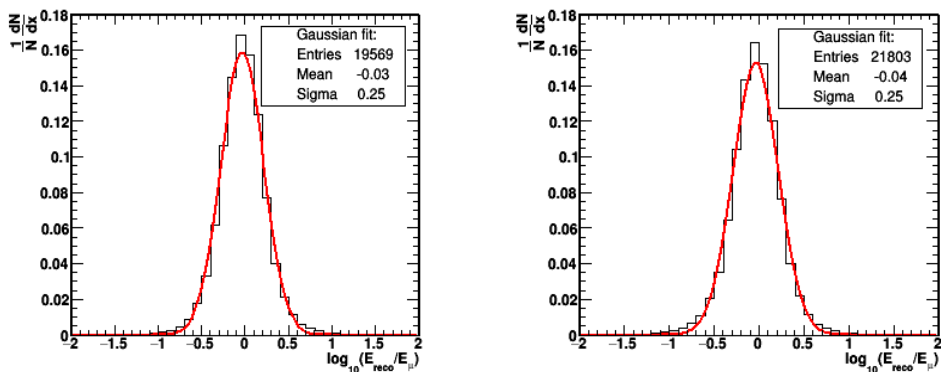


Figure 6.9: The distribution of the logarithm of the ratio of the reconstructed to the MC muon energy for muons with $E_\mu \geq 10$ TeV for events that satisfy the containment selection (left plot) and for all reconstructed events (right plot). A Gaussian fit is applied.

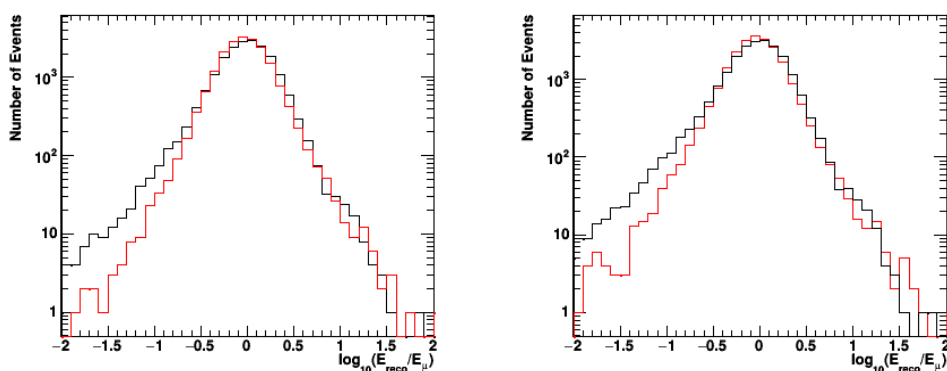


Figure 6.10: The distribution of the logarithm of the ratio of the reconstructed to the MC muon energy for muons with $E_\mu \geq 10$ TeV for events that satisfy the containment selection (left plot) and for all reconstructed events (right plot). The black line corresponds to the previous energy estimator while the red line corresponds to the new energy estimator after improvements.

sider the IceCube astrophysical neutrino flux without cutoff (as it is described in section 6.3). The points of minimization of the MRF and the MDP when the reconstructed and the MC muon energy are considered are reported in Tables 6.10 and 6.12 respectively. As it can be observed in the aforementioned tables the reconstructed energy for which the MRF and the MDP are minimised is shifted in higher energies by approximately two (or more) energy bins (or about 0.2 in $\log_{10} E_\mu$) with respect to the corresponding minimisation points when the calculations are performed for the MC muon energy. The corresponding val-

6. SENSITIVITY AND DISCOVERY POTENTIAL

For a neutrino flux $\Phi(E_\nu) = 1.2 \cdot 10^{-8} \cdot \frac{E_\nu^{-2}}{1 \text{ GeV}} [GeV^{-1} sr^{-1} s^{-1} cm^{-2}]$:

θ_{reco}	<i>MRF</i>	<i>MDP</i>	ν_{sig}	ν_{atm}
$[0^\circ, 180^\circ]$	0.276 at $E_\mu = 10^{5.45} GeV$	(0.793 at $E_\mu = 10^{5.45} GeV$)	19.26	5.40
	(0.302 at $E_\mu = 10^{5.85} GeV$)	0.755 at $E_\mu = 10^{5.85} GeV$	10.39	0.84
$[0^\circ, 100^\circ)$	0.568 at $E_\mu = 10^{5.35} GeV$	(1.725 at $E_\mu = 10^{5.35} GeV$)	9.40	5.46
	(0.577 at $E_\mu = 10^{5.55} GeV$)	1.608 at $E_\mu = 10^{5.55} GeV$	6.70	1.91

Table 6.10: The reconstructed E_μ that minimises the Model Rejection Factor (MRF) and the Model Discovery Potential (MDP) and the points of minimisation are reported for events that have been reconstructed with the *recoLNS* reconstruction. The number of signal ν_{sig} and background events ν_{atm} at these points are calculated.

For a neutrino flux $\Phi(E_\nu) = 1.2 \cdot 10^{-8} \cdot \frac{E_\nu^{-2}}{1 \text{ GeV}} [GeV^{-1} sr^{-1} s^{-1} cm^{-2}]$:

θ_{reco}	$\Phi_{90} [GeV^{-1} sr^{-1} s^{-1} cm^{-2}]$	$\Phi_{5\sigma} [GeV^{-1} sr^{-1} s^{-1} cm^{-2}]$
$[0^\circ, 180^\circ]$	$0.33 \cdot 10^{-8}$	$0.91 \cdot 10^{-8}$
$[0^\circ, 100^\circ)$	$0.68 \cdot 10^{-8}$	$1.93 \cdot 10^{-8}$

Table 6.11: Calculations for the sensitivity and the discovery potential for 1 year of operation of the KM3NeT-ARCA detector for events that have been reconstructed with the *recoLNS* reconstruction.

ues for the sensitivity and the discovery potential are reported in Tables 6.11 and 6.13. An improvement on these estimates with respect to the reconstructed muon energy with this new NN when compared to the previous training of the NN (Table 6.8) has been achieved.

For completeness, the values of the MRF and the MDP and thus the sensitivity and the discovery potential are calculated for the astrophysical IceCube neutrino flux with cutoff at about 3 PeV. Since high energy neutrinos (above few PeV) are not expected for the flux with this cutoff, only upgoing and horizontal tracks (with reconstructed zenith angle more 80°) are considered and the results

6.5 Calculations for KM3NeT detector using the Improved Energy Reconstruction

For a neutrino flux $\Phi(E_\nu) = 1.2 \cdot 10^{-8} \cdot \frac{E_\nu^{-2}}{1 \text{ GeV}} [GeV^{-1} sr^{-1} s^{-1} cm^{-2}]$:

θ_{reco}	<i>MRF</i>	<i>MDP</i>	ν_{sig}	ν_{atm}
$[0^\circ, 180^\circ]$	0.216 at $E_\mu = 10^{5.35} GeV$	(0.632 at $E_\mu = 10^{5.35} GeV$)	22.51	4.10
	(0.218 at $E_\mu = 10^{5.45} GeV$)	0.612 at $E_\mu = 10^{5.45} GeV$	19.55	2.70
$[0^\circ, 100^\circ]$	0.426 at $E_\mu = 10^{5.15} GeV$	(1.262 at $E_\mu = 10^{5.15} GeV$)	12.68	5.67
	(0.443 at $E_\mu = 10^{5.35} GeV$)	1.224 at $E_\mu = 10^{5.35} GeV$	9.25	2.35

Table 6.12: The MC E_μ that minimises the Model Rejection Factor (MRF) and the Model Discovery Potential (MDP) and the points of minimisation are reported for events that have been reconstructed with the *recoLNS* reconstruction. The number of signal ν_{sig} and background events ν_{atm} at these points are calculated.

For a neutrino flux $\Phi(E_\nu) = 1.2 \cdot 10^{-8} \cdot \frac{E_\nu^{-2}}{1 \text{ GeV}} [GeV^{-1} sr^{-1} s^{-1} cm^{-2}]$:

θ_{reco}	$\Phi_{90} [GeV^{-1} sr^{-1} s^{-1} cm^{-2}]$	$\Phi_{5\sigma} [GeV^{-1} sr^{-1} s^{-1} cm^{-2}]$
$[0^\circ, 180^\circ]$	$0.26 \cdot 10^{-8}$	$0.73 \cdot 10^{-8}$
$[0^\circ, 100^\circ]$	$0.51 \cdot 10^{-8}$	$1.47 \cdot 10^{-8}$

Table 6.13: Calculations (using the MC E_μ) for the sensitivity and the discovery potential for 1 year of operation of the KM3NeT-ARCA detector for events that have been reconstructed with the *recoLNS* reconstruction.

are summarized in Tables 6.14 and 6.15. Compared to Table 6.4 an improvement on the discovery potential can be reported while the sensitivity remains constant.

6. SENSITIVITY AND DISCOVERY POTENTIAL

For a neutrino flux $\Phi(E_\nu) = 1.2 \cdot 10^{-8} \cdot \frac{E_\nu^{-2}}{1 \text{ GeV}} \cdot e^{-E_\nu/3 \text{ PeV}} \text{ [GeV}^{-1} \text{ sr}^{-1} \text{ s}^{-1} \text{ cm}^{-2}\text{]}$:

θ_{reco}	MRF	MDP	ν_{sig}	ν_{atm}
$[0^\circ, 100^\circ)$	0.946 at $E_\mu = 10^{4.95} \text{ GeV}$	2.771 at $E_\mu = 10^{4.95} \text{ GeV}$	12.11	35.13

Table 6.14: The reconstructed E_μ that minimises the Model Rejection Factor (MRF) and the Model Discovery Potential (MDP) and the points of minimisation are reported for events that have been reconstructed with the *recoLNS* reconstruction. The number of signal ν_{sig} and background events ν_{atm} at these points are calculated.

For a neutrino flux $\Phi(E_\nu) = 1.2 \cdot 10^{-8} \cdot \frac{E_\nu^{-2}}{1 \text{ GeV}} \cdot e^{-E_\nu/3 \text{ PeV}} \text{ [GeV}^{-1} \text{ sr}^{-1} \text{ s}^{-1} \text{ cm}^{-2}\text{]}$:

θ_{reco}	$\Phi_{90} \text{ [GeV}^{-1} \text{ sr}^{-1} \text{ s}^{-1} \text{ cm}^{-2}\text{]}$	$\Phi_{5\sigma} \text{ [GeV}^{-1} \text{ sr}^{-1} \text{ s}^{-1} \text{ cm}^{-2}\text{]}$
$[0^\circ, 100^\circ)$	$1.14 \cdot 10^{-8}$	$3.33 \cdot 10^{-8}$

Table 6.15: Calculations for the sensitivity and the discovery potential for 1 year of operation of the KM3NeT-ARCA detector for events that have been reconstructed with the *recoLNS* reconstruction.

6.6 Uncertainty introduced by the energy estimator

In order to investigate the shift of the minimisation points of the MRF and the MDP to higher energies, the number of atmospheric and astrophysical ν_μ ($\bar{\nu}_\mu$) for different energy bins of the MC (E_μ^{MC}) and the reconstructed (E_μ^{reco}) muon energy are calculated and reported in Tables 6.16 and 6.17 for all reconstructed track directions ¹ and for upgoing and horizontal tracks (tracks with reconstructed zenith angle more 80°) respectively. As it can be observed in these tables the number of signal events (ν_{sig}) per energy bin of E_μ^{MC} and E_μ^{reco} is similar while the number of atmospheric neutrinos (ν_{atm}) per bin of the E_μ^{reco} is larger compared to the corresponding bin of E_μ^{MC} . In particular, the number of atmospheric neutrinos per bin of the E_μ^{reco} is comparable to the number of atmospheric neutrinos that is displayed at about two bins lower in E_μ^{MC} . This behavior could be explained by an overestimation of the muon energy, thus shifting the events to higher energy bins but the consistency of the number of ν_{sig}

¹Events have been reconstructed with the *recoLNS* reconstruction package.

has still to be investigated.

In order to check if this difference in the calculation of the number of ν_{sig} and ν_{atm} per energy bin of the simulated and the reconstructed muon energy is reasonable, we consider a muon with simulated $\log_{10}E_{\mu}^{MC} = 5.35$ (corresponding to muon energy of about 224 TeV) and suppose an uncertainty in the muon energy of about 0.25 in $\log_{10}E_{\mu}^{MC}$ that corresponds to the energy resolution of this method. Then we count the number of signal and background events for the MC muon energy at bins ¹ [5.1,5.2), [5.3,5.4) and [5.5,5.6) corresponding to $E_{\mu}^{MC} = 10^{5.15}, 10^{5.35}$ and $10^{5.55}$ as they are shown in Table 6.17. The number of ν_{atm} that are counted in the bin with $E_{\mu}^{reco} = 10^{5.35}$ is very close to the number of ν_{atm} that is observed at about two bins lower in E_{μ}^{MC} . This can happen if a muon with $E_{\mu}^{MC} = 10^{5.15}$ is overestimated at 0.25 in $\log_{10}E_{\mu}^{MC}$ (corresponding to $E_{\mu}^{reco} = 10^{5.35}$). On the other hand, the number of ν_{sig} that are counted in the bin [5.3,5.4) of E_{μ}^{reco} is slightly larger (about 2%) than the corresponding bin at E_{μ}^{MC} .

The spectrum of ν_{atm} has a steeper fall (following $E^{-3.7}$, as it can be seen in Figure 5.1) and extends to lower energies. Events for which the energy is overestimated will be added to higher energy bins resulting to a significantly larger number of ν_{atm} in this bin while the ν_{sig} spectrum is more flat (following E^{-2}), compared to the spectrum of ν_{atm} , and the weights that will be added to the events will be comparable for events for which the energy is overestimated and underestimated. An overestimation of about 0.25 is thus expected to add 141% more background events in an energy bin and 37% more signal events. Specifically, if we consider a flatter spectrum, such as the ν_{sig} spectrum, the effect in the number of detected events due to the uncertainty in energy estimation (of 0.25 in the $\log_{10}E_{\mu}^{MC}$) will be less important for the final calculations. When considering the ν_{atm} spectrum however, in which most events are at lower energies, an overestimation of detected events in higher energy bins will be favored and a larger number of ν_{atm} will be calculated.

The same behavior of the number of ν_{sig} and ν_{atm} per energy bin can be observed in Table 6.16, that refers to tracks with reconstructed zenith angle all over 2π . In this table however, the number of ν_{atm} per energy bin of E_{μ}^{reco} is

¹An uncertainty of 0.25 in $\log_{10}E_{\mu}^{MC}$ for a muon with $\log_{10}E_{\mu}^{MC} = 5.35$ (bin [5.3,5.4)) corresponds to a shift at energies of approximately $\log_{10}E_{\mu}^{MC} = 5.35 \pm 0.25$ (at energy bins [5.1,5.2) and [5.5,5.6)).

6. SENSITIVITY AND DISCOVERY POTENTIAL

smaller than the number of atmospheric neutrinos that is displayed at about two bins lower in E_μ^{MC} when compared to the corresponding quantities at Table 6.17 (that takes into account only upgoing and horizontal reconstructed tracks). This difference is due to the contribution of muons with energies at the PeV range when downgoing tracks are also considered. Muons at these high energies are usually underestimated leading to a shift of some events to lower bins of E_μ^{reco} thus partially compensating for the overestimation of the lower part of the spectrum and the shifting of E_μ^{reco} at higher energy bins.

For a neutrino flux $\Phi(E_\nu) = 1.2 \cdot 10^{-8} \cdot \frac{E_\nu^{-2}}{1 \text{ GeV}} [\text{GeV}^{-1} \text{sr}^{-1} \text{s}^{-1} \text{cm}^{-2}]$:

$E_\mu^{MC} [\text{GeV}]$	ν_{sig}	ν_{atm}	$E_\mu^{reco} [\text{GeV}]$	ν_{sig}	ν_{atm}
$10^{5.15}$	29.60	9.42	$10^{5.15}$	30.39	22.27
$10^{5.25}$	25.94	6.29	$10^{5.25}$	26.24	14.31
$10^{5.35}$	22.51	4.10	$10^{5.35}$	22.48	8.68
$10^{5.45}$	19.55	2.70	$10^{5.45}$	19.26	5.40
$10^{5.55}$	16.80	1.75	$10^{5.55}$	16.50	3.45

Table 6.16: The number of signal ν_{sig} and background events ν_{atm} are calculated for different energy bins of the MC and the reconstructed muon energy for tracks with reconstructed zenith angle all over 2π .

To conclude, the calculations of the sensitivity and the discovery potential, based on the reconstructed energy, include an uncertainty that is introduced by the ambiguity on the determination of the energy. In order to interpret the results on the sensitivity and the discovery potential, the error on the reconstruction of the energy, and specifically the energy resolution has to be considered. Apart from the resolution of energy, the percentage of events for which the energy is over(under)estimated should be taken into account, since a bias of a method on the over(under)estimation of the energy would introduce a bias in the calculation of the aforementioned quantities. A band for the sensitivity and the discovery potential containing their lower and higher values taking into account the uncertainty of the energy can be introduced. Since the energy resolution for this

6.6 Uncertainty introduced by the energy estimator

For a neutrino flux $\Phi(E_\nu) = 1.2 \cdot 10^{-8} \cdot \frac{E_\nu^{-2}}{1 \text{ GeV}} [GeV^{-1}sr^{-1}s^{-1}cm^{-2}]$:

$E_\mu^{MC} [GeV]$	ν_{sig}	ν_{atm}	$E_\mu^{reco} [GeV]$	ν_{sig}	ν_{atm}
$10^{5.15}$	12.68	5.67	$10^{5.15}$	13.31	14.12
$10^{5.25}$	10.89	3.70	$10^{5.25}$	11.20	9.09
$10^{5.35}$	9.25	2.35	$10^{5.35}$	9.40	5.46
$10^{5.45}$	7.92	1.51	$10^{5.45}$	7.94	3.24
$10^{5.55}$	6.70	0.95	$10^{5.55}$	6.70	1.91

Table 6.17: The number of signal ν_{sig} and background events ν_{atm} are calculated for different energy bins of the MC and the reconstructed muon energy for tracks with reconstructed zenith angle more 80° .

energy estimator is of about 0.25 the calculation of the lower and higher values for the sensitivity (discovery potential) band will consider background events lying in two bins higher and lower than the minimum of the MRF (and the MDP) and signal events corresponding to the bin of the MRF (MDP) minimisation. Therefore, the sensitivity band for tracks with reconstructed zenith angle all over 2π considering the IceCube flux without cutoff (as presented in Table 6.11) will lie between $[0.25 \cdot 10^{-8} GeV^{-1}sr^{-1}s^{-1}cm^{-2}, 0.48 \cdot 10^{-8} GeV^{-1}sr^{-1}s^{-1}cm^{-2}]$. These values are calculated considering the minimum and the maximum values for background events that correspond to the background events at energy bins [5.6, 5.7) and [5.2, 5.3) respectively. These bins are two bins higher and lower than the bin of the MRF minimisation ([5.4, 5.5) (Table 6.11)). As it is observed the calculated sensitivity, with a value of $0.33 \cdot 10^{-8} GeV^{-1}sr^{-1}s^{-1}cm^{-2}$ lies in this estimated band. The sensitivity calculated for the MC muon energy with a value of $0.26 \cdot 10^{-8} GeV^{-1}sr^{-1}s^{-1}cm^{-2}$, as it is shown in Table 6.13, corresponds to the lower part of the sensitivity band. Following the same procedure, the band for discovery potential is $[0.73 \cdot 10^{-8} GeV^{-1}sr^{-1}s^{-1}cm^{-2}, 1.32 \cdot 10^{-8} GeV^{-1}sr^{-1}s^{-1}cm^{-2}]$ which contains both the value of the discovery potential using the reconstructed ($0.91 \cdot 10^{-8} GeV^{-1}sr^{-1}s^{-1}cm^{-2}$) and the MC muon energy ($0.73 \cdot 10^{-8} GeV^{-1}sr^{-1}s^{-1}cm^{-2}$), as presented in Tables 6.11 and 6.13

6. SENSITIVITY AND DISCOVERY POTENTIAL

respectively. The resulting sensitivity band and discovery potential band for 1 year of operation of the KM3NeT-ARCA detector are summarized in Table 6.18 for events reconstructed using the *recoLNS* reconstruction package.

For a neutrino flux $\Phi(E_\nu) = 1.2 \cdot 10^{-8} \cdot \frac{E_\nu^{-2}}{1 \text{ GeV}} [\text{GeV}^{-1} \text{sr}^{-1} \text{s}^{-1} \text{cm}^{-2}]$:

$\Phi_{90} [\text{GeV}^{-1} \text{sr}^{-1} \text{s}^{-1} \text{cm}^{-2}]$	$\Phi_{5\sigma} [\text{GeV}^{-1} \text{sr}^{-1} \text{s}^{-1} \text{cm}^{-2}]$
$[0.25 \cdot 10^{-8}, 0.48 \cdot 10^{-8}]$	$[0.73 \cdot 10^{-8}, 1.32 \cdot 10^{-8}]$

Table 6.18: The sensitivity band and the discovery potential band for 1 year of operation of the KM3NeT-ARCA detector for events with reconstructed zenith angle all over 2π , which have been reconstructed using the *recoLNS* reconstruction package.

7

Conclusion

A novel method for the muon and neutrino energy reconstruction has been developed and is presented in this thesis. The reconstruction of the muon direction is essential for the energy estimation. For this reason, before attempting to estimate the muon energy, significant effort has been invested in improving the muon direction reconstruction.

The *Chameleon* reconstruction, which is the muon reconstruction used throughout this thesis, has been described and its performance after several improvements has been discussed. A very good pointing accuracy of about 0.2° for muons at the PeV energy range has been achieved. Comparisons of the *Chameleon* reconstruction with another track reconstruction package, the *recoLNS* reconstruction, have shown that *Chameleon* performs very well for high energy muons of $E_\mu > 50$ TeV, which is the energy regime we are mostly interested in.

Once the muon direction has been reconstructed, a Neural Network with appropriate input variables is employed for the muon energy reconstruction. The muon energy has been reconstructed with a very good energy resolution of approximately 0.25 in $\log_{10} E_\mu$ for muons at the TeV energy range. The muon energy has been estimated both for events reconstructed with the *Chameleon* and for events reconstructed with the *recoLNS* package with comparable results. The neutrino energy has been reconstructed for events that have interacted inside the instrumented volume and both Cherenkov photons and photons from the hadronic shower have been detected. A very good linear relation between the simulated and the reconstructed neutrino energy has been achieved. This method for the muon and neutrino energy reconstruction has also been applied for an alternative detector configuration with a larger distance between strings

7. CONCLUSION

leading to an instrumented volume of 0.8 km^3 instead of 0.5 km^3 for the standard detector layout. The energy has been estimated for events reconstructed with both track reconstruction algorithms leading to a very good energy resolution of approximately 0.25 in $\log_{10} E_\mu$ for muons with $E_\mu \geq 10 \text{ TeV}$.

Finally, the sensitivity and the discovery potential for the KM3NeT neutrino telescope were calculated, taking into account the astrophysical neutrino flux measured by the IceCube Collaboration. The influence of the uncertainty in the energy estimation to the calculation of the sensitivity and the discovery potential has been determined. In addition, the energy resolution has been considered in order to interpret the results of the sensitivity and the discovery potential for KM3NeT. An uncertainty band for the sensitivity and the discovery potential (containing the lower and higher values of these quantities) taking into account the energy resolution of the method was determined.

Bibliography

- [1] Updated Cosmic Ray Spectrum, web-site <http://www.physics.utah.edu/whanlon/spectrum.html>
- [2] C. Cesarsky, *Cosmic Ray Confinement in the Galaxy*, Ann. Rev. Astron. Astrophys. 18 (1980) 30
- [3] P. Blasi, *Recent developments in cosmic ray physics*, Nucl. Phys. B (2014) 12
- [4] J. Becker, *High-energy neutrinos in the context of multimessenger astrophysics*, (2008) 127
- [5] T. K. Gaisser, *Cosmic rays and particle physics*, Cambridge, Univ. Pr. (1990) 279
- [6] T. Stanev, *High Energy Cosmic Ray*, Springer, (2004) 333
- [7] R. Treumann, C. Jaroschek, *Fundamentals of Non-relativistic Collisionless Shock Physics: V. Acceleration of Charged Particles*, (2008) 41, [arXiv:0806.4046 [astro-ph]]
- [8] R. J. Protheroe, *Origin and propagation of the highest energy cosmic rays* (1996) 27, [astro-ph/9612212]
- [9] J. G. Learned, K. Mannheim, *High-energy neutrino astrophysics*, Ann. Rev. Nucl. Part. Sci. 50 (2000) 70
- [10] K. Greisen, *End to the cosmic ray spectrum?*, Phys. Rev. Lett. 16 (1966) 3
- [11] T. Kashti, E. Waxman, *Astrophysical Neutrinos: Flavor Ratios Depend on Energy*, Phys. Rev. Lett. 95, Vol. 95 (2005) 11
- [12] S. Klein, R. Mikkelsen, J. Becker Tjus, *Muon Acceleration in Cosmic-Ray Sources*, Astrophys.J. V. 779 (2013) 5

BIBLIOGRAPHY

- [13] U. Katz, C. Spiering, *High-Energy Neutrino Astrophysics: Status and Perspectives*, Prog.Part.Nucl.Phys. 67 (2012) 53
- [14] E. Waxman, *Cosmological Origin for Cosmic Rays Above 10^{19} eV*, Astrophys. J. 452 (1995) 9
- [15] F. Stecker, M. Salamon, *High energy neutrinos from quasars*, Space Sci. Rev. 75 (1996) 14
- [16] B. Paczynski, *Gamma-Ray Bursters at Cosmological Distances*, Ap. J. Lett., V. 308 (1986) 3
- [17] J. Goodman, *Are Gamma Bursts Optically Thick?*, Ap. J., V. 308 (1986) 4
- [18] E. Waxman, J. Bahcall, *High energy neutrinos from cosmological gamma-ray burst fireballs*, Phys. Rev. Lett. 78 (1997) 3
- [19] F. Stecker, *Are Diffuse High Energy Neutrinos and -rays from Starburst Galaxies Observable?*, Astropart.Phys. 26 (2007) 3
- [20] F. Acero, *Detection of Gamma Rays From a Starburst Galaxy*, (2009), 24
- [21] M. Ahlers, L. Anchordoqui, M. Gonzalez-Garcia, F. Halzen, S. Sarkar, *GZK neutrinos after the Fermi-LAT diffuse photon flux measurement*, Elsevier, Vol. 34, Iss. 2 (2010) 9
- [22] Aharonian, F. et al., HESS Collaboration, *H.E.S.S. observations of the supernova remnant RX J0852.0-4622: Shell-type morphology and spectrum of a widely extended VHE gamma-ray source*, Astrophys.J. 661 (2007) 13
- [23] W. Bednarek, *Neutrinos from the pulsar wind nebulae*, Astron.Astrophys. 407 (2003) 6
- [24] H. Christiansen, M. Orellana, G. Romero, *High-energy neutrino emission from X-ray binaries*, Phys.Rev.D73:063012 (2006) 18
- [25] A. Levinson, E. Waxman, *Probing microquasars with TeV neutrinos*, Phys. Rev. Lett. 87 (2001) 5
- [26] C. Castagnoli, G. Navarra, *On the possibility of detecting high energy neutrinos from the galactic disc*, Nucl. Phys. B Proc. Supp., Vol. 14, Iss.2 (1990) 4

- [27] F. Reines, *Neutrino interactions*, Ann. Rev. Nucl. Part. Sci. 10 (1960), 27
- [28] V. Agrawal, T. K. Gaisser, P. Lipari, and T. Stanev, *Atmospheric neutrino flux above 1 GeV*, Phys. Rev. D 53 (1996) 9
- [29] Y. Becherini, A. Margiotta, M. Sioli and M. Spurio, *A Parameterisation of single and multiple muons in the deep water or ice*, Astropart. Phys. (2008) 25
- [30] B. Baret, V. Van Elewyck, *High-energy neutrino astronomy: detection methods and first achievements*, Rep. Prog. Phys. 74 (2011) 35
- [31] T. Gaisser, *Cosmic Rays and Particle Physics*, (1990) 296
- [32] IceCube Collaboration, *A Combined Maximum Likelihood Analysis of the High Energy Astrophysical Neutrino Flux Measured with IceCube*, Astroph. J. 809, 98 (2015) 16
- [33] IceCube Collaboration, *IceCube-Gen2: A Vision for the Future of Neutrino Astronomy in Antarctica*, (2014) 20 [arXiv:1412.5106]
- [34] M. Markov, I. Zheleznykh, *On high energy neutrino physics in cosmic rays*, Nucl. Phys. 27 (1961) 385
- [35] U.F. Katz, *Deep Inelastic Positron Proton Scattering in the High Momentum Transfer Regime of HERA*, Springer, Vol. 168 (2000) 240
- [36] S. Forte, *Parton distributions at the dawn of the LHC*, Acta Phys. Pol. B 41, (2010), 51
- [37] M. B. Gay Ducati, M. M. Machado, M. V. T. Machado, *Charm production in neutral current neutrino-nucleus scattering within the color dipole approach*, Braz. J. Phys. vol.38 no.3b So Paulo (2008) 4
- [38] R. Gandhi, C. Quigg, M. Reno, I. Sarcevic, *Neutrino interactions at Ultra-high energies*, Phys.Rev. D58 093009 (1998) 32
- [39] A. Connolly, R.S. Thorne and D. Waters, *Calculation of high energy neutrino-nucleon cross sections and uncertainties using the MSTW parton distribution functions and implications for future experiments*, Phys. Rev. D 83, Iss. 11 (2011) 17

BIBLIOGRAPHY

- [40] R. Gandhi, C. Quigg, M.H. Reno and I. Sarcevic, *Neutrino interactions at ultrahigh energies*, Phys. Rev. D 58, (1998) 32
- [41] J. Pumplin, *New Generation of Parton Distributions with Uncertainties from Global QCD Analysis*, JHEP 0207:012 (2002) 44
- [42] C. Tyler, A. Olinto, G. Sigl, *Cosmic neutrinos and new physics beyond the electroweak scale*, Phys. Rev. D 63 (2001) 12
- [43] J. Alvarez-Muiz, J. Feng, F. Halzen, T. Han, D. Hooper, *Detecting microscopic black holes with neutrino telescopes*, Phys. Rev. D 65 (2002) 20
- [44] A. Cooper-Sarkar, S. Sarkar, *Predictions for high energy neutrino cross-sections from the ZEUS global PDF fits*, JHEP 0801 (2008) 10
- [45] R. Gandhi, C. Quigg, M. Reno, I. Sarcevic, *Ultrahigh-energy neutrino interactions*, Astropart. Phys. 5 (1996) 81
- [46] I.F.M. Albuquerque, J. Lamoureux, G.F. Smoot, *Astrophysical neutrino event rates and sensitivity for neutrino telescopes*, Astrophys. J. Suppl. 141 (2002) 195
- [47] H. Alaeian, *An Introduction to β -Ray Spectroscopy*, Physics 241, Stanford University, Winter (2014) available on [<http://large.stanford.edu/courses/2014/ph241/alaeian1/>]
- [48] ANTARES Coll., E. Aslanides et al., *A deep sea telescope for high-energy neutrinos*, (1999) 146 [arXiv:astro-ph/9907432]
- [49] C. Spiering, *Neutrino detectors under water and ice*, Springer, Vol. I/21/B/2/6.2 (2011) 10
- [50] D. Cowen, *Tau Neutrinos in IceCube*, J. Phys. 60 (2007) 4
- [51] F. Halzen, S. Klein, *Invited Review Article: IceCube: An instrument for neutrino astronomy*, Rev. Scien. Instr. 81, (2010) 24
- [52] KM3NeT Collaboration, *Deep sea tests of a prototype of the KM3NeT digital optical module*, Eur.Phys.J.C (2014) 9
- [53] KM3NeT Collaboration, *The prototype detection unit of the KM3NeT detector*, Eur.Phys.J.C76 (2015) 18

- [54] A. Roberts, *The birth of high-energy neutrino astronomy: A personal history of the DUMAND project*, Rev. Mod. Phys. 64 (1992) 259
- [55] Baikal Coll., I.A. Belolaptikov et al., *The Baikal underwater neutrino telescope: Design, performance and first results*, Astropart. Phys. 7 (1997) 263
- [56] AMANDA Coll., E. Andrs et al., *The AMANDA neutrino telescope: Principle of operation and first results*, Astropart. Phys. 13 (2000) 1
- [57] NESTOR Coll., L.K. Resvanis et al., *NESTOR: A neutrino particle astrophysics underwater laboratory for the Mediterranean*, Nucl. Phys. Proc. Suppl. 35 (1994) 294
- [58] NEMO Coll., E. Migneco et al., *NEMO: Status of the project*, Nucl. Phys. Proc. Suppl. 136 (2004) 6
- [59] E. Anassontzis, I. Liubarsky, A. Psallidas, L. Resvanis, D. Lenis, P. Rapidis, *Absolute angular calibration of a submarine km³ neutrino telescope*, Nucl.Instrum.Meth. A626-627 (2011) 4
- [60] The NESTOR Collaboration, *A measurement of the cosmic-ray muon flux with a module of the NESTOR neutrino telescope*, Astrop. Phys. 23 (2005) 16
- [61] E. Anassontzis, A. Ball, A. Belias, A. Fotiou, G. Grammatikakis, H. Kontogiannis, P. Koske, S. Koutsoukos, V. Lykoussis, E. Markopoulos, A. Psallidas, L. Resvanis, I. Siotis, S. Stavrakakis, G. Stavropoulos, V. Zhukov, *Water transparency measurements in the deep Ionian Sea*, Astrop. Phys. Vol. 34, Iss. 4 (2010) 11
- [62] F. Blondeau for the ANTARES Coll., *The ANTARES demonstrator: Towards a high-energy undersea neutrino telescope*, Prog. Part. Nucl. Phys. 40 (1998) 2
- [63] IceCube Coll., J. Ahrens et al., *Sensitivity of the IceCube detector to astrophysical sources of high energy muon neutrinos*, Astropart. Phys. 20 (2004) 25
- [64] ANTARES Coll., J.A. Aguilar et al., *AMADEUS-The acoustic neutrino detection test system of the ANTARES deep-sea neutrino telescope*, Nucl. Inst. Meth. A (2011) 2

BIBLIOGRAPHY

- [65] ANTARES Coll., *Measurement of the atmospheric muon flux with a 4 GeV threshold in the ANTARES neutrino telescope*, Elsevier Vol. 33, Iss. 2 (2010) 5
- [66] ANTARES Coll., *Measurement of the atmospheric ν_μ energy spectrum from 100 GeV to 200 TeV with the ANTARES telescope*, EPJ C (2013) 20
- [67] ANTARES Coll., *Searches for Point-like and extended neutrino sources close to the Galactic Centre using the ANTARES neutrino Telescope*, ApJL. (2014) 18
- [68] ANTARES Coll., *First combined search for neutrino point-sources in the Southern Hemisphere with the ANTARES and IceCube neutrino telescopes*, ApJ. (2015) 25
- [69] IceCube Collaboration, *The Design and Performance of IceCube DeepCore*, Astrop. Phys., Vol. 35, Iss. 10 (2012) 9
- [70] M. Santander, *Anisotropy of TeV and PeV cosmic rays with IceCube and IceTop*, astro-ph.HE (2012) 4
- [71] IceCube Collaboration, *IceTop as a veto in astrophysical neutrino searches for IceCube*, proceedings ICRC (2013), 4
- [72] IceCube Coll., *IceTop as a veto in astrophysical neutrino searches for IceCube*, proceedings ICRC (2013), 4
- [73] IceCube Collaboration, *Evidence for high-energy extraterrestrial neutrinos at the IceCube detector*, Science 342 (2013) 38 [arXiv:1311.5238 [astro-ph.HE]]
- [74] IceCube Collaboration, *Observation of High-Energy Astrophysical Neutrinos in Three Years of IceCube Data*, Phys. Rev. Lett. 113 (2014) 8
- [75] IceCube Collaboration, *A measurement of the diffuse astrophysical muon neutrino flux using multiple years of IceCube data*, ICRC 2015 proceedings - to be published
- [76] IceCube Collaboration, *Measurement of the Anisotropy of Cosmic Ray Arrival Directions with IceCube*, Astrophys. J. 718 (2010) 5

- [77] IceCube Collaboration, *Determining neutrino oscillation parameters from atmospheric muon neutrino disappearance with three years of IceCube Deep-Core data*, Phys. Rev. D 91 (2015) 10
- [78] IceCube-PINGU Collaboration, *Letter of Intent: The Precision IceCube Next Generation Upgrade (PINGU)*, Instr. Det., (2014) 136 [arXiv:1401.2046 [physics.ins-det]]
- [79] KM3NeT Collaboration, *KM3NeT Strategy Document*, available on <http://www.km3net.org/home.php>
- [80] KM3NeT Collaboration, *KM3NeT Technical Design Report*, available on <http://www.km3net.org/home.php>, (2010)
- [81] G. Riccobene, A. Capone, the NEMO collaboration, *Deep seawater inherent optical properties in the Southern Ionian Sea*, Astrop. Phys. Vol. 27 Iss. 1 (2007) 9
- [82] E. Anassontzis et al., *Light transmission measurements with LAMS in the Mediterranean Sea*, Nucl. Instr. Meth. in Phys. Res. A (2011) 4
- [83] KM3NeT Collaboration, *Letter of Intent for ARCA and ORCA-Astroparticle Oscillation Research with Cosmics in the Abyss*, (2016) 126 [arXiv:1601.07459 [astro-ph.IM]]
- [84] The KM3NeT Collaboration, *Expansion cone for the 3-inch PMTs of the KM3NeT optical modules*, JINST 8 T03006 (2013) 21
- [85] P. Amram et al. (ANTARES collaboration), *The ANTARES optical module*, Nucl. Instrum. Methods A 484 (2002) 15
- [86] E.G. Anassontzis et al., *The optical module for the NESTOR neutrino telescope*, Nucl. Instrum. Methods A 479, 439 (2002) 17
- [87] S. Aiello et al., *The optical modules of the phase-2 of the NEMO project*, JINST 8 (2013) 23
- [88] J. Aguilar et al. (ANTARES Collaboration), *The data acquisition system for the ANTARES neutrino telescope*, Nucl. Instr. Meth. A570 (2007) 107

BIBLIOGRAPHY

- [89] H. Le Provost et al., *A readout system-on-chip for a cubic kilometer submarine neutrino telescope*, JINST6 (2011) 18
- [90] B. Herold, *Study of ^{40}K -induced rates for a KM3NeT design option with multi-PMT optical modules*, Nucl. Instr. Meth. Phys. (2011) 3
- [91] F. C. Bunner, *ANATRES-Software/2000-008* (2000)
- [92] David .J.L. Bailey, PhD thesis, *Monte Carlo tools and analysis methods for understanding the ANTARES experiment and predicting its sensitivity to Dark Matter*, Wolfson College, Oxford, UK., (2002) 177
- [93] A. Dziewonski, D. Anderson *Preliminary Reference Earth model*, Phys. Earth Planet. Interior (1981) 60
- [94] G. Ingelmann, A. Edin, J. Rathsman, *LEPTO 6.5 A Monte Carlo generator for deep inelastic lepton-nucleon scattering*, Comput. Phys. Commun. 101 (1997) 108
- [95] G. Barr, PhD thesis, *The Separation of Signals and Background in a Nucleon Decay Experiment*, University of Oxford, (1987) 186
- [96] P. Antonioli et al., *A Three-dimensional code for muon propagation through the rock: Music*, Astropart. Phys. 7 (1997) 11
- [97] I. A. Sokalski et al., *MUM: flexible precise Monte Carlo algorithm for muon propagation through thick layers of matter*, Phys. Rev. D 64 (2001) 24
- [98] P. Lipari, T. Stanev, *Propagation of multi-TeV muons*, Phys. Rev. D 44 (1991) 12
- [99] C. Colnard, PhD thesis, *Ultra-high energy neutrino simulations*, University of Amsterdam, (2009) 177
- [100] D. Heck, J. Knapp, J.N. Capdevielle, G. Schatz, T. Thouw, *CORSIKA: A Monte Carlo Code to Simulate Extensive Air Showers*, FZKA-6019 (1998) 95
- [101] G. Carminati et al., *Mupage: A muon generator for parametric formulas*, ANTARES internal note, ANTARES-Phys/2006-003, (2006) 13

- [102] A. Margiotta, *Common simulation tools for large volume neutrino detectors*, Nuclear Instruments and Methods in Physics Research A 725 (2013) 3
- [103] A. Trovato, PhD thesis, *Development of reconstruction algorithms for large volume neutrino telescopes and their application to the KM3NeT detector*, (2013), 184
- [104] D. Lenis, G. Stavropoulos, *Chameleon: A Reconstruction package for a KM3NeT detector*, Instr. Meth. Astro (2012) 37 [arXiv:1203.6727]
- [105] A. Trovato, E. Drakopoulou, P. Sapienza, *Muon track reconstruction and muon energy estimate in KM3NeT/ARCA detector*, proceedings of ICRC2015 (2015), to be published, 8
- [106] W. Lohmann et al., *Energy loss of muons in the energy range 1-10,000 GeV*, CERN Yellow Report 85-03 (1985)
- [107] Olaf Sporns, Giulio Tononi, Rolf K"otter, *The Human Connectome: A Structural Description of the Human Brain* PLOS (2005) 10
- [108] A. Hoecker, P. Speckmayer, J. Stelzer, J. Therhaag, E. von Toerne, H. Voss, *TMVAUsersGuide* (2013) 152 available on: <http://tmva.sourceforge.net/docu/TMVAUsersGuide.pdf>
- [109] G. Cybenko, *Approximation by Superpositions of a Sigmoidal Function*, Springer, Math. Cont. Sign. Syst. (1989) 12
- [110] C.G. Broyden, *The Convergence of a Class of Double-rank Minimization Algorithms*, J.Inst. of Math. and App. 6 (1970) 76; R. Fletcher, *A New Approach to Variable Metric Algorithms*, Computer J. 13 (1970) 317; D. Goldfarb, *A Family of Variable Metric Updates Derived by Variational Means*, Math. Comp. 24 (1970) 23; D.F. Shannon, *Conditioning of Quasi-Newton Methods for Function Minimization*, Math. Comp. 24 (1970) 647
- [111] C. Mobley, *Light and Water: Radiative Transfer in Natural Waters*, Elsevier Science Publishing Co Inc. (1994) 592
- [112] E. Drakopoulou, C. Markou, E. Tzamariudaki, K. Pikounis, *Energy reconstruction of high energy muon and neutrino events in KM3NeT*, Proceedings of VLVnT2015 (2015) 4

BIBLIOGRAPHY

- [113] K. Pikounis, PhD thesis under preparation
- [114] G. Feldman, R. Cousins, *A Unified Approach to the Classical Statistical Analysis of Small Signals*, Phys. Rev. D 57 (1998) 17
- [115] C. Hill, K. Rawlins, *Unbiased cut selection for optimal upper limits in neutrino detectors: the model rejection potential technique*, Astropart. Phys. 18 (2003) 7
- [116] G. C. Hill, J. Hodges, B. Hughey, A. Karle and M. Stamatikos, *Examining the balance between optimising an analysis for the best limit setting and best discovery potential*, Proceedings of PHYSTAT05 (2006) 4
- [117] M. Honda et al., *Calculation of atmospheric neutrino flux using the interaction model calibrated with atmospheric muon data*, Phys. Rev. D 75 (2007) 50 [arXiv:astro-ph/0611418]
- [118] R. Enberg, M.H. Reno, I. Sarcevic, *Prompt neutrino fluxes from atmospheric charm*, Phys. Rev. D 78 (2008) 13 [arXiv:0806.0418 [astro-ph]]